Understanding the role of the substrate texture on superhydrophobicity

A thesis is submitted in partial fulfilment of
the requirements for the degree of
Doctor of Philosophy

Hossein Rashidian

Department of Mechanical Engineering
University of Canterbury

September 2018

Abstract

Synthetic super-hydrophobic surfaces have varied important applications ranging from the improved design of heat-exchangers in power plants and the development of high-performance wetsuits to the formulation of pesticides which best adhere to natural surfaces. When using micro-patterns to design these functional surfaces, it is crucial to understand how the droplet wets the topographical features of the substrate. To achieve a greater understanding and control of the wetting of complex surfaces, this thesis explores the interaction between an impacting droplet and a limited number of occlusions using the multiphase lattice Boltzmann method.

Firstly, the impact of a droplet onto a surface with a single ridge was simulated. Depending on two control parameters, namely the dimensionless distance from the impact point to the ridge and the Weber number, different wetting outcomes were observed including pinning, wetting and splashing. A simple model based on energy conservation was proposed to analyse the pinning-wetting and wetting-splashing transitions. Secondly, the stability of the thin liquid lamella which is formed after impact when it interacts with a small occlusion was investigated. The critical thickness below which the lamella punctures was predicted analytically. The numerical results confirmed this analytical model and demonstrated that an increase in the diameter of the occlusion, the impact velocity, or the hydrophobicity of the surface promote the formation of a hole in the lamella.

Next, simulations were performed to study the wetting outcomes for a droplet which impacts on a surface with a pair of pillars. In addition to the classical Wenzel, Cassie-Baxter, and break-up states, another wetting regime was revealed, namely the engulfed state, as the droplet wets both sides of pillars but an air pocket appears directly under the droplet in the gap between

the two pillars. Furthermore, the influences of the geometrical parameters, Weber number, and wettability of the surface on the potential outcomes for such impacts were investigated.

Finally, the wetting of an occlusion array during oblique drop impact was modelled. To the best of the applicant's knowledge no one has attempted detailed numerical simulation of such drop impacts onto sizable textured substrates. Based on the simulations by varying the impact angle and the Weber number, four various outcomes were observed: asymmetric spreading, bilateral splashing including a prompt splash and a corona splash, one-sided coronal splashing and asymmetric break-up. The numerical results revealed that the substrate texture parameters such as the post height, the space between posts, and wettability of the substrate play an important role on the occurrence of splashing.

In loving memory of my parents

Acknowledgment

I am pleased to express my sincerest gratitude to my PhD supervisor, Dr. Mathieu Sellier, for his willingness to support my work and his patience throughout my studies which allowed me to develop my skills. His valuable guidance and insightful suggestions gave me enormous encouragement in every stage of the preparation of this thesis.

I am grateful for the UC Doctoral Scholarship which supported me during my PhD. This funding gave me the freedom to fully immerse myself into research.

More generally, I thank all staff and faculty members at the department of mechanical engineering for a friendly atmosphere.

I would like to express my special appreciation to my sisters, Shideh and Shila, for their endless love and support. They always encouraged me to pursue higher education.

Last and most, I express my love and deepest affection towards my wife, Narges, for her unfailing encouragement, love, support, and patience. I have been successful in my life because she has been so much a part of it.

Preface

This thesis is submitted for the degree of Doctor of Philosophy in Mechanical Engineering at the University of Canterbury. The research described in this thesis was conducted under the primary supervision of Dr. Mathieu Sellier. Publications that have arisen from this work are:

Modelling an impact droplet on a pair of pillars (Chapter 6 and sections 3.1-3.2)

Rashidian H. and Sellier M. (2017) *Interfacial Phenomena and Heat Transfer*, 5(1): 43-57. http://dx.doi.org/10.1615/InterfacPhenomHeatTransfer.2018020347

Dynamic wetting of an occlusion after drop impact (Chapter 5 and section 3.3)

Rashidian H., Sellier M. and Mandin P. (2019) *International Journal of Multiphase Flow*, 111: 264-271. https://doi.org/10.1016/j.ijmultiphaseflow.2018.12.002

Oblique impact of a droplet on a textured substrate (Chapter 7 and section 3.4)

Rashidian H. and Sellier M. (2019) *Springer, IUTAM Book Series, 34*: Chapter 11. https://doi.org/10.1007/978-3-030-13720-5_11

Effects of a microscale ridge on dynamic wetting during drop impact (Chapter 4)

Rashidian H., Broom M., Willmot G. R. and Sellier M. This article is submitted to *Computers and Fluids* (under review).

The results shown in this thesis have been presented at the following conferences:

Modelling the spreading of a liquid droplet on a super-hydrophobic surface using the multiphase lattice Boltzmann method

Rashidian H. and Sellier M. *20th Australasian Fluid Mechanics Conference (AFMC)*. Perth, Australia. December 2016.

Engulfed state: an extra regime for the wetting of a pair of pillars

Rashidian H. and Sellier M. *Fluid in New Zealand (FiNZ)*. Christchurch, New Zealand. February 2017.

Interaction between the edge of an impacting droplet and a microscopic ridge

Willmot G. R., Broom M., Rashidian H. and Sellier M. *3rd International Conference on Droplets*. Los Angeles, USA. July 2017.

Post droplet impact lamella puncture and healing

Rashidian H. and Sellier M. *IUTAM Symposium on Recent Advances in Moving Boundary Problems in Mechanics*. Christchurch, New Zealand. February 2018.

Modelling of an oblique drop impact on a textured substrate

Rashidian H. and Sellier M. *Australia and New Zealand Nano and Microfluidics (ANZNMF) Conference*. Auckland, New Zealand. June 2018.

Contents

List of tables

List of figures

Nomenclature

A	Surface area at the lamella-air interfaces (lu^2)
A'	Surface area between the lamella and the substrate (lu^2)
a	Constant parameter of the Carnahan-Starling equation of state ($lu^5/(mu.ts^2)$)
b	Constant parameter of the Carnahan-Starling equation of state (lu^3/mu)
Bo	Bond number (-)
C	Constant parameter (-)
$\boldsymbol{c}$	Lattice speed (lu/ts)
c_s	Sound speed (lu/ts)
Ca	Capillary number (-)
D	Diameter of droplet (lu)
D_{max}	Maximum spreading diameter (lu)
$\boldsymbol{e}$	Microscopic velocity (lu/ts)
$\boldsymbol{F}$	Inter-particle force ($mu.lu/ts^2$)
f	Distribution function (mu/lu^3)
f^{eq}	Equilibrium distribution function(mu/lu^3)
G	Strength control parameter (-)
g	Gravitational acceleration (lu/ts^2)
H	Height (lu)
h_c	Critical thickness (lu)
h_l	Thickness of the lamella (lu)
KE	kinematic energy ($mu.lu^2/ts^2$)

k	discrete velocity direction (-)
L	Distance (lu)
L_x	Domain size on the x-axis (lu)
L_y	Domain size on the y-axis (lu)
L_z	Domain size on the z-axis (lu)
M	Constant parameter (-)
N	Constant parameter (-)
P	Pressure ($mu/(lu.ts^2)$)
Q	Constant parameter (-)
R	Constant parameter of the Carnahan-Starling equation of state ($lu^2/(ts^2.tu)$)
r	Occlusion radius (-)
Re	Reynolds number (-)
S	Spacing gap (lu)
SE	Surface energy ($mu.lu^2/ts^2$)
T	Temperature (tu)
T_0	Reduced temperature (-)
T_C	Critical temperature (tu)
t	Time (ts)
$\boldsymbol{U}$	Whole fluid velocity (lu/ts)
$\boldsymbol{u}$	Macroscopic velocity (lu/ts)
$\boldsymbol{u}_0$	Initial macroscopic velocity (lu/ts)
$\boldsymbol{u}^{eq}$	Equilibrium velocity (lu/ts)
V	Impact velocity (lu/ts)
V_n	Normal impact velocity (lu/ts)

V_t	Tangential impact velocity (lu/ts)
W	Width (lu)
We	Weber number (-)
We_n	Normal Weber number (-)
We_t	Tangential Weber number (-)
$\overline{z}$	Centre of gravity on the z-axis (lu)
z_0	Distance from the origin (lu)
α	Non-dimensional geometrical parameter (-)
β	Non-dimensional geometrical parameter (-)
γ	Interfacial tension between liquid-gas (mu/ts^2)
γ_{Sg}	Interfacial tension between solid-gas (mu/ts^2)
γ_{SL}	Interfacial tension between solid-liquid (mu/ts^2)
μ	Dynamic viscosity($mu/lu.ts$)
ΔSE	Total change in the surface energy ($mu.lu^2/ts^2$)
Δt	Time step (ts)
Δx	Lattice unit (lu)
ε	Non-dimensional geometrical parameter (-)
ζ	Roughness factor (-)
η	Normalized surface affinity parameter (-)
θ	Equilibrium contact angle (°)
θ_{CB}	Apparent contact angle of the droplet in the Wenzel state (°)
θ_W	Apparent contact angle of the droplet in the Cassie-Baxter state (°)
κ	Roughness factor (-)
λ	Non-dimensional geometrical parameter (-)

ν	Kinematic viscosity (lu^2/ts)
ξ	Maximum spreading factor (-)
ρ	Macroscopic density (mu/lu^3)
ρ_0	Initial macroscopic density (mu/lu^3)
ρ_g	Density of gas (mu/lu^3)
ρ_l	Density of liquid (mu/lu^3)
ρ_w	Density of wall (mu/lu^3)
τ	Relaxation time (-)
Φ	Impact angle (°)
χ	Ratio of the mass of the droplet which remains onto the substrate to the initial mass of the droplet (-)
ψ	Interaction potential factor (-)
Ω	Collision operator (-)
ω	Weight factor (-)

Abbreviations

BCs	Boundary Conditions
BGK	Bhatnagar Gross Krook
CFD	Computational Fluid Dynamics
CA	Cellular Automata
CS	Carnahan-Starling
EOS	Equation of State
FE	Free Energy
HCZ	He-Chan-Zhang
LBE	Lattice Boltzmann Equation
LBM	Lattice Boltzmann Method
LGCA	Lattice Gas Cellular Automata
MD	Molecular Dynamics
MRT	Multi Relaxation Time
PR	Peng-Robinson
RK	Redlich- Kwong
RKS	Redlich-Kwong-Soave
vdW	van der Waals
SC	Shan-Chen
SCMP	Single Component Multiphase
SRT	Single Relaxation Time

Chapter 1

1. Introduction

This chapter starts with an introduction to superhydrophobicity and gives a review on the wetting of super-hydrophobic surfaces. Then the knowledge gaps in this field of research are highlighted to motivate four various research questions. Finally, the structure of the thesis are described.

1.1 Background and motivation

When a water droplet sits on a surface, a contact angle exists at the droplet edge where the liquid-gas interface meets the solid substrate. This contact angle can be determined via the capillary forces acting on the triple line or calculating the work done when the contact line moves by a distance [1]. For an ideal solid surface, the equilibrium contact angle (θ) is defined by Young's Equation [2]:

$$\cos\theta = \frac{\gamma_{SG} - \gamma_{SL}}{\gamma} \tag{1.1}$$

where γ_{SG} , γ_{SL} and γ denote the interfacial tension between solid-gas, solid-liquid and liquid-gas respectively. A contact angle less than 90° indicates hydrophilicity and a contact angle greater than 90° corresponds to hydrophobicity. A super-hydrophobic surface has a contact angle greater than 150° [3]. The characteristics of super-hydrophobic surfaces are two-fold:

they are low energy surfaces which means water repellent and covered by a hierarchy of micro-structures [3].

Superhydrophobicity has been an important area of research over decades and the interaction between a liquid and a textured surface has attracted much attention in the scientific communities and industries [4-6]. Super-hydrophobic behaviour is observed on plant leaves such as the lotus leaf which is the best known example of super-hydrophobic surfaces in nature [7], and other natural objects such as butterfly wings, the exoskeleton of beetles and water strider legs [8-9]. Willmott et al. [10] presented the experimental results of dynamic wetting of New Zealand leaves and reported that three native plants: A. bifurcatum, E. glauca and V. albicans are highly water repellent. These naturally occurring surfaces have inspired the fabrication of man-made super-hydrophobic surfaces [11].

Fig. 1.1. *Lotus leaf is the best known example of the super-hydrophobic surface in nature.*

The development of artificial super-hydrophobic surfaces has led to several technological advances such as self-cleaning surfaces [12], anti-icing surfaces [13], anti-fouling surfaces [14] and reduced-drag surfaces [15]. These functional surfaces have varied, important applications such as the improved design of heat exchangers in power plants [16], the development of high-performance wetsuits [17], the formulation of pesticides which best adhere to natural surfaces [18], the creation of special coating for the surfaces of ships travelling to Antarctica which

minimize the amount of accumulated ice [19], etc. A key feature of many synthetic super-hydrophobic surfaces is the topographical pattern imprinted on them in the form of arrays of micron-sized pillars.

For surfaces with microstructures, previous studies reveal that two wetting states may exist: the Wenzel state where the liquid completely fills the space between the pillars [20] and the Cassie-Baxter state where the droplet effectively sits on the top of the micro-pillars with air pocket underneath [21]. Fig. 1.2 shows that both states are quite different since the Cassie-Baxter state leads to a very low contract angle hysteresis and therefore a very slippery surface on which droplets are highly mobile while the Wenzel state leads to a stickier surface where droplets are much harder to displace.

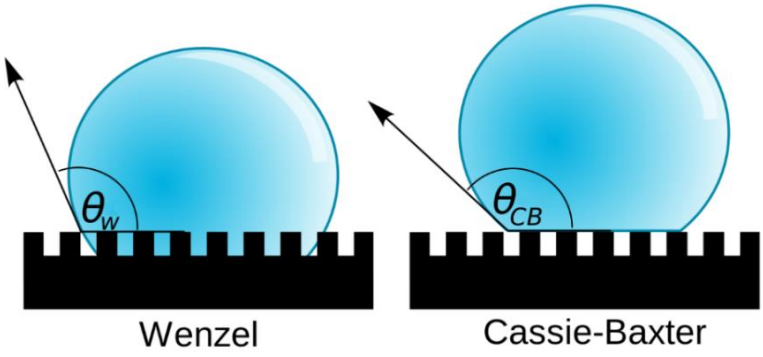

Fig. 1.2. *Two wetting states for a surface with microstructures [22].*

The stable Cassie-Baxter state, the stable Wenzel state and the transition between the two are characterized by the apparent contact angle and geometrical parameters of the pillars [23]. The apparent contact angle of a droplet in the Wenzel state is given by:

$$\cos\theta_W = \kappa \cos\theta \tag{1.2}$$

where κ denotes the roughness factor defined by the ratio of the actual surface area to the planar area. This roughness factor is given by:

$$\kappa = 1 + \frac{\pi DH}{(D+S)^2} \tag{1.3}$$

where D is the diameter of droplet and H and S denote the height of pillars and the spacing between the pillars, respectively. For the Cassie-Baxter state, the apparent contact angle is determined by:

$$\cos\theta_{CB} = -1 + \zeta(1 + \cos\theta) \tag{1.4}$$

where ζ denotes the ratio of the pillars top surface area to the substrate total base area and is given by:

$$\zeta = \frac{\pi D^2}{(D+S)^2} \tag{1.5}$$

From a thermodynamic point of view, the droplet prefers wetting surfaces with a lower free energy. Therefore, the stability of Cassie-Baxter state is described by the threshold contact angle, which is obtained by:

$$cos\,\theta^* = \frac{\zeta - 1}{\kappa - \zeta} \tag{1.6}$$

where θ^* denotes the threshold contact angle. For $\theta > \theta^*$, the Cassie-Baxter state is observed and for $\theta < \theta^*$, the Wenzel state exist.

Beside the Wenzel and the Cassie-Baxter states, an additional equilibrium state named the impaled state occurs for a small droplet on a rough hydrophobic surface as the droplet partially wets the texture but not yet touches the substrate base [24]. Recently, Bormashenko [25] has reported an exhaustive review of the main experimental and theoretical efforts on wetting transitions on rough surfaces. In addition, numerous studies have been performed numerically

to investigate flows with moving contact lines [26]. For example, Dupuis and Yeomans [27] simulated the equilibrium state and the transition between the Wenzel state and the Cassie and Baxter state using the lattice Boltzmann method. They illustrated that during transition, the spacing between pillars is filled from the centre of the droplet outwards. Lundgren et al. [28] carried out molecular dynamics simulations of wetting on rough surfaces and reported that the transition between the Wenzel state and the Cassie and Baxter state has been observed as the height of pillars increases. They also examined the influence of the pillar width and the spacing between the pillars on the contact angle and reported that the spreading increases when the pillar width and the fractional area increase. Smith et al. [29] modelled the rolling of a droplet on a tilted super-hydrophobic surface with high slip length using molecular dynamics. For such simulations, they revealed that the steady droplet motion is dominated by the contact line dissipation but for real leaves, the viscous shear prevails on the droplet motion and the slip parameter is negligible.

This research is motivated by the prospect of being able to design patterns which can control impact outcomes. The wetting outcomes are highly dependent on how the wetting front (also known as the contact line) where the liquid, solid and gas meet interacts with the substrate topographies. A better understanding of this phenomenon is likely to significantly help in the future design of artificial super-hydrophobic surfaces which will have important implications in industrial fields such as energy, agriculture and nanotechnologies.

1.2 Drop impact on a super-hydrophobic surface

Many industrial applications involve the impact of a droplet on a substrates. Examples include food coating [30], agriculture [31], inject printing [32], and spray cooling [33]. Following the impact of a liquid drop on to a solid surface, the liquid typically forms a thin lamella which

spreads over the surface [34]. Wetting outcomes are determined by parameters such as the surface roughness, impact velocity (V), drop size (D), liquid viscosity (μ) and surface tension (γ). To simplify and reduce the number of parameters, drop impact conditions can be characterized by the dimensionless Reynolds and Weber numbers, which balance inertial forces with viscous and capillary forces, respectively:

$$\mathrm{Re} = \frac{\rho V D}{\mu} \tag{1.7}$$

$$\mathrm{We} = \frac{\rho V^2 D}{\gamma} \tag{1.8}$$

In addition to these dimensionless parameters, the Capillary number which represents the balance between viscous and capillary forces is important. The Capillary number is defined as:

$$\mathrm{Ca} = \frac{\mathrm{We}}{\mathrm{Re}} = \frac{\mu V}{\gamma} \tag{1.9}$$

Furthermore, wetting outcomes of a drop impact on a patterned surface can be influenced by geometrical parameters such as the pillar spacing, pillar width and pillar height [35], pillar shapes and arrangements [36] and ambient pressure [37]. Shahraz et al. [38] noted that the wetting outcomes of a droplet deposited on a textured substrate are independent of the droplet size if the geometrical parameters are normalized by the droplet size and the effect of gravity is neglected. The gravity influence can be ignored at small Bond numbers. The Bond number which balances gravitational forces with capillary forces is determined by:

$$\mathrm{Bo} = \frac{\rho g (\frac{D}{2})^2}{\gamma} \tag{1.10}$$

where g denotes the gravitational acceleration.

The maximum spreading diameter is a significant measurable outcome of a drop impact onto a solid surface. The maximum spread occurs when an impacting droplet deforms to its largest extent on a substrate. Many relations have been proposed between impact parameters and the maximum spread diameter [39-44]. Clanet et al. [41] found that the maximum spreading of an impacting droplet with low viscosity such as water droplet on a super-hydrophobic surface depends on the droplet size and the Weber number.

For normal impacts on solid surfaces, Rioboo et al. [45] proposed that the wetting outcomes can be broken down into five categories: deposition, rebound, receding break-up, prompt splash and corona splash. The regime of interest here is splashing because this phenomena, observed in many applications, is complex and still remains less understood. As a droplet impacts on a solid surface, the kinetic energy of the droplet is transformed into surface energy (potential energy) and dissipated by the viscous shear. If kinetic energy overcomes surface energy, the lamella may either generate tiny droplets at the contact line (prompt splash) or lifts off and detaches away from the substrate and generates satellite droplets (corona splash). Various researchers have drawn links between impact parameters and splashing [37, 45-47]. This has included the identification of splash thresholds as a function of surface morphology [47] and Weber number [37]. Furthermore, splashing can be suppressed by reducing the ambient pressure [37].

Research into drop impact onto micro-patterned solid surfaces is a growing area of interest [48-49], particularly when the surfaces are super-hydrophobic. The current state of the knowledge is comprehensively reviewed by Josserand and Thoroddsen [50]. Most studies have been involved with experiments or numerical simulations of an impact droplet onto a fully pillared surface. For example, Van der Veen et al. [35] used a high speed colour interferometry technique to measure the dynamic evolution of the air layer below the droplet during impact. The effects of the pillar spacing and pillar height on the air film were investigated. They

demonstrated a dimple beneath the droplet is formed as the droplet impacts the micro-patterned surface because the air pressure below the droplet increases before the droplet wets the substrate. Bartolo et al. [51] introduced critical impact velocities for non-bouncing, bouncing and sticky regimes. They also investigated the relation between the critical impact kinetic energy with the height of the pillar for the bouncing-sticky transition and bouncing-non-bouncing transition. A model of bouncing and non-bouncing droplet impact on a super-hydrophobic surface was developed by Bange and Bhardwaj [52]. They presented a regime map to delimit the bouncing or non-bouncing state on the surface with equilibrium contact angle of 155° for different Reynolds and Weber numbers. An experimental and numerical study of pancake bouncing was carried out by Yeomans et al. [53]. Pancake bouncing takes place as impacting droplet enters the textured surface slowly thus capillary forces expel it. They reported that two important criteria exist for pancake bouncing: first a suitable time to return the fluid to the surface and second an enough kinetic energy to lift the droplet.

Notwithstanding the fact that simple models are crucial to understand how the wetting front interacts with topographic features, only a few studies are available about droplet impact on smooth surfaces with isolated topographies. For example, Josserand et al. [54] performed experiments on the impact of a droplet on a Teflon-coated surface with a small obstacle placed in the droplet spreading path. In that study, the influence of the obstacle's thickness and distance from the impact point on the splashing angle were investigated, with the Reynolds and Weber numbers held constant. Numerical simulations of such impacts were also carried out. Splashing was observed in simulations, but the splashing angle for the simulations was smaller than that in experiments. de Jong et al. [55] experimentally studied drop impact near a millimeter-sized pit and a millimeter-sized pore. They observed that depending on the distance between the impact point and the pit, three different wetting outcomes exist: splash, air bubble and jet, whereas drop impact close to the pore generated either splash or no splash and therefore neither

the air bubble nor the jet can be observed. Ellis et al. [56] compared the spreading rate computed analytically and numerically of a droplet impacting on various rough surfaces featuring a single step, a double-step, a two-sided steps and a periodic structure.

Beside the normal impact, oblique impacts of a droplet on a substrate has also been interesting topic. The wettability of the substrate and the impact parameters such as the impact angle and the Weber number may affect the wetting outcome of oblique impact. Few studies exist on the oblique impact of droplets on super-hydrophobic surfaces. For example, Yeong et al. [57] performed an investigation of the impact and rebound dynamics of droplet impacting at an angle onto a super-hydrophobic surface and reported that the maximum spread of the droplet is a function of both the normal and tangential components of the impact velocity. Aboud and Kietzig [58] carried out oblique drop impacts onto tilted moving surfaces with various wettability including super-hydrophobic surfaces to obtain the oblique splashing threshold.

1.3 Knowledge gaps

From the above literature review, we have identified knowledge gaps which this thesis is aiming to fill as detailed below.

1.3.1 Dynamic wetting of a limited number of topographical features after drop impact

In spite of the large amount of recent interest in drop impacts on super-hydrophobic surfaces, as mentioned in the literature, the problems of the wetting of a small occlusion and also a pair of occlusions have not to date been investigated in a rigorous and systematic way. Here several questions can be generated regarding the dynamic wetting of a limited number of features. For instance:

- Question 1. What are the conditions under which a spreading lamella submerges a small surface ridge?
- Question 2. How is the lamella of an impacting droplet punctured by the presence of a small occlusion?
- Question 3. A question central to the determination of the super-hydrophobic state of the surface is whether the wetting front penetrates the "pillar forest" and floods it, or rather skims on top of it. An equivalent question is whether the contact line initially "attached" to the surface is able to separate on topographic features and create an air pocket.

1.3.2 Role of the textured substrate on the wetting outcomes in oblique impacts

Regarding the oblique impact of droplets on super-hydrophobic surfaces, the effect of the geometrical parameters of the textured hydrophobic surface such as the space between posts, the height of post has not been studied. For such impacts, an important question is:

- Question 4. How do the geometrical parameters of the textured substrate influence on the behaviour of the lamella in oblique impacts? In particular, what are the conditions under which the lamella breaks-up and generates a satellite droplet?

On the other hand, in this area, the aforementioned efforts in the literature have been experimental and therefore a numerical modelling of the dynamics of the lamella resulting from the oblique impact of a droplet onto a horizontal textured substrate has not been investigated in depth yet.

1.4 Objectives

When using micro-patterns to design surfaces, it is important to understand the interaction between impacting drops and topographical features. The aim of this research is to provide simple design principle in terms of the intrinsic wettability of the geometrical properties of the micro-pillar forest and the flow conditions.

This thesis extends previous studies on the influence of substrate texture on super-hydrophobicity and helps fill the gaps in the current understanding. To answer the questions, mentioned in the previous section, numerical simulations are used because they enable a deeper understanding of the wetting process. Moreover, experimental works may difficult and also are unable to achieve sufficient temporal and spatial resolution to really understand the underlying physics. The lattice Boltzmann method which has provided a popular way to study the flow which involve capillary and wetting phenomena is our tool of choice for the investigation of the role of control parameters such as the occlusion size, Weber number and surface wettability on wetting outcomes. Therefore, multiphase lattice Boltzmann solvers are developed in two-dimensions (2D) and also three-dimensions (3D) to simulate:

- The wetting of a single occlusion in 2D
- The wetting of a single occlusion in 3D
- The wetting of a pair of occlusions in 2D
- The wetting of an occlusion array in oblique impacts in 2D

The hypothesis is that understanding the wetting of a limited number of topographical features will help understand more complex substrates and the super-hydrophobic state and its transitions.

1.5 Thesis outline

The present work is structured as follows.

Chapter 1 provides an introduction to superhydrophobicity and gives a review of the literature on the wetting of super-hydrophobic surfaces. Then the knowledge gaps in this field of research are highlighted to motivate four various research questions.

Chapter 2 describes the multiphase lattice Boltzmann method which is our methodology in this thesis. This chapter starts with the philosophy behind the lattice Boltzmann method and gives a history of this methodology. Then, a comprehensive explanation of the lattice Boltzmann method including general equations, variables and units, boundary conditions, force term and equation of state are provided. Finally, the numerical algorithm which has been implemented in FORTRAN for 2D and 3D flows is presented.

Chapter 3 provides four validation cases to demonstrate the ability of our lattice Boltzmann code to simulate wetting phenomena. All validation cases involve the study of a drop impact onto a smooth solid surface. For such impacts, several significant outcomes including the equilibrium contact angle, the maximum spreading diameter for both normal and oblique drop impacts and the thickness of the lamella at maximum spread are measured from the simulations. Finally these numerical results are compared with relevant well-known correlations previously reported in the literature.

Chapter 4 is the first result chapter. It investigates the conditions under which a spreading lamella submerges a small surface ridge. To achieve this goal, a two-dimensional multiphase lattice Boltzmann code is developed for simulating the impact and spreading of a droplet on a small ridge. First three basic outcomes are identified when the lamella comes into contact with the ridge. For each outcome, a side-by-side comparison is carried out with the experimental

results which have been obtained using high speed photography by Dr G.R. Willmott and his PhD student M. Broom. Then the effects of control parameters on the potential outcomes are investigated and a phase portrait of the different wetting outcomes is presented. Finally, an energy balance approach is used to study the transition between the different outcomes.

Chapter 5 investigates how and under which conditions the lamella of an impacting droplet is punctured by the presence of a small occlusion. An analytical model based on energy balance is proposed to obtain the critical thickness below which the liquid layer above the occlusion is unstable and lamella rupture occurs. Then, a 3D multiphase lattice Boltzmann code is developed to confirm the energy balance analysis and study the influence of key parameters like the size of the occlusion, the impact velocity and the wettability of substrate on hole formation.

Chapter 6 presents the wetting outcomes for an impacting droplet on a surface with a pair of pillars using the 2D multiphase lattice Boltzmann method. The effect of geometrical parameters on the wetting outcomes is studied. Then a regime map for different Weber numbers and geometrical parameters are proposed to predict the whole range of possible wetting states. Finally, the influence of patterned substrates wettability on outcomes is also presented.

Chapter 7 examines the conditions under which the lamella lifts off the substrate and generates a satellite droplet. This chapter is a first attempt to simulate an oblique drop impact on a textured substrate using the 2D multiphase lattice Boltzmann method. Firstly, depending on the impact angle and the Weber number, various outcomes are identified. Then a graph which shows splashing thresholds for a range of normal Weber numbers and impact angles is presented. Finally, the influence of substrate texture parameters such as the height of posts, space between posts and wettability of the substrate are investigated.

Chapter 8 presents the key conclusions of the current work and suggestions for future works.

Chapter 2

2. Methodology

The aim of this chapter is to describe the single component multiphase (SCMP) Shan-Chen (SC) model of the lattice Boltzmann method (LBM) which is employed in this thesis. The present chapter starts with the philosophy behind the LBM and gives a history of the LBM. Then a comprehensive explanation of this methodology including general equations, variables and units in LBM, boundary conditions, force term and equation of state in the SC model are provided. Finally, the numerical algorithm which has been implemented in FORTRAN is presented.

2.1 Introduction

In computational fluid dynamics (CFD), the macroscopic scale and the microscopic scale are two very distinct viewpoints from which to simulate the transport equations. Although the macroscopic continuum approach has many advantages, it may face difficulties since some problems in fluid dynamics involve microscopic interactions such as the dynamics of wetting. The microscopic molecular dynamics (MD) approach, on the other hand, is able to handle such these problems without any difficulties through the study of the behaviour of a collection of individual particles which interact with each other; however, the enormous computing demand limits the method to very small systems described by a very large number of particles. For

instance; Kadau et al. [59] simulated a cubic piece of metal with a micron edge length using a maximum of 320 billion atoms in double precision.

The lattice Boltzmann method (LBM) operates in the so-called the mesoscopic scale and can be considered as a bridge between the microscopic and the macroscopic worlds through a distribution function of particles. The distribution function represents the property and the behaviour of a collection of particles. Thus, the LBM offers advantages over both mainstream approaches which will be described later.

Historically the LBM originated from the cellular automata concept which was first described by Stanislaw Ulam and John von Neumann [60] in the 1940s. A cellular automata (CA) is a discrete model which occupies a position on a grid in space. The CA interacts with its neighbours and examines and updates its own state and also neighbours states at any specific time step according to mathematical functions. Frisch et al. [61] identified the lattice gas cellular automata (LGCA) as a suitable tool to solve the three dimensional Navier-Stokes equations in 1986.

Several issues of the LGCA such as non-isotropic advection term, pressure-velocity relation, and noise which were hard to solve or unsolved led to the development of the LBM. McNamara and Zanetti [62] introduced the lattice Boltzmann equations as a numerical scheme in 1988. They removed the statistical noise with replacing an average distribution function which was still directionally discrete instead of individual particles. Afterwards, Lallemand and Luo reported in 2000 [63] that the LBM can be obtained from the Boltzmann equation. Then, Wolf-Gladrow [64] recovered the traditional continuity and Navier-Stokes equations from the LBM through a Chapman-Enskog expansion of the Boltzmann equation. In addition to this advantage, the LBM has other benefits. For example, in the LBM the pressure and the density are related through the equation of state (EOS) and therefore the Poisson equation does not have to be solved as would be the case in traditional CFD methods. Moreover, a problem with

a complex domain can be solved using parallel process computing with a good level of accuracy. Both of these lead to reduce the computational time. Finally, the LBM can handle no slip boundary conditions easily as will be discussed in next section. These major advantages have led the LBM to become a powerful CFD tool for simulating single and multiphase flow problems.

2.2 Lattice Boltzmann method

2.2.1 Boltzmann equation

The Boltzmann equation, also called the Boltzmann transport equation, describes the transport of a particle distribution function $f(\boldsymbol{x}, \boldsymbol{e}, t)$ at time t, location $\boldsymbol{x}$ with a microscopic velocity $\boldsymbol{e}$. The Boltzmann transport equation without an external force can be written as:

$$\frac{\partial f}{\partial t} + \boldsymbol{e}.\nabla f = \Omega(f) \tag{2.1}$$

The above equation represents an advection equation with a source term $\Omega(f)$. This $\Omega(f)$, namely the collision operator, is a function of the particle distribution function. If the collision operator is known, Eq. (2.1) which is a nonlinear integro-differential equation can be solved. Higuera et al. [65] developed an efficient scheme for building the collision matrix which was linearized the collision operator. Then Qian et al. [66] replaced it with the Bhatnagar, Gross and Krook (BGK) single relaxation time model which was originally proposed by Bhatnagar et al. [67] due to its simplicity and efficiency.

Following the BGK approximation, collisions are inclined to relax the distribution function towards local equilibrium with a relaxation time τ and therefore:

$$\Omega_{BGK}(f) = \frac{f^{eq} - f}{\tau} \tag{2.2}$$

where f^{eq} denotes the local equilibrium distribution function

The local equilibrium distribution function is described by the Maxwell-Boltzmann distribution according to:

$$f^{eq} = \frac{\rho}{2\pi/3} \exp(-\frac{3}{2}(\boldsymbol{e} - \boldsymbol{u})^2) \tag{2.3}$$

where ρ and $\boldsymbol{u}$ denote the density and macroscopic velocity, respectively. These macroscopic quantities can be determined by integrating the distribution function moments over the velocity space:

$$\rho(\boldsymbol{x}, t) = \int f(\boldsymbol{x}, \boldsymbol{e}, t) d\boldsymbol{e} \tag{2.4}$$

$$\rho(\boldsymbol{x}, t)\boldsymbol{u}(\boldsymbol{x}, t) = \int \boldsymbol{e} f(\boldsymbol{x}, \boldsymbol{e}, t) d\boldsymbol{e} \tag{2.5}$$

2.2.2 Lattice Boltzmann equation

The main idea behind the LBM is to solve numerically the Boltzmann equation. Therefore, the Boltzmann equation with BGK approximation can be symbolically written considering $f \xrightarrow{discretised\ into} f_k$, $f^{eq} \xrightarrow{discretised\ into} f_k^{eq}$ and $\boldsymbol{e} \xrightarrow{discretised\ into} \boldsymbol{e}_k$ where k denotes a discrete velocity direction:

$$\frac{\partial f_k}{\partial t} + \boldsymbol{e}_k . \nabla f_k = \frac{f_k^{eq} - f_k}{\tau} \tag{2.6}$$

The above linear partial differential equation which is similar to an advection equation (left hand side) with a source term (right hand side) can be discretised as:

$$\frac{f_k(\boldsymbol{x}, t+\Delta t) - f_k(\boldsymbol{x}, t)}{\Delta t} + \boldsymbol{e}_k \frac{f_k(\boldsymbol{x}+\boldsymbol{e}_k\Delta t, t+\Delta t) - f_k(\boldsymbol{x}, t+\Delta t)}{\boldsymbol{e}_k \Delta t} = \frac{f_k^{eq}(\boldsymbol{x}, t) - f_k(\boldsymbol{x}, t)}{\tau} \tag{2.7}$$

Where $\boldsymbol{e}_k$ and Δt are the discrete microscopic velocities and the time step, respectively.

Eq. (2.7) can be rewritten as:

$$f_k(\boldsymbol{x}+\boldsymbol{e}_k\Delta t, t+\Delta t) - f_k(\boldsymbol{x}, t) = \frac{\Delta t}{\tau}[f_k^{eq}(\boldsymbol{x}, t) - f_k(\boldsymbol{x}, t)] \tag{2.8}$$

The above equation is the so-called lattice Boltzmann equation (LBE) and consists of a streaming step (left hand side) which models the particle distribution advection along the lattice link and a collision step (right hand side) which models the rate of change in the particle distribution. In fact, during the streaming process a fraction of the distribution propagates with the discrete microscopic velocities $\boldsymbol{e}_k$ from a lattice position $\boldsymbol{x}$ to its neighbouring lattice $\boldsymbol{x} + \boldsymbol{e}_k\Delta t$ via certain directions or lattice links k at the following time step Δt. On the other hand, a portion of the other particles is moving from various directions to the same lattice simultaneously and therefore the collision process will take place at this lattice. The collision step affects the numbers of original particles in each direction.

The final local equilibrium distribution function can be determined using a Taylor series expansion in Eq. (2.3):

$$f_k^{eq} = \omega_k \rho[1 + \frac{\boldsymbol{e}_k.\boldsymbol{u}}{c_s^2} + \frac{1}{2}\left(\frac{\boldsymbol{e}_k.\boldsymbol{u}}{c_s^2}\right)^2 - \frac{\boldsymbol{u}.\boldsymbol{u}}{2c_s^2}] \tag{2.9}$$

where c_s and ω_k denote the speed of sound and the weight factors, respectively. These parameters as well as the discrete velocities are dependent on discrete velocity models which will be specified later.

To calculate the equilibrium distribution function, the macroscopic quantities ρ and $\boldsymbol{u}$ can be obtained from the density distributions according to

$$\rho = \sum_k f_k \tag{2.10}$$

$$\rho \boldsymbol{u} = \sum_k f_k \, \boldsymbol{e}_k \tag{2.11}$$

The discrete LBE which is commonly implemented in the LBM is referred to as the BGK model with a single relaxation time (SRT). The kinematic viscosity is related to this relaxation time is defined as:

$$v = c_s^2(\tau - 0.5)\Delta t \tag{2.12}$$

It is also worth noting that in some problems a higher numerical stability and accuracy than the SRT scheme is needed and therefore the multi-relaxation time (MRT) scheme with other collision operators can be applied [68].

2.2.3 Lattice structures

Discrete velocity models which play an essential role in the LBM are specified as D*n*Q*m*, where *n* denotes the space dimension and *m* denotes the number of velocities. The popular two dimensions (2D) and three dimensions (3D) discrete velocity models which have been used especially in fluid dynamics problem are D2Q9 [66] and D3Q19 [64], respectively. Fig. 2.1 illustrates their lattice arrangements. As shown in this figure, the D2Q9 model involves nine

velocity vectors labelled $k = 0,\ldots,8$ in 2D and the D3Q19 model has nineteen velocity vectors such that $k = 0,\ldots,18$ in 3D.

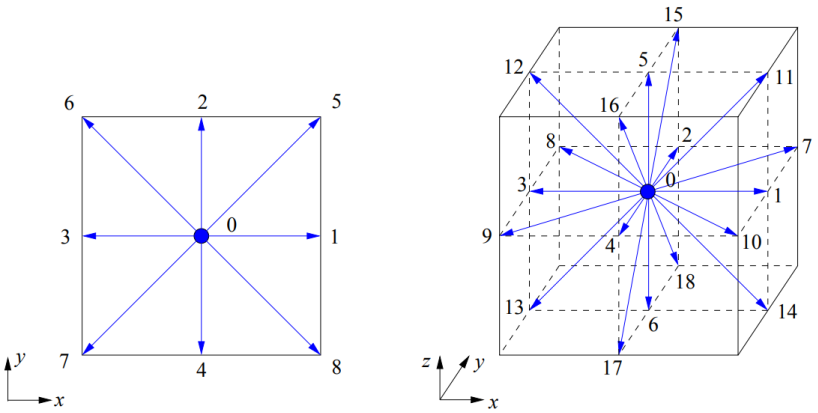

Fig. 2.1. *Lattice arrangements for the D2Q9 (left) and the D3Q19 (right)*

For these discrete velocity models, the sound speed is determined as:

$$c_s^2 = \frac{c^2}{3} \tag{2.13}$$

where c denotes the lattice speed which is given by $c = \frac{\Delta x}{\Delta t}$.

Furthermore, the discrete microscopic velocities and the weight factors are given as follows:

For the D2Q9:

$$\boldsymbol{e}_k = \begin{cases} (0,0) & k = 0 \\ c\,(\cos\left(\frac{(k-1)\pi}{4}\right), \sin\left(\frac{(k-1)\pi}{4}\right)) & k = 1,2,3,4 \\ \sqrt{2}\,c\,(\cos\left(\frac{(k-9/2)\pi}{2}\right), \sin\left(\frac{(k-9/2)\pi}{2}\right)) & k = 5,6,7,8 \end{cases} \tag{2.14}$$

$$\omega_k = \begin{cases} 4/9 & k = 0 \\ 1/9 & k = 1,2,3,4 \\ 1/36 & k = 5,6,7,8 \end{cases} \tag{2.15}$$

For the D3Q19:

$$\boldsymbol{e}_k = \begin{cases} (0,0,0) & k = 0 \\ c\ (\pm 1,0,0), c(0,\pm 1,0), c(0,0,\pm 1) & k = 1,2,\dots,6 \\ c\ (\pm 1,\pm 1,0), c(\pm 1,0,\pm 1), c(0,\pm 1,\pm 1) & k = 7,8,\dots,18 \end{cases} \tag{2.16}$$

$$\omega_k = \begin{cases} 1/3 & k = 0 \\ 1/18 & k = 1,2,\dots,6 \\ 1/36 & k = 7,8,\dots,18 \end{cases} \tag{2.17}$$

The weight factors are obtained so as to achieve isotropy of the fourth-order tensor of velocities and Galilean invariance [64, 66]. Other discrete velocity models in the LBM exist such as D2Q7 [69], D3Q15 [64] and D3Q27 [70], but they are not applied in simulations in this study.

2.2.3 Boundary Conditions

Various boundary conditions exist in the LBM including bounce-back, moving or rotating walls, inlet and outlet boundaries with known velocity and pressure distributions, periodic and symmetry [71-73]. The basic premise of using boundary conditions is to determine unknown distribution functions entering the simulation domain along the lattice links embedded in the boundaries. In this study, the periodic boundary condition for the lateral sides of the bounding box and the bounce-back boundary conditions at the solid-liquid interface and are applied because these are particularly simple and efficient.

The bounce-back boundary conditions are usually applied to replicate the no-slip state on the boundary. For the bounce-back boundary condition, distribution functions from a lattice boundary node hit the wall during the streaming process and scatter back to the same node via reversed lattice links. This process for the D2Q9 model is illustrated in Fig. 2.2. It can be seen that the distribution functions from a boundary node propagate along their lattice links. After

propagation, five distribution functions (blue arrows) move towards the corresponding neighbouring nodes following the stream process, while three distributions (black arrows) are bounced back to the same node they had originated from.

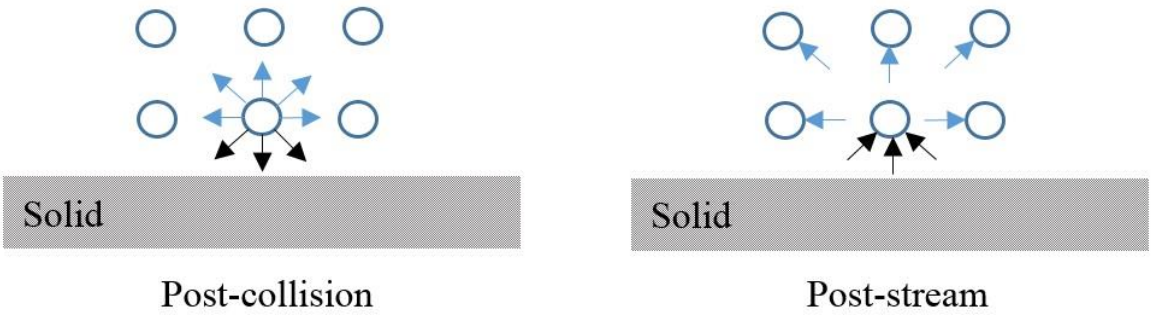

Fig. 2.2. *Bounce-back boundary conditions.*

The periodic boundary conditions are known as the simplest scheme in the LBM. To achieve a periodic boundary condition, the distribution functions carry on the opposite wall once they reach the end of the region, as demonstrated in Fig. 2.3.

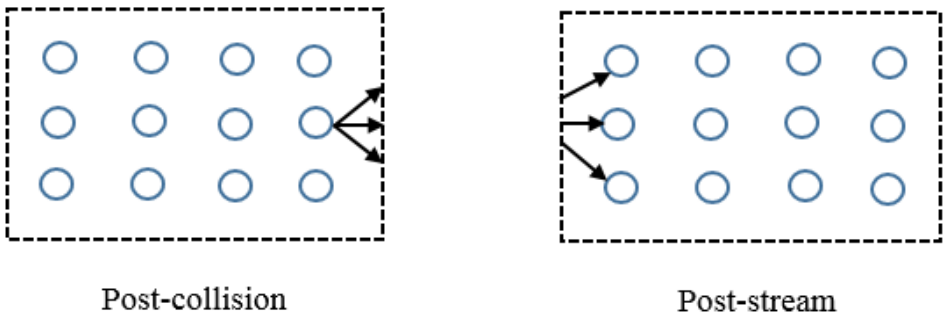

Fig. 2.3. *Periodic boundary conditions.*

2.3 Multiphase lattice Boltzmann methods

In addition to simulating single-phase flows, the LBM is able to model multiphase flows. Over the last two decades, several multiphase LBMs have been developed such as the Rothman-

Keller (RK) colour-gradient model (1988 and 1991) [74-75], the Shan-Chen (SC) model (1993 and 1994) [76-77], the Free Energy (FE) model (1995 and 1996) [78-79] and the He-Chan-Zhang (HCZ) model (1999 and 2005) [80-81].

In this study, the SC model which has the ability to model multiphase flows with single component such as water and vapour is implemented because of its simplicity and popularity. Recently, numerous applications have been investigated using the single-component multiphase (SCMP) model such as bubble rise [82], cavitation [83], moving contact line [84-85], porous media [86] and this method has had great success to simulate multiphase problems. This model is also suitable for simulating wetting phenomena such as the interaction between impacting drops and surfaces as will be demonstrated in next chapter. Furthermore, the current work intends to clearly state limitations of the SCMP model.

2.4 Single-component multiphase Shan-Chen Model

To consider the interaction between fluid-fluid and solid-fluid, the SCMP Shan-Chen (SC) model [76] is implemented. In the SCMP model, incorporating the inter-particle forcing term into the correlated lattice Boltzmann equation changes the equation of state (EOS) from an ideal gas to a non-ideal and non-monotonic one. The inter-particle force is given by:

$$\boldsymbol{F}(\boldsymbol{x},t) = -G\psi(\boldsymbol{x},t)\sum_{k}\omega_k\psi(\boldsymbol{x}+\boldsymbol{e}_k\Delta t,t)\boldsymbol{e}_k \tag{2.18}$$

where G denotes the strength controlling parameter and creates a liquid-gas interface with constant surface tension, density gradient and interface thickness. ψ denotes an pseudopotential term and is a function of density, as shown below.

The inter-particle force can be translated into an excess pressure with regard to the expression of ideal gas ($c_s^2\rho$) [87] :

$$-\partial_j P_{ij} + \partial_i(c_s^2\rho) = \boldsymbol{F}_i \tag{2.19}$$

where P_{ij} denotes the total pressure tensor. Then from the above equation, the EOS in the SCMP SC model is obtained by:

$$P = c_s^2\rho + \frac{c_s^2 G}{2}\psi^2 \tag{2.20}$$

where P denotes the thermodynamic pressure.

Yuan and Schaefer [88] demonstrated that for any given EOS, the mean field potential term $\psi(\rho)$ can be written from Eq. (2.19):

$$\psi(\rho) = \sqrt{\frac{2(P - c_s^2\rho)}{c_s^2 G}} \tag{2.21}$$

Various EOS can be incorporated into the SCMP model such as the SC, van der Waals (vdW), Redlich- Kwong (R-K), Redlich- Kwong Soave (RKS), Peng-Robinson (P-R) and Carnahan-Starling (C-S). Yuan and Schaefer [88] compared the performance of these EOS in terms of temperature range, density ratio and spurious current and reported the C-S EOS allows the highest density ratio up to 1400. Therefore, The C-S EOS is applied to obtain the pressure-density relation and this is given by:

$$P = \rho RT\frac{1 + \frac{b\rho}{4} + (\frac{b\rho}{4})^2 - (\frac{b\rho}{4})^3}{(1 - \frac{b\rho}{4})^3} - a\rho^2 \tag{2.22}$$

where T denotes the temperature and is equal $T = T_0 T_C$ where T_0 denotes the reduced temperature and T_C is the critical temperature determined as $T_C = \frac{0.3773a}{bc}$. Following Yuan and Schafer [88]: a=1 $lu^5/(mu.ts^2)$, b=4 lu^3/mu and R =1 $lu^2/(ts^2\,.\,tu)$.

Furthermore, the inter-particle force contributes to a fluid particles momentum $\boldsymbol{F}\tau$. The momentum can reach an equilibrium state $\rho\boldsymbol{u}^{eq}$ after $\Delta t = \tau$ where $\boldsymbol{u}^{eq}$ denotes the equilibrium velocity and replaces with $\boldsymbol{u}$ in Eq. (2.9) to calculate the equilibrium distribution function in the collision step. The equilibrium velocity is calculated as:

$$\boldsymbol{u}^{eq} = \boldsymbol{u} + \frac{\boldsymbol{F}\tau}{\rho} \tag{2.23}$$

Then, the whole fluid velocity $\boldsymbol{U}$ can be determined by averaging the momentum before and after the collision:

$$\rho\boldsymbol{U} = \rho\boldsymbol{u} + \frac{\boldsymbol{F}}{2} \tag{2.24}$$

The interaction with solid nodes can simply be obtained in the SCMP model by giving an artificial wall density ρ_w to solid nodes with a value between the densities of the liquid phase ρ_l and the gas phase ρ_g [87]. As will be shown in next chapter, various equilibrium contact angles based on Young's equation can be achieved by adjusting ρ_w.

In the SCMP model, the surface tension, density ratio and relaxation time depend on each other. Huang et al. [89] demonstrated that the surface tension and the density ratio are a function of T/T_C. They also investigated comprehensively numerical stability in the SCMP model. The interface thickness, which defines the minimum thickness between the liquid bulk and the gas bulk (see Fig. 2.4), plays an essential role in the numerical stability because the SCMP is a diffuse-interface method. This thickness cannot be adjusted explicitly and depends on the other model parameters such as the temperature, relaxation time and the constants *a, b* and *R* in the C-S EOS. To achieve numerical stability in this study, all numerical parameters are chosen carefully based on Huang et al. manuscript [89].

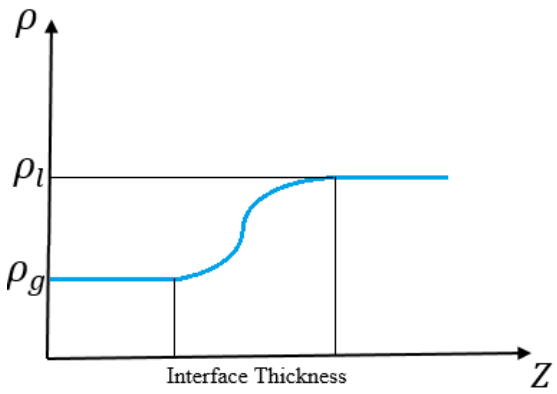

Fig. 2.4. *The interface thickness for two-phase flows.*

2.5 Units in lattice Boltzmann method

Basic units in the LBM consist of *mu* (mass unit) for mass, *lu* (lattice unit) for length, *ts* (time step) for time and *tu* (temperature unit) for temperature. Other units can be derived as a combination of basic units as shown in table 2.1. Generally, non-dimensional numbers such as the Reynolds number and the Weber number can be considered to ensure dynamic similarity and connect lattice quantities with physical ones. The Reynolds matching procedure for gravity driven flow problem was, for example, provided by Sukop and Thorne [72].

Table 2.1. *Units in the LBM*

Variables	**Unit**
Velocity	lu/ts
Density	mu/lu^3
Pressure	$mu/(lu.ts^2)$
Surface Tension	mu/ts^2
Kinematic Viscosity	lu^2/ts

As another example, droplet impact conditions are characterized by the dimensionless Weber number. For a droplet impact simulation, we find a suitable value for the impact velocity in the LBM to correctly match given physical conditions. To make comparable simulations to reality, the Weber number in the physical system which is calculated from experimental data must be equal to the Weber number in the lattice Boltzmann system. As a consequence, the impact velocity in the LBM can be determined from:

$$V_{LBM} = \sqrt{\frac{We_{LBM}\sigma_{LBM}}{\rho_{LBM}D_{LBM}}} \tag{3.25}$$

Where ρ_{LBM} , D_{LBM} and σ_{LBM} are known.

2.6 Computational solver

FORTRAN solvers have been developed using the SCMP lattice Boltzmann method described in the previous section for both two-dimensional and three-dimensional flows. These codes have been compiled by the PGI compiler and all post-processing was done using the Tecplot software. The solvers which have been developed following the SCMP model consists of three main parts:

- Initialising variables:

  The complex flow is modelled on a solution domain which is divided into lattices. Each lattice site is occupied by either a fluid (liquid or gas) node or a solid node. For fluid nodes, an initial velocity u_0 needs to be assigned as well as an initial density ρ_0 which is either the gas density ρ_g or the liquid density ρ_l.

  Moreover, the parameter ρ_w is adjusted based on the surface contact angle as will be discussed in chapter 3. Then the discrete velocities model *DnQm* is chosen and relevant parameters to this velocity model such as $\boldsymbol{e}_k$, c , ω_k and c_s^2 are initialised.

Finally, the relaxation time is set to 1 (in this study) and the initial particle distribution function $f_k(\boldsymbol{x}, t = 0) = f_k^{eq}(\boldsymbol{x}, t = 0) = f_k^{eq}(\rho_0, \boldsymbol{u}_0)$ is assumed.

- Main loop:

  In the collision step the equilibrium distribution functions (f_k^{eq}) are calculated using Eq. (2.9) and then the distribution functions are updated as $f_k^{post}(\boldsymbol{x}, t) = f_k^{eq}(\boldsymbol{x}, t)$ as the relaxation time is unity.

  Furthermore, for solid nodes the bounce back boundary condition is applied. In the streaming step the distribution functions are propagated as $f_k(\boldsymbol{x} + \boldsymbol{e}_k \Delta t, t + \Delta t) = f_k^{post}(\boldsymbol{x}, t)$. During propagation, for the lateral sides of the simulation domain the periodic boundary condition is implemented as the distribution functions reach the end of the region.

  Next, the macroscopic quantities ρ and $\boldsymbol{u}$ are obtained using Eqs. (2.10) and (2.11). Then, the pressure is calculated through the C-S EOS which is described by Eq. (2.22) and as a consequence the pseudopotential term $\psi(\rho)$ is determined from Eq. (2.21). Now the interaction forces between the solid and fluid nodes (adhesive force) and between fluid nodes (cohesive force) can be calculated using Eq. (2.18). Note that for the inter-particle forces between solid nodes and fluid nodes the parameter ρ_w is used. Finally, the equilibrium velocity is determined via Eq. (2.23) and then the equilibrium distribution function Eq. (2.9) is updated by this velocity in the collision step in the next loop.

- Post-processing stage including plotting the density contours.

During the simulations, the default values of gas density and liquid density are 0.0285 mu/lu^3 and 0.285 mu/lu^3, respectively. The effect of gravity is neglected in this study. The computational algorithm is summarized in Fig. 2.5.

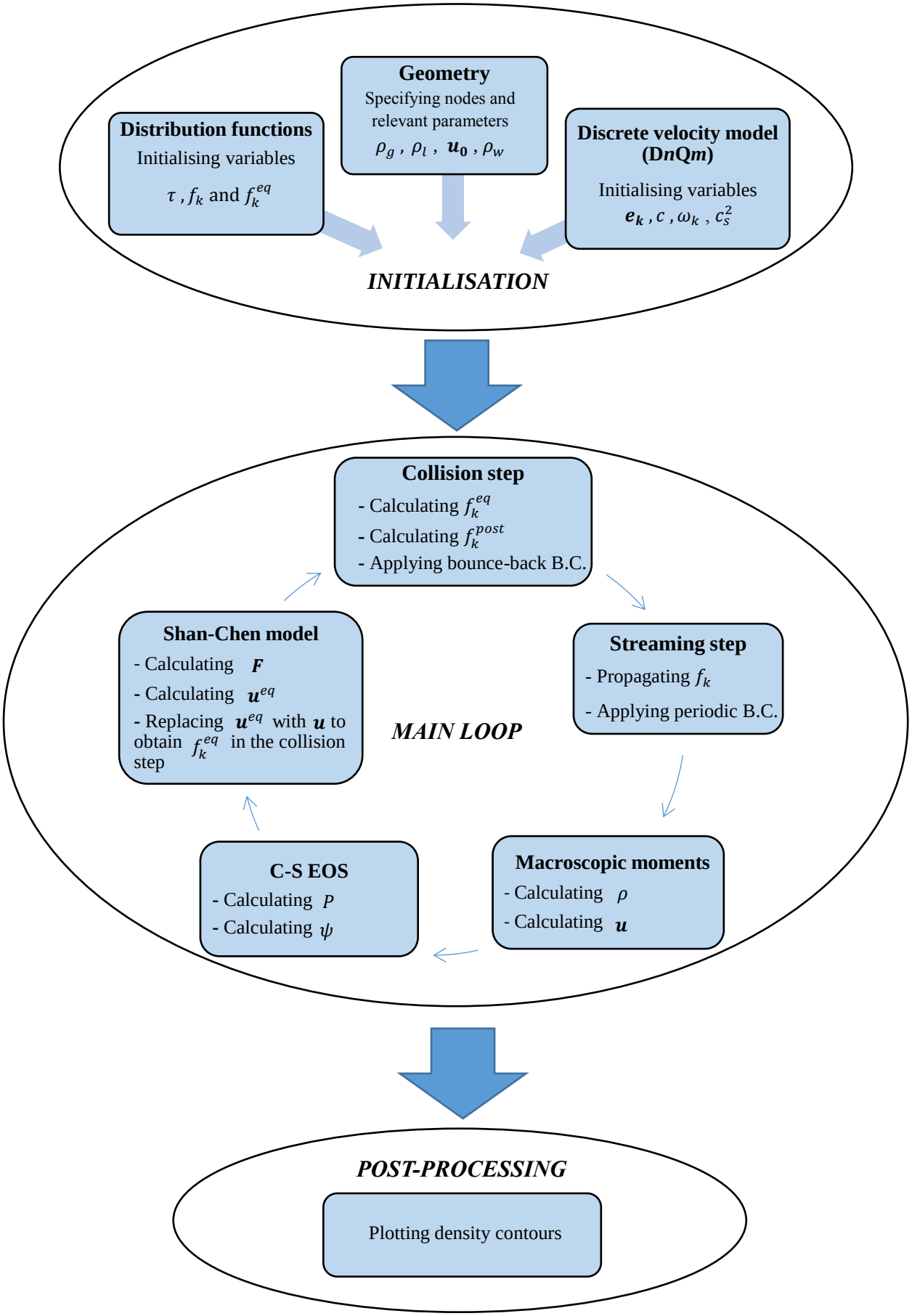

Fig. 2.5. *Schematic of the computational algorithm.*

2.7 Summary

The lattice Boltzmann method (LBM) has emerged as a mesoscopic approach for modelling multi-phase flows and interfacial dynamics problems. The fundamental idea of the LBM is to solve numerically the Boltzmann equation. The discrete lattice Boltzmann equation consists of a streaming step and a collision step. The main variable is the density distribution function $f_k(\boldsymbol{x}, t)$ which represents the state of a fluid parcel. To consider inter-particle forces between nodes, the single-component multiphase (SCMP) Shan-Chen (SC) model is implemented.

The algorithm which has been developed following the SCMP model includes three main parts: firstly initialising variables and nodes, secondly a main loop involving the collision step, the streaming step, applying boundary conditions (the bounce-back and the periodic boundary conditions), calculating macroscopic quantities, determining pressure and forces and then obtaining the equilibrium velocity to update distribution functions in the next loop and finally a post-processing stage including plotting the density contours. The LBM has the benefits of both the macroscopic and microscopic approaches which means that this method can solve complex multiphase flows problems with reliable accuracy in both macro and micro scales. Thus, the LBM has become a powerful CFD tool for simulating multiphase flows problems such as wetting phenomena which is the reason we chose it for the flows which will be considered in the forthcoming chapters.

Chapter 3

3. Validation and test cases

This chapter describes four validation cases to demonstrate the ability of our lattice Boltzmann code for simulating wetting phenomena. All validation cases involve the study of a drop impact onto a smooth solid surface. In such impacts several distinctive features are observed including the equilibrium contact angle, the maximum spreading diameter for both normal and oblique drop impacts and the thickness of the lamella at maximum spread. These numerical results are compared with relevant well-known relations which have been previously reported.

3.1 Equilibrium contact angle

The modelling of the equilibrium contact angle on a smooth surface is carried out as the first validation case. Various contact angles based on Young equation (Eq. (1.1)) can be achieved numerically by adjusting the parameter ρ_w. In 2D simulations, the size of the computational domain is 300 lu by 60 lu and the initial radius of the droplet is 20 lu. Initially, the liquid droplet which is in contact with the surface is left to spread spontaneously. After reaching an equilibrium state, the contact angle is measured manually with a protractor. The results for the droplet with different angles 145°, 110°, 90°and 60° are shown in Fig. 3.1.

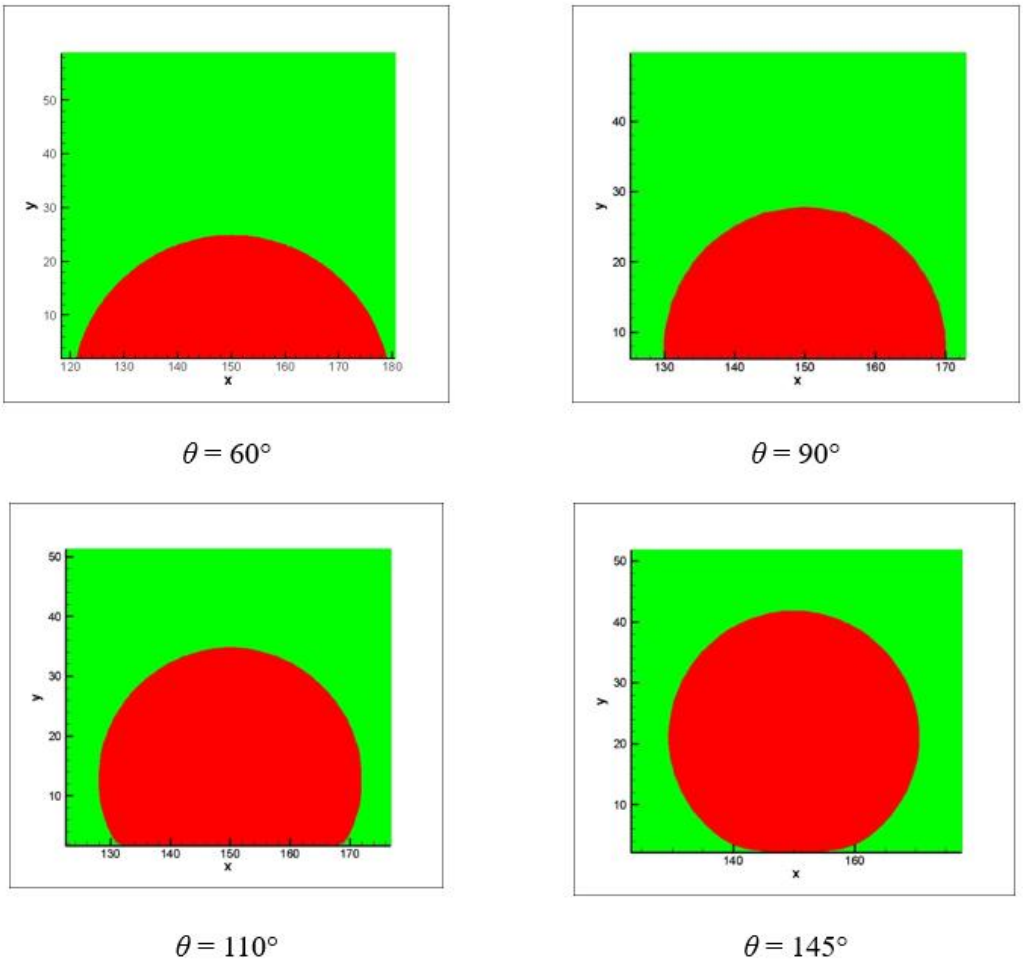

Fig. 3.1. *2D numerical simulations of different static contact angles on a smooth surface obtained by adjusting the artificial wall density (ρ_w)*

We now compare the equilibrium contact angle predicted by the numerical simulation with the analytical solution which was reported by Benzi et al. [87]. The authors estimated analytically the contact angle in terms of ρ_w by taking the integral of the density profile along the solid-gas, solid-liquid and liquid-gas interfaces. They also compared this relation with their numerical results in figure 3 of Ref [87].

Since ρ_w is an artificial parameter in the SCMP model, we choose here to represent the results using a normalized surface affinity parameter which is more physical and can be defined as [56]:

$$\eta = \frac{\rho_w - \rho_g}{\rho_l - \rho_g} \tag{3.1}$$

where η=0 (no affinity) and η=1(high affinity) correspond to the equilibrium contact angles of 0 and 180, respectively.

Fig. 3.2 compares the equilibrium contact angle-affinity curve (θ vs η) obtained numerically from the simulations to the analytical solution of Benzi et al. [87] (see figure 3 of the paper) for the parameter set stated earlier. The graph shows that for both cases, the equilibrium contact angle decreases when the wall density increases which corresponds to an increase of the affinity parameter. It can be seen that a good agreement is found between the numerical and analytical results. The non-smooth nature of the curve for the numerical results is attributed to the uncertainty associated with measuring the contact angle with a protractor. Note that a similar rugged curve is observed in the numerical results of Benzi et al. [87].

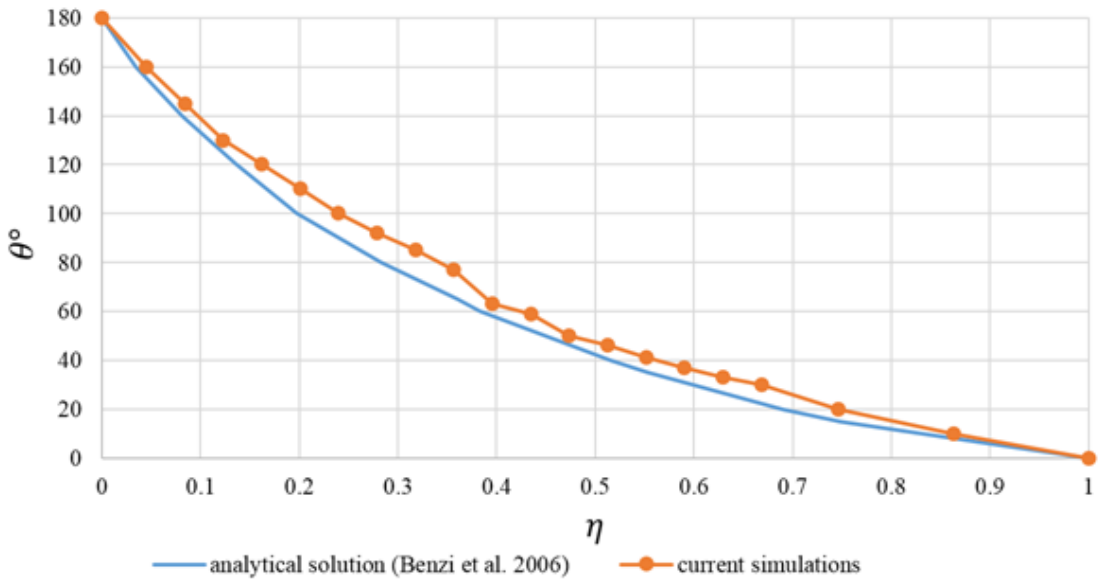

Fig. 3.2. *Comparison between the 2D current simulations (—●—) and the analytical solution [87] (———).*

3.2 Maximum spreading factor

As mentioned in the literature, the maximum spreading diameter D_{max} is a significant measurable outcome of a drop impact onto a solid surface. When the spreading lamella of an impacting droplet reaches its largest extent on a surface, D_{max} is measured based on both side of the lamella. This parameter can be normalized with the initial drop diameter (D) as follows:

$$\xi = \frac{D_{max}}{D} \tag{3.2}$$

Where ξ denotes the maximum spreading factor.

Scheller and Bousfield [39] developed an empirical relationship based on the Reynolds and Weber numbers to predict the maximum spreading factor:

$$\xi = 0.61\ \mathrm{Re}^{1/5}\ (\mathrm{We}\ \mathrm{Re}^{-2/5}\ )^{1/6} \tag{3.3}$$

As the second validation case, we have simulated in 2D the normal impact of a droplet with an initial diameter of ($D = 65\ lu$) on a smooth solid surface with an equilibrium contact angle of $\theta = 90°$ for a range of velocities ($40 \leq \mathrm{Re} \leq 155$) and calculated the maximum spreading diameter. We have then compared our numerical results with the above correlation. The comparison is shown in Fig. 3.3. It can be seen that good agreement is found between the numerical results and Scheller and Bousfield's correlation [39]. The maximum error of 8.47% occurs for the largest tested Reynolds number of 155 and Weber number of 270.

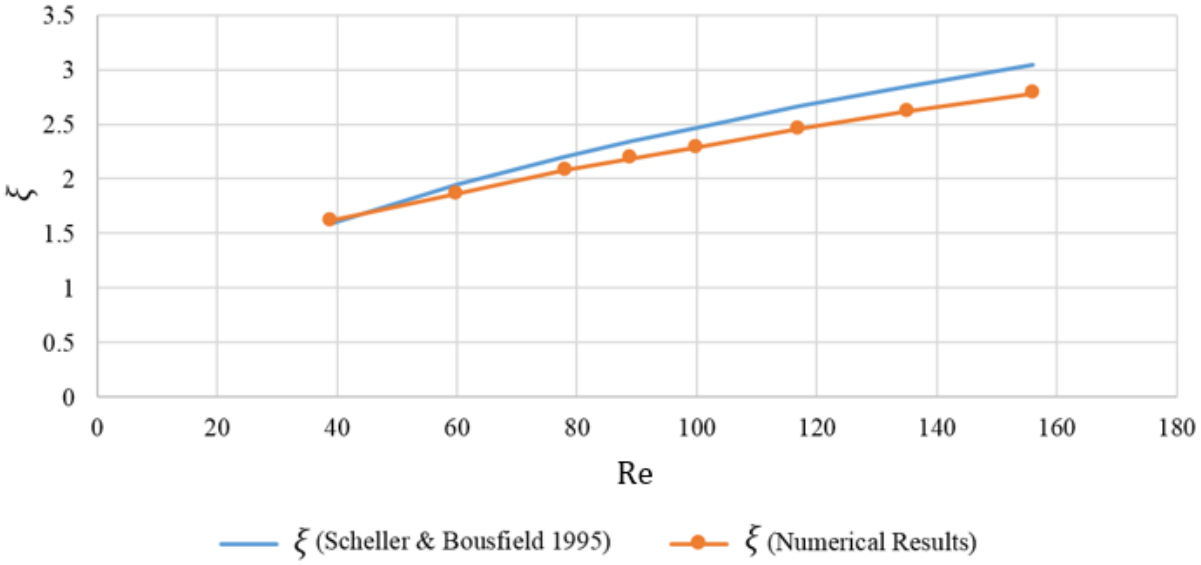

Fig. 3.3. *Comparison between the maximum spreading factor computed numerically in 2D (—●—) and Scheller and Bousfield [39] correlation (———). The error increases from 1.32% for a Reynolds number of 40 and a Weber number of 18 to 8.47 % for a Reynolds number of 155 and a Weber number of 270.*

3.3 Lamella thickness at maximum spread

Firstly, in order to find an accurate spatial resolution, the spreading of an impacting droplet on a flat substrate is simulated for two different spatial resolutions including $L_X \times L_Y \times L_Z =$ $130\times130\times45$ lu^3 and $260\times260\times90$ lu^3. The diameter of the droplet is $D = \frac{L_X}{4}$ lu. Three-dimensional simulations are performed for a Reynolds number of 39 and a Weber number of 18. To achieve the same dimensionless numbers, the relaxation time is set to $\tau = 0.85\Delta t$ for $L_X \times L_Y \times L_Z = 130\times130\times45$ lu^3 and $\tau = \Delta t$ for $L_X \times L_Y \times L_Z = 260\times260\times90$ lu^3.

Fig. 3.4 illustrates the simulation results of the spreading lamella at maximum spread. For $L_X \times L_Y \times L_Z = 130\times130\times45$ lu^3 and $L_X \times L_Y \times L_Z = 260\times260\times90$ lu^3 the maximum spreading factor are $\xi = 1.815$ and $\xi = 1.615$, respectively.

We then determine this factor through Scheller and Bousfield [39] empirical correlation (Eq. (3.3)). For a Reynolds number of 39 and a Weber number of 18, the maximum spreading diameter factor is $\xi = 1.609$. Comparing ξ computed numerically and Scheller and Bousfield [39] correlation (Eq. (3.3)) shows that when the spatial resolution is refined, from $130\times130\times45$ lu^3 to $260\times260\times90$ lu^3, the maximum spreading diameter factor is increasingly closer to the corresponding correlation of Scheller and Bousfield [39] (Eq. (3.3)) and the error is marginal.

Hence, we will apply the 260×260×90 lu^3 spatial resolution to capture reliable 3D numerical results in the reminder of this thesis.

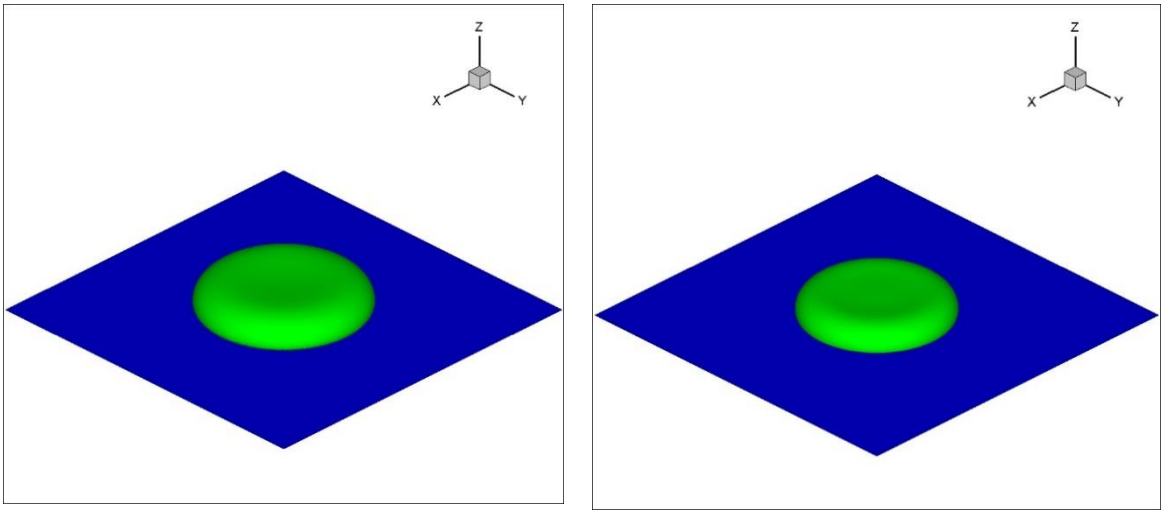

(a) (b)

Fig. 3.4. *3D simulation results for two various spatial resolutions (a) 130×130×45 lu^3 and (b) 260×260×90 lu^3. For both cases the Reynolds number and the Weber number are 39 and 18, respectively.*

Now, to obtain analytically the lamella thickness at maximum spread, a cylindrical shape for the lamella at maximum spread is considered as shown in Fig. 3.5. A mass balance of the droplet before impact and at maximum spread can be written as:

$$\rho \frac{\pi}{6} D^3 = \rho \frac{\pi}{4} D_{max}^2 h_l \tag{3.4}$$

where h_l is the thickness of lamella at maximum spread.

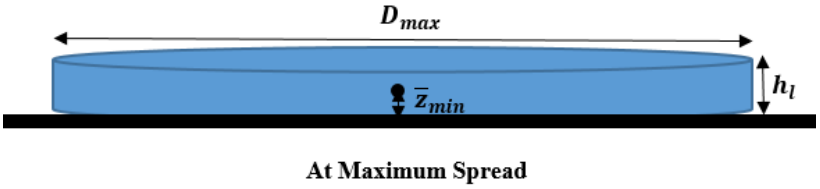

Fig. 3.5. *A cylindrical shape for the lamella at maximum spread with a diameter of D_{max} and a height of h_l. Maximum spread occurs as the centre of gravity hits a minimum. $\bar{z}_{min}$ denotes the minimum of the centre of gravity on the z-axis.*

Simplifying Eq. (3.4) yields:

$$h_l = \frac{2D}{3\xi^2} \tag{3.5}$$

where ξ is given by Eq.(3.3). Subsuming Eq. (3.3) into Eq. (3.5) and therefore:

$$h_l = \frac{2D}{3[0.61\ \mathrm{Re}^{\frac{1}{5}}\ (\mathrm{We}\ \mathrm{Re}^{-\frac{2}{5}})^{\frac{1}{6}}]^2} \tag{3.6}$$

Next, 3D simulations are carried out for a spherical droplet with a given diameter $D = 65\ lu$, an initial velocity V which impacts, spreads and recoils onto a flat substrate with an equilibrium contact angle of $\theta = 90°$. The centre of gravity of a droplet on the z-axis ($\overline{z}$) during impact, spreading and retraction is computed by the lattice Boltzmann solver according to:

$$\overline{z} = \frac{\sum z_0(\rho - \rho_g)}{\sum(\rho - \rho_g)} \tag{3.7}$$

where $\overline{z}$ is the centre of gravity and z_0 denotes the distance from the origin. This parameter helps us calculate the thickness of the lamella at maximum spread time.

Maximum spread occurs as the centre of gravity hits a minimum. As Fig. 3.5 illustrated, the thickness of the lamella is assumed to be twice the distance between centre of gravity and the substrate:

$$h_l = 2\,\overline{z}_{min} \tag{3.8}$$

where $\overline{z}_{min}$ denotes the minimum height of centre of gravity. The centre of gravity for three different cases with various Reynolds and Weber numbers is plotted in Fig. 3.6.

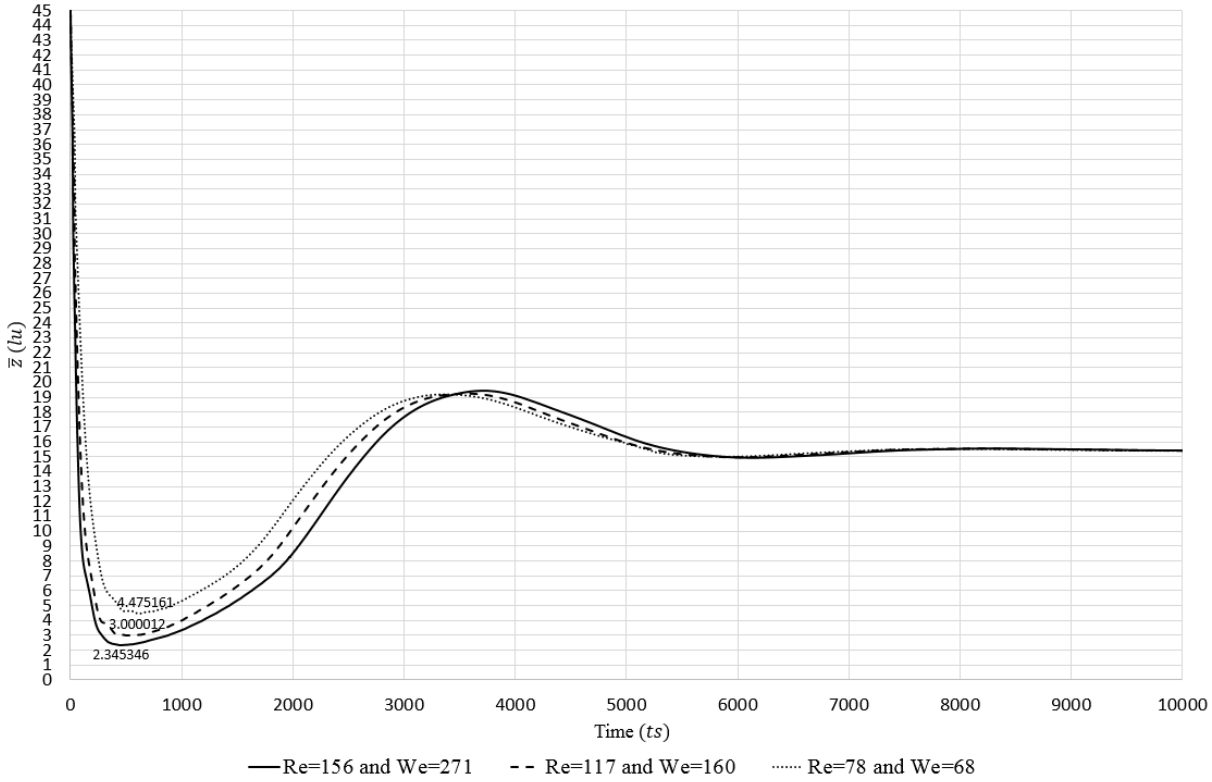

Fig. 3.6. *This plot demonstrates the location of the centre of gravity on the z-axis ($\overline{z}$) as the droplet falls, impacts, spreads and retracts on the substrate without occlusion. At maximum spread, the centre of gravity hits a minimum. The minimum amount of $\overline{z}$ shows for each graph. The thickness of the lamella is assumed to be twice this minimum.*

For the third validation case, we compare the thickness of the lamella determined using the centre of gravity with the corresponding results when using the Scheller and Bousfield [39] correlation described in Eq. (3.6). As table 3.1 illustrates, a good agreement is found between the Lattice Boltzmann simulation results and the correlation with the error being less than 1%.

Table 3.1. *Comparison of the lamella thickness at maximum spread between Scheller and Bousfield [39] correlation (using Eq. 3.3) and the numerical solution in 3D (using centre of gravity in z-axis)*

Re	We	h_l analytical solution (lu)	h_l numerical solution (lu)
78	68	8.92	8.95
117	160	6.02	6
156	271	4.68	4.69

3.4 Maximum spreading factor for oblique impacts

For an oblique impact, the maximum spread factor is the outcome of an asymmetric behaviour created by the tangential component of the impact velocity. Since the tangential momentum affect such drop impacts, a normal and tangential Weber number is defined through the normal impact velocity V_n and the tangential impact velocity V_t:

$$\mathrm{We}_n = \frac{\rho {V_n}^2 D}{\sigma} \tag{3.9}$$

$$\mathrm{We}_t = \frac{\rho {V_t}^2 D}{\sigma} \tag{3.10}$$

The impact angle, illustrated in Fig. 3.7, is defined as:

$$\Phi = \tan^{-1} \frac{V_n}{V_t} \tag{3.11}$$

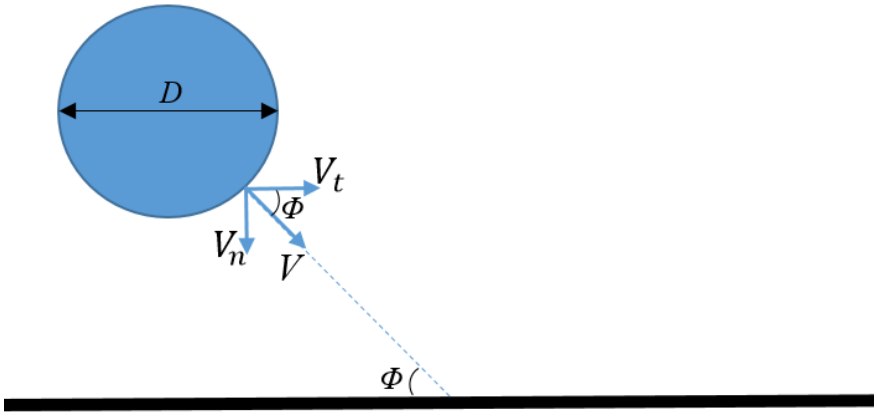

Fig. 3.7. *Schematic of an oblique impacting droplet with a diameter of D and an impact angle Φ onto a substrate. V, V_n and V_t denote the impact velocity, the normal and tangential components of the impact velocity, respectively.*

Yeong et al. [57] obtained an experimental relationship between the maximum spread factor $\xi = \frac{D_{max}}{D}$ and the Weber numbers:

$$\xi = 0.9\ \mathrm{We}_n{}^{0.25} + C\ \mathrm{We}_t \tag{3.12}$$

where C is a constant equal to 0.005. It should be noted that this correlation is valid for $\mathrm{We}_n < 60$ since break-up occurs beyond this value.

We now model in 2D the impact of a droplet with a diameter of $D = 200\ lu$ and impact velocity V under an initial impact angle Φ=30° onto a smooth substrate with an equilibrium contact angle of $\theta = 150°$. Fig. 3.8 shows the droplet at maximum spread when the Weber number is 50. For this case, the non-dimensional maximum spread calculated via correlation 15 yields 3.14, while our simulation gives 3.17 (error is around 1%).

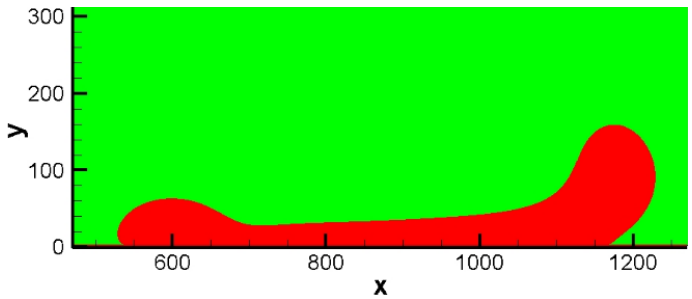

Fig. 3.8. *2D Numerical simulation of the maximum spread of a droplet when the normal Weber number and the impact angle are 50 and 30°, respectively.*

Numerical simulations are performed for a various range of the normal Weber numbers from 10 to 50. A comparison between the normalized maximum spread determined numerically (the blue line) and Eq. (3.12) (the black spot) is shown in Fig. 3.9. It can be seen that a good agreement is found. The maximum error is 3.7% as Φ=10°.

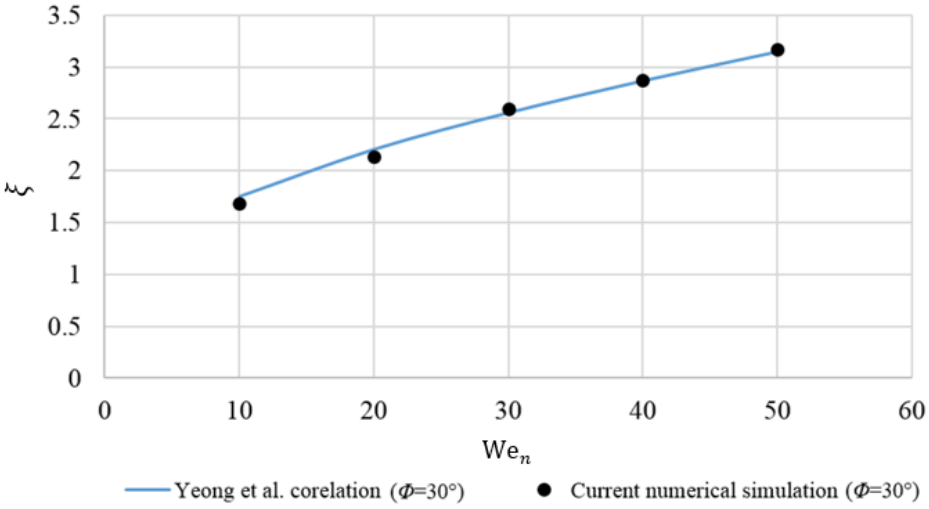

Fig. 3.9. *Comparison between the current numerical simulations in 2D and the correlation reported by Yeong et al. [57] for the maximum spread of an oblique impact drop on a super-hydrophobic surface when the impact angle is 30°.*

3.5 Summary

In order to validate the correct implementation of our LBM solver, the simulation of a drop impact onto a flat surface has been performed and three different measurable outcomes including the equilibrium contact angle (in 2D), the maximum spreading diameter (in 2D) and thickness of lamella at maximum spread (in 3D) have been calculated.

The equilibrium contact angle was considered as a static validation case. Numerical results reported that equilibrium states on a smooth surface are correctly predicted. Besides, for the maximum spreading diameter the 2D numerical results have been compared with Scheller and Bousfield' correlation [39] (Eq. (3.3)) and a good agreement was found with a maximum error of 8.47%. The LBM solver in 3D has been also verified with a comparison between the numerical results for the thickness of lamella at maximum spread (Eq. (3.8)) and the corresponding correlation of Scheller and Bousfield [39] (Eq. (3.3)). The error was found to be less than 1%. Finally, we performed simulations in 2D to calculate the maximum spread for an oblique impacting droplet onto a smooth surface. The numerical results have been successfully compared with a correlation (Eq. (3.12)) reported by Yeong et al. [57].

Chapter 4

4. Interaction between the wetting front and a microscopic ridge*

This result chapter investigates the conditions under which a spreading lamella surmounts a small surface ridge. Three basic outcomes have been observed when the lamella comes into contact with the ridge: pinning, wetting and splashing. For each of the potential outcomes, a side-by-side comparison with the experimental results obtained by Dr G.R. Willmott and M. Broom using high speed photography is carried out. The effects of the Weber number and the dimensionless distance between the impact point and the ridge are investigated and a phase portrait of the different wetting outcomes is presented. An energy balance approach is used to study the transition between the different outcomes.

* This chapter is a collaborative effort with Dr G.R. Willmott and his PhD student M. Broom from the university of Auckland. The author of this thesis, Hossein Rashidian, has performed all the simulations and contributed to the analysis and discussion parts.

4.1 Problem specification

The lamella-ridge interaction is especially relevant in two areas that have recently been prominent in the literature. Firstly, researchers have noted the ability to reduce a droplet contact time by direct impact on a thin hydrophobic ridge [90-91]. In applications where the drop incidence is stochastic, droplets will more commonly impact the surface some distance away from a ridge, after which a spreading lamella will impact the ridge from the side [92]. A related problem is the spread of a lamella on or near vascular bundles (veins) on leaves, which can produce asymmetric drop outcomes [10].The second area of specific relevance concerns the interplay between spreading dynamics and the Cassie-Baxter and Wenzel states, which are more familiar from quasi-static wetting. Drop impact experiments have shown that a lamella can transition from fully penetrating a microstructure to spreading over the top of the pillars [93-95]. This transition is similar to a lamella moving over a ridge, studied in this chapter.

To gain a greater understanding of drop impacts near individual topographical features, in this chapter, we focus on the interaction between the edge of the spreading lamella and a micron-sized ridge on a flat surface as shown in Fig. 4.1 where D denotes the initial diameter of the droplet, V the impact velocity, L the distance parallel to the surface from the edge of the ridge to the centre of the droplet, and W and H are the width and height of the ridge, respectively. We investigate the influence of two important control parameters on the wetting outcomes: the dimensionless distance from the impact point to the ridge L/D and the Weber number We.

2D Numerical simulations are performed for Weber numbers in the range $25 < \mathrm{We} < 350$, and for impact points such that $0.5 \leq L/D \leq 2$. Note that if $L/D \leq 0.5$, part of the drop lands directly on the ridge, a situation not studied here. The equilibrium contact angle is $\theta = 110°$ and the effect of gravity is negligible due to the Bond number being small.

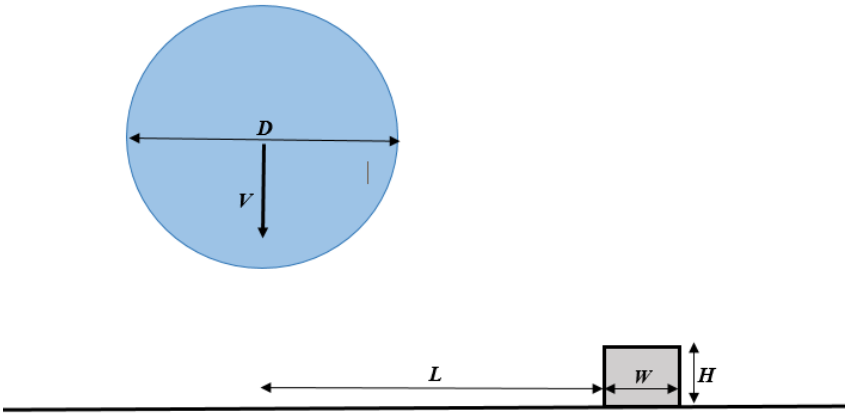

Fig. 4.1. *Schematic of a drop impacting on a surface with a single ridge.*

4.2 Classification of outcomes

We define the outcome of the drop impact at the moment when the lamella is at maximum spread, immediately prior to recoil. Three basic outcomes have been observed. Firstly, the advance of the lamella may be arrested before the drop reaches the far side of the ridge, an outcome labelled as pinning (Fig. 4.2). The lamella may spread and touch the ridge without extending horizontally beyond the ridge, or it may extend beyond it, but start to recoil prior to touching the surface on the other side. Wetting, the second outcome, occurs when the drop spreads on to the surface beyond the ridge without breaking-up (Fig. 4.3). In some wetting cases, the lamella first makes contact with the surface on the far side at some distance from the edge of the ridge. The third outcome is splashing, when smaller drops are generated from the lamella edge while the lamella is in contact with the ridge, prior to the onset of lamella retraction (Fig. 4.4).

Figs. 4.2, 4.3, and 4.4 provide a side-by-side comparison for the three different outcomes. In each figure, four steps during droplet impact are shown: (i) impact, when the droplet strikes the surface; (ii) as the droplet begins to spread; (iii) when the droplet first touches the ridge; and (iv) the droplet at maximum spread, when the outcome of the impact is determined.

Simulations and experiments show good qualitative agreement, although there are observable differences. For example, in Fig. 4.4 the simulated splashing angle is smaller than the angle observed in experiments, an observation previously reported by Josserand et al. [54]. It can also be seen that the size of the satellite drop in simulations is larger than the ejected drops in experiments. Moreover, free surface perturbations can be observed experimentally in the wetting case, while these are absent in simulations.

Several factors may explain these differences. Firstly, simulations are 2D; this point will be discussed further in the next section. Secondly, the density ratio in simulations is significantly different from the experimental case due to limitations of the SCMP lattice Boltzmann method. It should be noted that simulations have the density ratio of 10, whereas this ratio is 1000 for experiments. Thus, simulations are not able to capture the smaller length scale effects entirely.

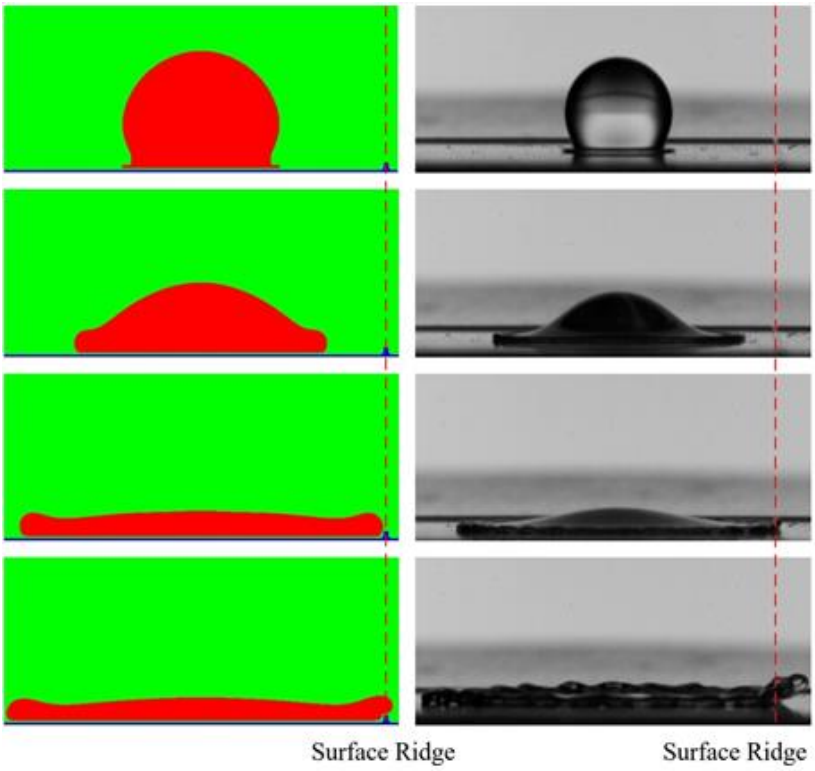

Fig. 4.2. *Side-by-side comparison of numerical (left) and experimental (right) results for the pinning outcome, both obtained for* $\frac{L}{D}$*=1.48 and* We*=144. In the photographs, the red dashed line indicates the position of the ridge.*

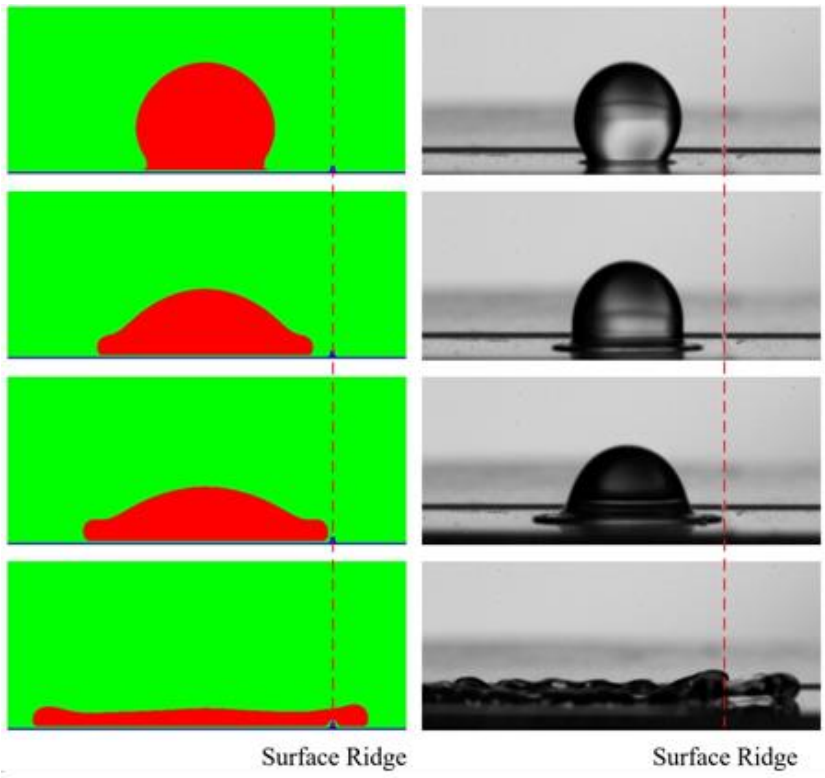

Fig. 4.3. *Side-by-side comparison of numerical (left) and experimental (right) results for the wetting outcome, both obtained for* $\frac{L}{D}$*=0.91 and* We*=142. In the photographs, the red dashed line indicates the position of the ridge.*

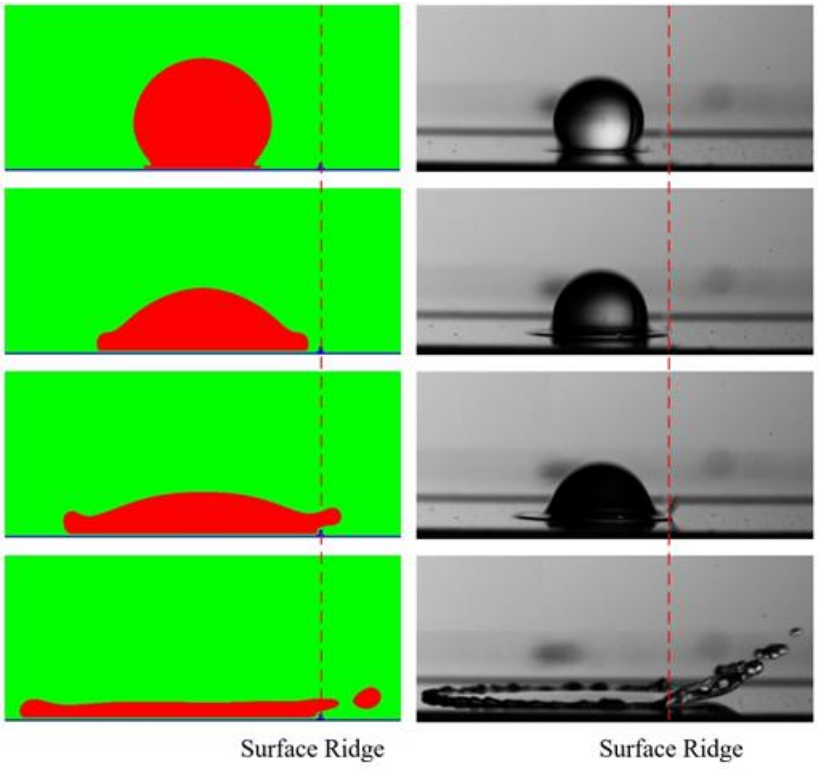

Fig. 4.4. *Side-by-side comparison of numerical (left) and experimental (right) results for the splashing outcome, both obtained for* $\frac{L}{D}$*=0.86 and* We*=237. In the photographs, the red dashed line indicates the position of the ridge.*

4.3 Energy approach for analysing transitions

When the droplet meets the ridge, the outcome should be predominantly governed by competition between the kinetic and surface energies. Therefore, a simple energy balance approach is used to study the dependence of the pinning-wetting transition on L/D and We. The model is based on an estimate for the maximum spread of an impacting droplet [96-97], in which the reduction in kinetic energy following impact is equated to the extra surface energy produced in deforming the droplet. This analysis allows us to compare 2D and 3D models, and therefore to address the differences between the experimental and simulation data.

The method is approximate because energy losses due to viscous dissipation (known to be significant in drop spreading [98]) are neglected, and because the spreading drop is modelled as a cylindrical disc with the liquid-vapour surface tension applicable on all surfaces. However, we do account for the initial surface energy, which was neglected in Collings et al.'s model [96] that yields the widely-used result that the maximum spreading diameter scales $\propto We^{0.5}$ [48].

For this energy balance approach, the kinematic energy (KE_1) and surface energy (SE_1) prior to impact are equated to the sum of these energies at maximum spread:

$$KE_1 + SE_1 = KE_2 + SE_2 \tag{4.1}$$

where KE_2 and SE_2 denote the kinetic energy and surface energy at maximum spread, respectively. Given that the velocity is zero at maximum spread therefore $KE_2 = 0$.

If a 2D droplet of density ρ and surface tension γ spreads to its maximum extent, forming a strip of height h_l and the length D_{max}, this energy balance gives:

$$\frac{1}{2}\rho V^2\pi\left(\frac{D}{2}\right)^2 + \pi D\gamma = 2\gamma(h_l + D_{max}) \tag{4.2}$$

h_l can be determined by a mass balance of the droplet before impact and at maximum spread:

$$h_l = \frac{\pi}{D_{max}}\left(\frac{D}{2}\right)^2 \tag{4.3}$$

Substituting Eq. (4.3) into Eq. (4.2) and therefore:

$$\frac{\pi}{8}\rho V^2 D^2 = \gamma\left(\frac{\pi D^2}{2D_{max}} + 2D_{max} - \pi D\right) \tag{4.4}$$

Eq. (4.4) can be rewritten as:

$$\frac{\rho V^2 D}{\gamma} = \left(\frac{16D_{max}}{\pi D} + \frac{4D}{D_{max}} - 8\right) \tag{4.5}$$

The left hand side of Eq. (4.5) is more commonly known as the Weber number and therefore:

$$\mathrm{We} = \frac{16D_{max}}{\pi D} + \frac{4D}{D_{max}} - 8 \tag{4.6}$$

In this investigation, we assumed that the pinning-wetting transition occurs at some spreading diameter smaller than D_{max}, so that $2L = ND_{max}$ where $0 < N \leq 1$. Using the constant N allows us to make a simple fit to the simulated and experimental data. Therefore, N denotes a fitting parameter.

Applying this relation with Eq. (4.6), the relation can be obtained for 2D:

$$\mathrm{We} = \frac{32L}{N\pi D} + \frac{2ND}{L} - 8 \tag{4.7}$$

Following a similar method to the 2D case, the relationship between We and L/D in a 3D model can be investigated. In 3D, if the drop at maximum forms a cylindrical disc of height h_l and diameter D_{max}, the energy balance is:

$$\frac{1}{2}\rho V^2 \frac{4}{3}\pi\left(\frac{D}{2}\right)^3 + 4\pi\gamma\left(\frac{D}{2}\right)^2 = \pi\gamma(h_l D_{max} + \frac{D_{max}^2}{2}) \tag{4.8}$$

h_l can be determined by a mass balance of the droplet before impact and at maximum spread:

$$h_l = \frac{2D^3}{3D_{max}^2} \tag{4.9}$$

Substituting Eq. (4.9) into Eq. (4.8) and considering the definition of weber number:

$$\mathrm{We} = \frac{6D_{max}^2}{D^2} + \frac{8D}{D_{max}} - 12 \tag{4.10}$$

As in the 2D case, we assumed that the transition occurs at $2L = MD_{max}$ where $0 < M \leq 1$. Following Eq. (4.10), we obtain for the 3D case:

$$\mathrm{We} = \frac{24L^2}{M^2D^2} + \frac{4MD}{L} - 12 \tag{4.11}$$

4.4 Phase portrait of outcomes

A phase portrait of the experimental and simulated wetting outcomes is shown in Fig. 4.5. Describing the thresholds for transition between the pinned, wetting and splashing outcomes is of particular interest. Solid lines indicate transitions from pinned to wetting outcomes in both simulations and experimental results. Dashed lines show transitions from wetting to splash outcomes.

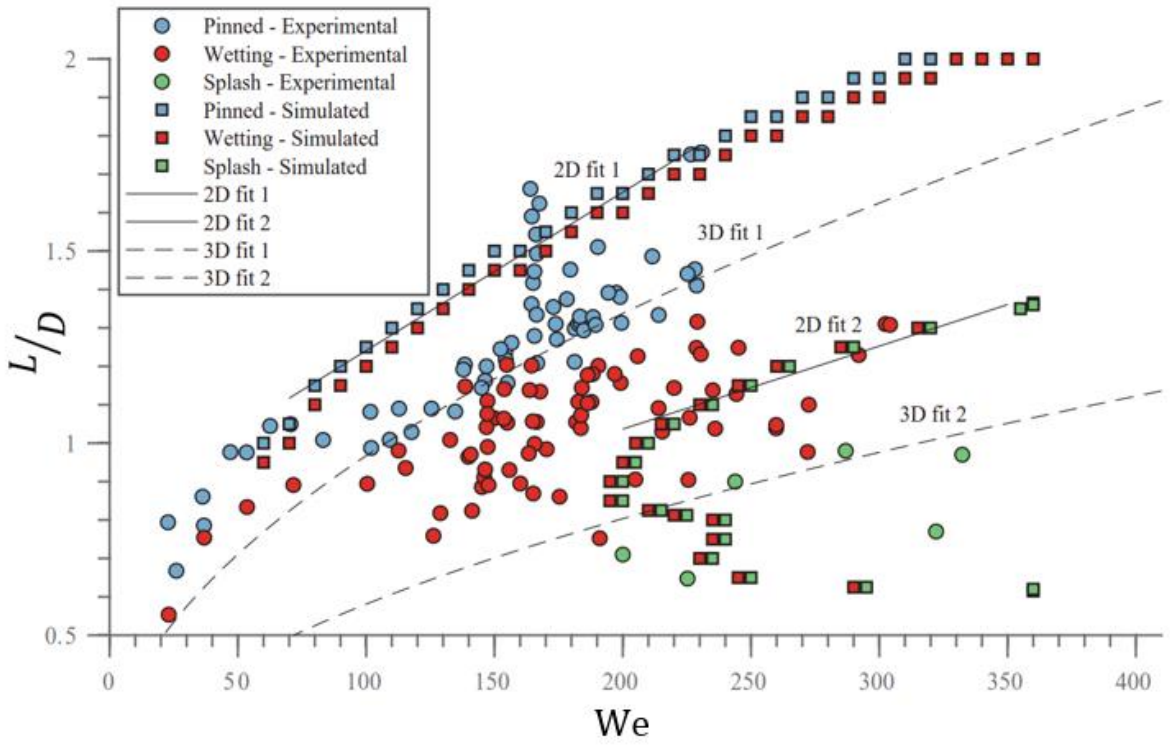

Fig. 4.5. *Phase portrait of the wetting outcomes. The solid lines are fits to the simulation data using a 2D model over the ranges of Weber number shown (Eq. 4.12. Fit1: N=0.042, Q=193. Fit 2: N=0.022, Q=272). The dashed lines are fits to the experimental data using a 3D model (Eq. 4.11. Fit1: M=0.45. Fit 2: M=0.27).*

For the experimental cases, lines are fitted with a least squares method to calculate the best value of M using Eq. (4.11). For the simulations, a similar method was used to find N, although Eq. (4.7) was modified to

$$\mathrm{We} = \frac{32L}{N\pi D} + \frac{2ND}{L} - 8 - Q \tag{4.12}$$

Inclusion of the constant parameter Q is necessary because the simple 2D model, Eq. (4.7), gives imaginary values of L/D near the origin ($We < 17$). Physically, this is because the model does not account for spreading driven by gravity or surface-liquid interactions at low We.

Firstly considering the boundary between the pinning and wetting outcomes in Fig. 4.5, it is clear that the energy required to surmount the ridge is reduced as the distance from the ridge decreases. The 3D fit using our simple model gives a good description of the experimental transition, and predicts that the transition occurs at slightly less than half the distance to maximum spread. Eq. (4.11) gives $L/D \propto We^{0.5}$ to first order, in agreement with the widely used results for maximum spread which uses a similar analytic approach [96].

Qualitatively, the experimental results are consistent with simulations, although direct quantitative comparison is not appropriate because the simulations are carried out in 2D. For example, the spreading 2D drop meets the ridge along a line, whereas the 3D drop first touches the ridge at a point. The fit to the simulation data using the 2D model (Eq. 4.12) can be used to effectively describe the pinning/wetting transition over a limited range of We. The model is limited by the lack of a solution at low We (mentioned above), and because viscous effects have been neglected.

Similar results are obtained for the transition from wetting to splash in Fig. 4.5. The closer to the ridge the droplet impacts, the more likely it is to retain enough energy after surmounting the ridge to break up into droplets. The experimental data suggest that this transition occurs when the ridge is about 0.27 of the distance to theoretical maximum spread.

Interestingly the simulation data are non-monotonic, and suggest that a wetting to splashing occurs at low value of L/D. In the simulations, drop travelling at high velocity and landing close to the ridge immediately wet the surface beyond the ridge, and do not break-up. When a drop has slightly further to travel before reaching the ridge, it will break-up and splash. This

transition was not observed in experiments, and probably reflects the importance of inertia and small length scales in the drop breakup dynamics when the drop lands very near the ridge. It is also possible that wetting outcomes (without splashing) could be observed in experiments close to $L/D = 0.5$ at high We. The upper branch of the simulated wetting-splashing transition is qualitatively similar to the experimental result, although quantitative agreement is not found for similar reasons to the pinning-wetting transition.

The analytic approach used to define the transitions in Fig. 4.5 has recognized limitations [48], in addition to the issue noted above for the 2D case at low We. In particular, viscous dissipation is neglected, and this generally accounts for about half the energy loss in more sophisticated analytical approaches [98]. Also, our approach has not accounted for the surface energy at the solid-liquid interface. A comparison with the model at the Collings et al. [96] which includes the contact angle for a spherical cap, suggests that this omission would not strongly affect the results we have obtained.

4.5 Summary

In this chapter, we have carried out the multiphase Lattice Boltzmann simulations to investigate the interaction between the edge of an impacting water drop and a microscopic ridge. The simulation results have been compared with high-speed imaging experiments which have been performed by Dr G.R. Willmott and his PhD student M. Broom at the University of Auckland.

Experimental and simulation outcomes have been categorised as pinning, wetting and splashing when the lamella is at maximum spread. A simple model based on energy conservation has been developed to predict outcomes as a function of the Weber number and the distance from the impact point to the ridge (L/D). This model gives a good description of the pinning-wetting and wetting-splashing transition. Identification of these transitions can

assist with the study and design of surface microstructures which passively control the outcomes of drop impact events.

When comparing the 2D numerical results with the experimental data, there is good qualitative agreement for each of the three classified outcomes. There is a clear pathway towards improvement of the simulations based on comparison with the experiments. For example, differences in the wetting front dynamics were observed because the simulations do not entirely capture smaller length scale effects (the simulations assumed a liquid to gas density ratio of 10 which is smaller than the density ratio of 1000 in the experiments). The 2D energy conservation model only produces a reasonable fit to transition thresholds over limited ranges of Weber number. Lack of quantitative agreement is to be expected because of the 2D nature of the simulations; however, the multiphase lattice Boltzmann simulations still provides useful insight.

Chapter 5

5. Dynamic wetting of an occlusion

This results chapter investigates how and under which conditions the lamella of an impacting droplet is punctured by the presence of a small occlusion. Better understanding the conditions which lead to the rupture of the lamella is critical to produce defect free coating layers in the context of spray coating, for example. An analytical model based on surface energy analysis is proposed to obtain the critical thickness below which the liquid layer above the occlusion is unstable and lamella rupture occurs. Furthermore, we have developed a three dimensional multiphase lattice Boltzmann code to confirm the surface energy analysis and study the influence of key parameters like size of the occlusion, impact velocity and wettability of substrate on hole formation. Results show that a hole is more likely to appear as the diameter of the occlusion, the impact velocity, and the hydrophobicity of the surface increase.

5.1 Problem specification

Hole formation in a thin sheet of liquid has fascinated many researchers in recent decades [99-106]. This dry spot which may lead to a rupture in a liquid film can be observed as the thickness of thin liquid film is decreased to a given threshold [107]. In the context of coating applications, the formation of hole in the lamella is considered a defect and therefore undesirable. Experiments have shown that the thin liquid film which is generated by a droplet impacting on

a solid surface with an intermediate contact angle (around 100°) ruptures for a range of impact velocities, while the film rupture only occurs for the highest impact velocity when the substrate is either hydrophilic or super-hydrophobic [108].

In this chapter, we investigate how the presence of an occlusion can create a hole in the lamella of an impacting droplet. Once the contact line passes over the occlusion, the lamella thickness reduces to a minimum at maximum spread, thus a hole may form into the lamella on top of the occlusion as the thickness of the lamella becomes smaller than a critical film thickness. It can be anticipated that this critical film thickness is dependent on several parameters such as the impact velocity, the surface properties and the size of occlusion.

To study this problem, a spherical droplet which is initially located at the centre of a domain with size $L_x \times L_y \times L_Z = 260\ (lu) \times 260\ (lu) \times 90\ (lu)$, as illustrated in Fig. 5.1, is considered. The droplet impacts and spreads onto a substrate which features a cylinder-shape occlusion. The diameter of the droplet is $D = 65\ lu$. The distance from the impact point to the centre of the occlusion is kept constant ($L = 53\ lu$) and the size of the occlusion including the height (H) and the radius (r) are varied.

During spreading, the lamella touches the occlusion and extends beyond it. At maximum spread, the occlusion may create a hole into the liquid film. An analytical model using surface energy analysis is proposed to predict hole formation which we prove using numerical simulations.

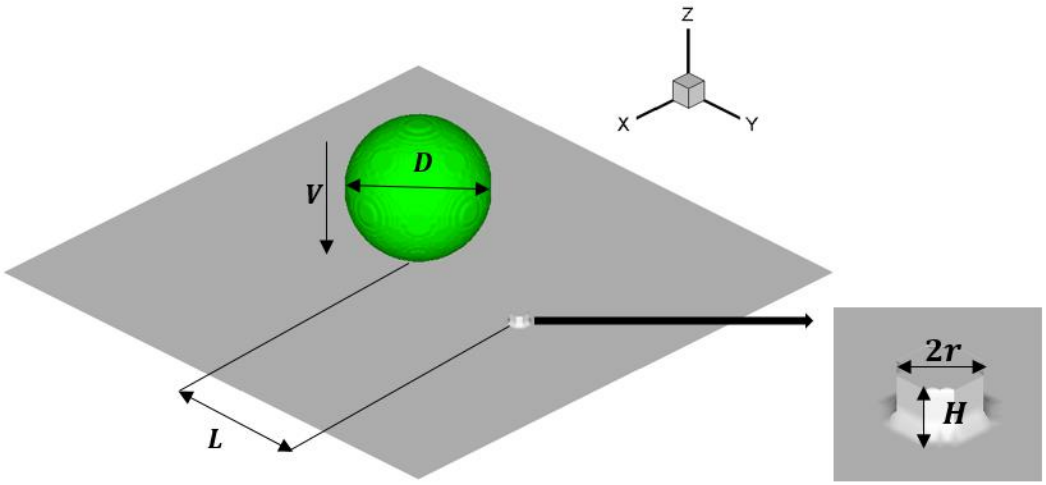

Fig. 5.1. *Simulation domain. A spherical droplet with a given diameter* $D = 65\ lu$ *and an initial velocity* V *impacts and spreads onto a substrate with a cylinder-shape occlusion with diameter* $2r$ *and height* H *. The distance from the impact point to the centre of the occlusion is* $L = 53\ lu$.

5.2 Surface energy analysis

To obtain the critical thickness below which a hole is likely to appear in the liquid film, a surface energy analysis is presented for both the lamella and the hole following Sharma and Ruckenstein [107]. Several assumptions are taken into account to simplify the analysis: the size of droplet, impact velocity and liquid properties are constant. Furthermore, the shape of the hole is a cylinder with a diameter equivalent to $2r$. Thus, the surface energy of the lamella becomes:

$$SE_{lamella} = \gamma A + \gamma_{sl} A' \tag{5.1}$$

where γ_{sl} and γ denote the interfacial tension between solid-liquid and liquid-gas respectively. A is the surface area at the lamella-air interfaces and A' represents the surface area between the lamella and the substrate. Now, when a hole is present on top of the occlusion, the surface energy is given by:

$$SE_{hole} = \gamma(A - \pi r^2) + \gamma_{sl}(A' - \pi r^2) + \gamma 2\pi r h + \gamma_{sg}\pi r^2 \tag{5.2}$$

The total change in the surface energy is therefore given by:

$$\Delta SE = SE_{hole} - SE_{lamella} = \pi r^2(-\gamma - \gamma_{sl} + \gamma_{sg}) + 2\pi r h\gamma \tag{5.3}$$

At this stage, we can substitute Young's equation which is $\gamma_{sg} - \gamma_{sl} = \gamma \cos\theta$ (Eq. (1.1)) into Eq. (5.3) and therefore:

$$\Delta SE = \gamma(-\pi r^2 + \pi r^2 \cos\theta + 2\pi r h) \tag{5.4}$$

During retraction, if $\Delta SE < 0$ then the hole grows in the lamella to break up around the occlusion and if $\Delta SE > 0$ then the hole closes spontaneously. When $\Delta SE = 0$, the critical thickness of the lamella on top of the occlusion to create the hole can be determined:

$$h_c = \frac{r(1 - \cos\theta)}{2} \tag{5.5}$$

At maximum spread, the thickness of the liquid film on top of the occlusion, h, is gradually decreased to reach the critical thickness, h_c,. A hole is unlikely to exist if $h > h_c$ (Fig. 5.2a) and is likely to appear if $h < h_c$ (Fig. 5.2b).

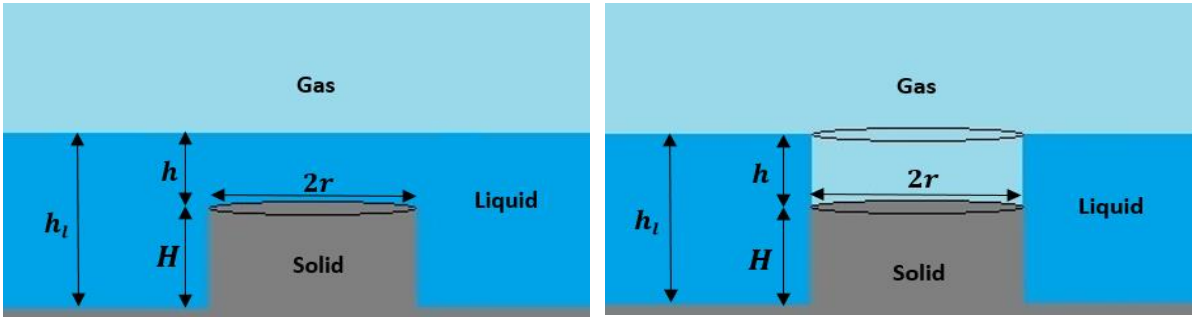

(a) (b)

Fig. 5.2. *Hole formation schematic at maximum spread. (a) There is no hole due to $h > h_c$ (b) A hole exists as $h < h_c$.*

The thickness of the lamella on top of the occlusion is defined as:

$$h = h_l - H \tag{5.6}$$

where H is the height of the occlusion, respectively. h_l denotes the thickness of lamella at maximum spread. It was seen in chapter 3 that h_l can be calculated analytically using Eq. (3.6) and numerically using Eq. (3.8).

5.3 Effect of the occlusion size

Eq. (5.5) illustrates that an increase in the diameter of the occlusion leads to an increase of the thickness threshold. To demonstrate this expected correlation, several simulations are carried out for a constant height of the occlusion ($H = 5\ lu$) but varied diameters. The equilibrium contact angle is adjusted to $\theta = 90°$, the Reynolds and Weber number are set to 117 and 160, respectively. As shown in Table 3.1, the corresponding lamella thickness at maximum spread is $h_l = 6\ lu$ such that the thickness of lamella on top of the occlusion is 1 lu. For $r = 4\ lu$, once the lamella reaches maximum spread, a hole is created (as shown in Fig. 5.3a) as the thickness of the liquid film on top of the occlusion ($h = 1\ lu$) is less than its critical thickness ($h_c = 2\ lu$). During retraction, the hole is growing until a break-up occurs around the occlusion (Fig. 5.3b) and then the droplet recoil to a steady state condition with a contact angle of 90°(Fig. 5.3c).

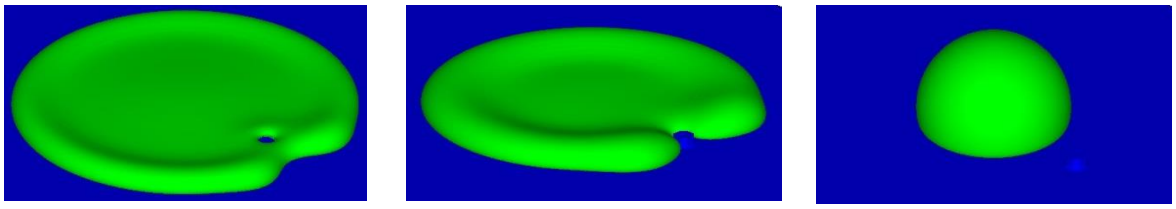

(a) (b) (c)

Fig. 5.3. *Simulation results for the first case as $r = 4\ lu$ and $\theta = 90°$. (a) The hole is created as $h < h_c$ at maximum spread of lamella. (b) During retraction a break-up occurs in the lamella around the occlusion. (c) The droplet reaches a steady state at the impact point with its equilibrium contact angle.*

We consider next a set of conditions for which the thickness of the liquid film on top of the occlusion and the critical thickness are identical. Thus, for the second case, we consider $r = 2\ lu$ and consequently $h = h_c = 1\ lu$. The simulation results are depicted in Fig. 5.4. It can be seen that a hole is created at maximum spread (Fig. 5.4a); however, this hole closes spontaneously during retraction since the film thickness on top of the occlusion becomes larger than the threshold value (Fig. 5.4b). In fact, the surface energy of the lamella which was defeated by the surface energy of the hole at maximum spread ($\Delta SE \leq 0$) overcomes the hole energy during retraction ($\Delta SE > 0$) due to the thickness of liquid film on top of the occlusion exceeding the critical value $h_c = 1\ lu$. Therefore, the hole is unable to grow, the liquid film "heals" and eventually retraction occurs without break-up (Fig. 5.4c).

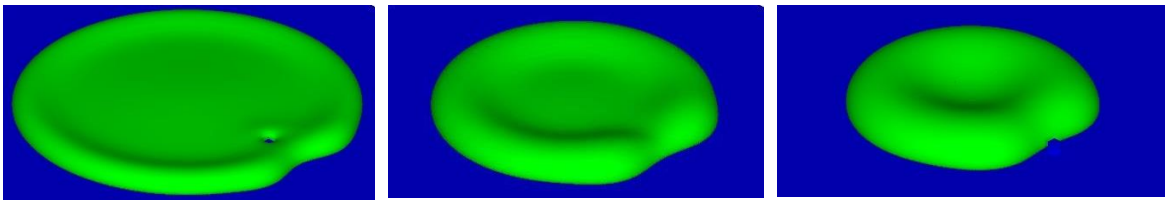

(a) (b) (c)

Fig. 5.4. *Simulation results for the second case as $r = 2\ lu$ and $\theta = 90°$. (a) At maximum spread of lamella: the thickness of lamella on top of the occlusion and the critical thickness ($h = h_c = 1lu$) and therefore hole is created. (b) But the hole closes spontaneously due to $h > h_c$ during retraction. (c) The lamella passes over the occlusion during retraction without break-up.*

In the third case, H is reduced from 5 lu to 3 lu and other parameters are kept the same as Case 1 to confirm that an increase in the thickness of the lamella on top of the occlusion by an amount greater than the critical thickness leads to the absence of hole generation during spreading and retraction. The simulation results demonstrate that a hole does not form for this case during spreading and retraction because to $h > h_c$ (see Fig. 5.5a). The results of this section are summarized in Table 5.1.

Table 5.1. *Dynamic wetting status of the occlusion for three different cases with various sizes of the occlusion (r and H) as* $\theta = 90°$, Re *=117 and* We *=160. For these equilibrium contact angle, Reynolds and Weber numbers, the thickness of the lamella at maximum spread is* $h_l = 6\ lu$ *(see Table 3.1) and therefore the thickness of the lamella on top of the occlusion (h) is determined using Eq. (5.6). The critical thickness is calculated using Eq. (5.5).*

Case	$r\ (lu)$	$H\ (lu)$	$h\ (lu)$	$h_c\ (lu)$	status
1	4	5	1	2	Hole formation
2	2	5	1	1	Hole formation occurs only at maximum spread and then the hole closes during retraction
3	4	3	3	2	No hole formation

5.4 Effect of the Weber number

In this section, two other cases are investigated to show the influence of the impact velocity on hole formation. Firstly, in Case 3 of section 5.3 for which we did not observe any hole the impact velocity is increased until the Reynolds number and the Weber number becomes 156 and 271, respectively. As illustrated in Table 3.1, h_l is 4.69 lu for these Reynolds and Weber numbers. According to Eq. (5.6), the thickness of the lamella on top of the occlusion yields $h = 1.69\ lu$. As shown in Fig. 5.5b, a hole is observed for that case because h is now smaller than h_c at maximum spread .The increase in the impact velocity leads to a smaller lamella thickness and the likely appearance of a hole as intuitively expected.

Secondly, in the Case 1 of section 5.3 for which we did observe the formation of a hole, the impact velocity is reduced until the Reynolds and Weber numbers becomes 100 and 111, respectively and therefore h_l is calculated to be 7.9 lu.. In this case, h is larger than its threshold and thus no hole is created as confirmed by Fig. 5.5c.

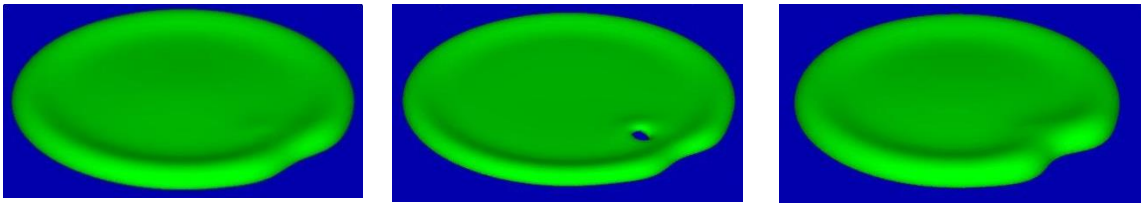

(a) (b) (c)

Fig. 5.5. *Simulation results (a) the hole is not created as* $r = 4\ lu$ *and* $H = 3\ lu$ *(*Re*=117 and* We *=160) due to* $h > h_c$ *. (b) With increase the impact velocity (*Re*=156 and* We*=271) the hole forms on top of the occlusion due to* $h < h_c$ *. (c) In this case the Reynolds and Weber numbers of the Case 1 in section 5.3 (*$r = 4\ lu$ *and* $H = 5\ lu$ *) are decreased to* Re *=100 and* We *=111 and therefore the hole is not created due to* $h > h_c$ *.*

5.5 Effect of substrate wettability

In this section, the diameter of the occlusion is kept constant and θ is varied to investigate the influence of the substrate wettability on hole formation. As Eq. (5.5) shows, the critical thickness reduces with increased wettability of the surface and vice-versa. The critical film thickness h_c for hydrophobic surfaces is larger than h_c for hydrophilic surfaces and thus hole formation is more likely to occur for increasing hydrophobicity.

The simulation results also confirm this correlation. For instance; for a same parameters as those of Case 3 in section 5.3, when θ increases from 90° to 135°, the critical thickness becomes 3.4 lu and therefore hole formation occurs during spreading because $h < h_c$, while no hole formed when $\theta = 90°$. Fig. 5.6 shows the simulations for $\theta = 135°$ and it can be seen that a hole is created at maximum spread time (Fig. 5.6a). The hole then grows towards the centre of liquid film during retraction and a break-up occurs around the occlusion (Fig. 5.6b). Finally the droplet recoils to a spherical cap configuration centred at the impact point with its equilibrium contact angle (Fig. 5.6c).

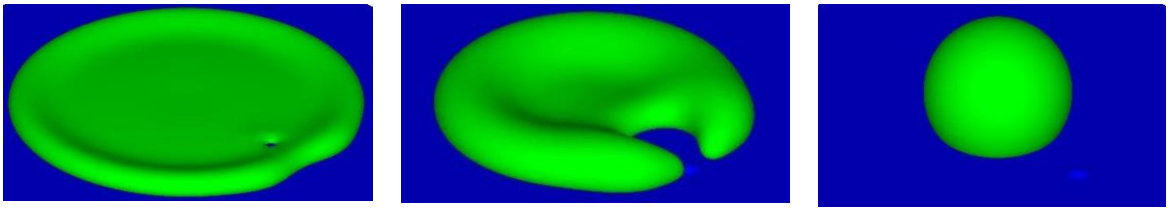

(a) (b) (c)

Fig. 5.6. *Simulation results (a) In Case 3 of section 5.3 ($r = 4\ lu$ and $H = 3\ lu$), with increasing the equilibrium contact angle of the substrate from $\theta = 90°$ to $\theta = 135°$, a hole forms on top of the occlusion because $h < h_c$. (b) During retraction, the lamella around the occlusion breaks up (see the size of the hole once the break-up occurs). (c) Finally, the droplet sits at the impact point with equilibrium contact angle of* $135°$.

Moreover, we carried out another simulation for which all parameters are the same as Case 1 in section 5.3 and only θ is reduced from 90° to 45°. For $\theta = 90°$ we observed that the hole was created, whereas for $\theta = 45°$ no hole is observed (see Fig. 5.7a) and as a consequence further confirm that a hole is unlikely to appear as surface wettability increased. It also interesting to note that when the surface wettability is enhanced, the droplet likes to adhere to the occlusion during retraction (Fig. 5.7b). Thus, the droplet centre of gravity moves from the impact point to a new location closer to the occlusion and adheres to it at its equilibrium contact angle (Fig. 5.7c).

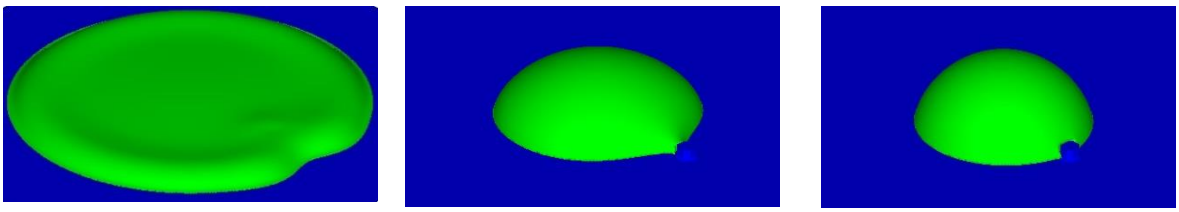

(a) (b) (c)

Fig. 5.7. *Simulation results (a) In Case 1 of section 5.3 ($r = 4\ lu$ and $H = 5lu$), no hole can be observed as the wettability of the substrate decreases from $\theta = 90°$ to $\theta = 135°$. (b) During retraction, the droplet sticks to the occlusion. (c) The droplet moves from the impact point to the occlusion position and sits alongside of the occlusion at its equilibrium contact angle.*

5.6 Summary

In this study, we have performed a surface energy analysis and numerical simulations to investigate how an occlusion may form a hole into the liquid film which is generated by an impacting droplet. This hole formation has been observed as the thickness of the liquid film on top of the occlusion (h) is reduced to reach a critical thickness (h_c). Based on our analytical investigation which involves several simplifying assumption, this critical film thickness depends on the diameter of the occlusion and the wettability of the substrate. Furthermore, the impact velocity plays an essential role on hole formation because the thickness of the lamella (h_l) is reduced when the impact velocity increases. This reduction in h_l leads to a decrease h to a value smaller than h_c and therefore a hole is likely to appear in the lamella.

To confirm these expected trends, we have carried out three-dimensional simulations. In our code, h_l at maximum spread was assumed to be twice the distance between the centre of gravity and the substrate (chapter 3). Then, the effect of various control parameters on hole formation was investigated numerically. The numerical simulations demonstrated that the hole is more likely to form as the diameter of the occlusion, the impact velocity and hydrophobicity of the substrate increase, as one would expect. It has been also observed that with increasing the wettability of substrate, the droplet endeavours to stick to the occlusion during retraction opening up interesting opportunity to control droplets on surfaces after impact.

Chapter 6

6. Drop impact on a pair of pillars

This results chapter aims to investigate the wetting outcomes for an impacting droplet on a surface with a pair of pillars. The expected equilibrium wetting states of a droplet on a textured super-hydrophobic surface normally are the Wenzel or the Cassie-Baxter state. An extra wetting regime arises when considering the wetting of a pair of pillars where the droplet wets both sides of pillars but an air pocket appears directly under the droplet in the spacing between the two pillars. This wetting outcome is henceforth referred to as the engulfed state. Also, the effect of important control parameters such as geometrical parameters on creating the engulfed state is studied. We propose a regime map for different Weber numbers and geometrical parameters to predict the whole range of possible wetting states which are the Engulfed, Wenzel, Cassie-Baxter and Break-up states. Finally, the influence of patterned substrates wettability on outcomes is investigated. Results show that the wetting state varies as the equilibrium contact angle changes from 60° to 150°.

6.1 Problem specification

The investigation of different behaviour of the wetting front in the presence of two occlusions can deepen our understanding of super-hydrophobicity. For example, a question central to the determination of the super-hydrophobic state of the surface is whether the water front

penetrates both pillars and floods them or rather skims on top of pillars and creates an air pocket. This chapter focuses on how and under which conditions the contact line initially attached to the substrate is able to separate from topographical features.

To answer the above question, we consider here a droplet with a given initial diameter $D = 100$ *lu* and an initial velocity V which impacts in the middle of the gap S between two pillars. The substrate with a pair of pillars is shown in Fig. 6.1. Both pillars have a rectangular shape with height H and width W and the equilibrium contact angle is set at 110°. The geometrical parameters can be made dimensionless by normalising them with the droplet diameter. 2D simulations are run with various geometrical parameters and impact velocities with the aim to investigate the influence of control parameters on the behaviour of the wetting front.

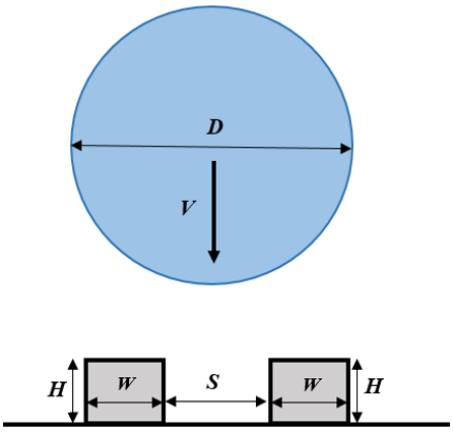

Fig. 6.1. *Geometry and notations for the simulations. The droplet impacts on a substrate with a pair of pillars. D denotes the initial droplet diameter and V is the impact velocity. H, W and S are the geometrical parameters which denote the pillar height, the pillar width and the spacing between them, respectively.*

6.2 Effect of geometrical parameters

In this section, we investigate under which conditions the different equilibrium wetting states occur. Firstly, the pillar spacing and width are varied while the aspect ratio W/H and spacing ratio S/W remain constant at unity. The impact velocity is also kept constant such that We = 50.

To simplify the discussions, a normalized distance between the pillars ($\alpha = S/D$), a normalized pillar width ($\beta = W/D$), a normalized pillar height ($\gamma = h/D$) and a normalized pattern extent ($\varepsilon = (2W + S)/D$) are introduced. With these definitions in mind, four different cases are given by Table 6.1.

Table 6.1. *Four different simulation cases.*

Case	α	β	γ
1	0.2	0.2	0.2
2	0.15	0.15	0.15
3	0.1	0.1	0.1
4	0.05	0.05	0.05

Fig. 6.2 shows simulation results for the final equilibrium state for the four cases. In the first case, the droplet is resting on the pillars and an air pocket is entrapped below the droplet which corresponds to the definition of the Cassie-Baxter state. It is observed that the Wenzel state occurs in the second case for which the liquid completely fills the space between the two pillars from the middle of the droplet like the mushroom state [109].

In cases 3 and 4, the droplet wets the substrate while an air trapped appears directly under the droplet in the spacing between the two pillars. This state which is neither characterized by the Wenzel state nor the Cassie-Baxter one, is labelled the “engulfed state” henceforth. In fact, the engulfed state is supported by this fact that the wetting front which initially wets the substrate is able to separate only on the spacing between pillars and create the air pocket like the Cassie-Baxter state but it is still wetting the outer parts of substrate.

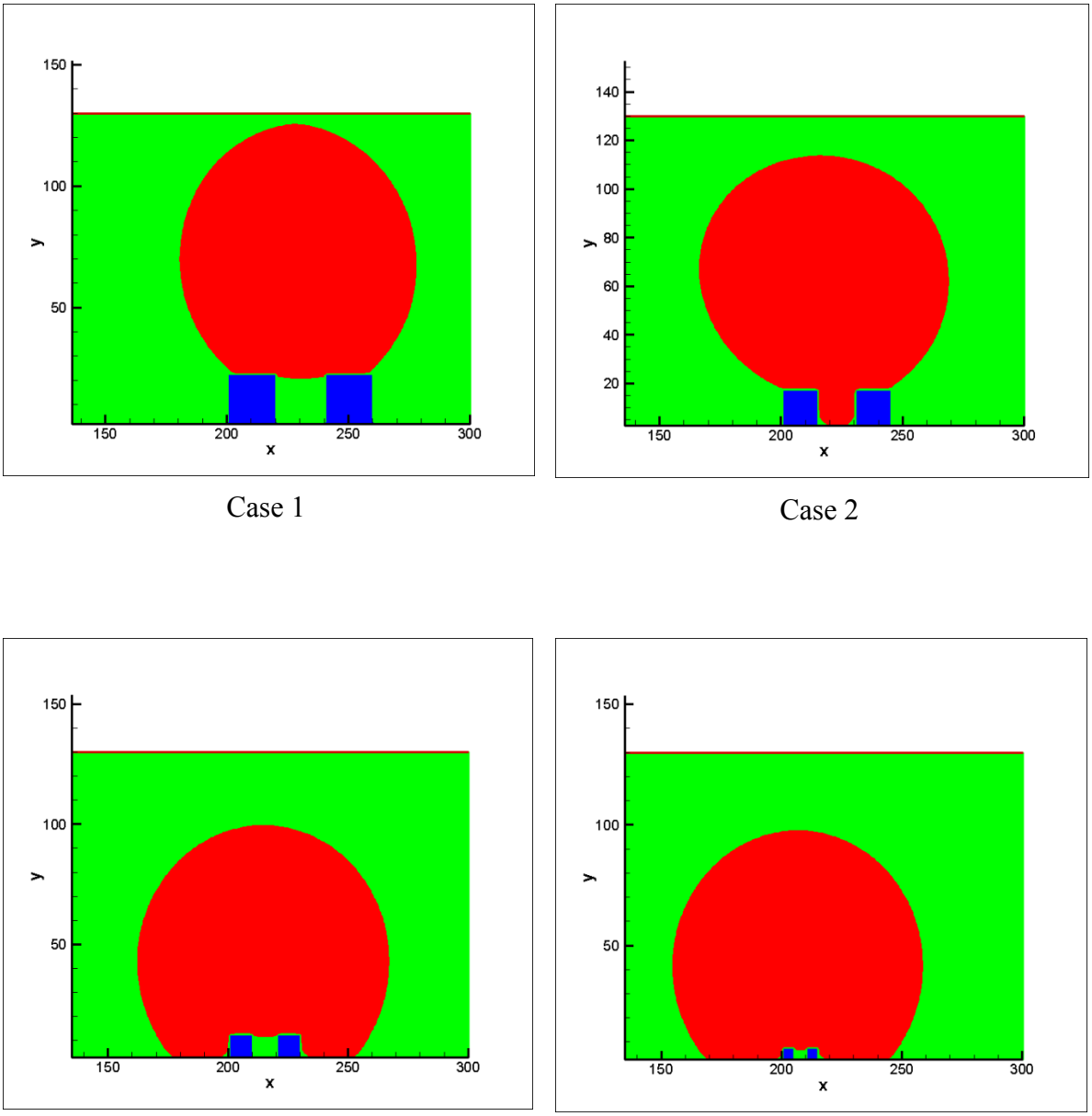

Fig. 6.2. *The wetting outcomes for four different cases: Case 1 illustrates the Cassie-Baxter state as the droplet sits on top of the pillars and an air pocket is observed in the spacing between the pillars. Case 2 shows the mushroom shape of the Wenzel state for which the droplet penetrates and remains in the spacing area. Cases 3 and 4 demonstrate a state for which the droplet wets the substrate however the air pocket exists between two pillars.*

To investigate the effect of the textured surface on the outcomes, the simulation is extended for a wide range of geometric parameters. The aspect ratio of the pillar is unity and the impact velocity is fixed as previously. α is chosen in the range between 0.05 to 0.2 in 0.05 increments and the spacing ratio is not unity.

The simulation results are plotted in Fig. 6.3. It can be seen that the Cassie-Baxter state occurs as ε exceeds 0.5. When this factor is less than 0.5, other states are observed. The engulfed state exists as α is small like 0.05 and 0.1. The Wenzel state happens for α = 0.15 and α = 0.2.

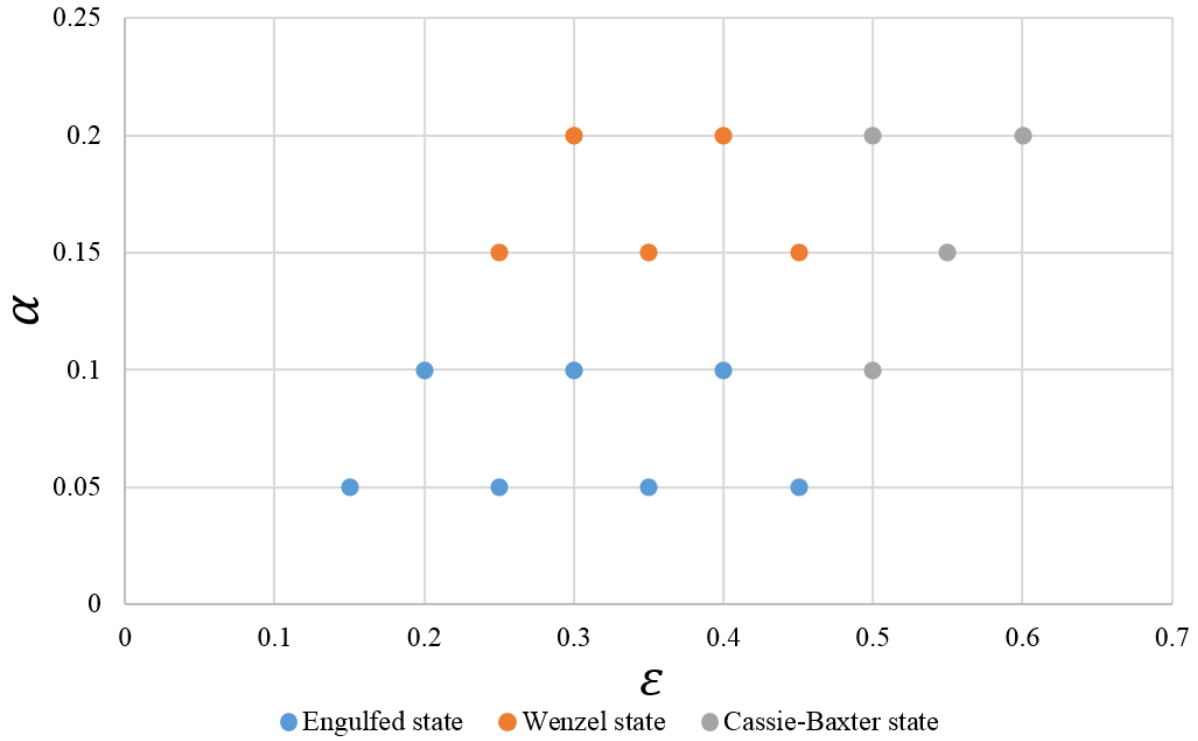

Fig. 6.3. *Influence of the normalized distance between the pillars ($\alpha = S/D$) and the normalized pattern extent ($\varepsilon = (2W + S)/D$) on the wetting outcomes. Three different wetting outcomes are observed: the Engulfed state, the Wenzel state and the Cassie-Baxter state which are illustrated by ◆, ■ and ▲, respectively.*

Moreover, as shown in Fig. 6.4, if α has a value which is greater than a threshold value it appears that the wetting state can switch from the Cassie-Baxter state to the Wenzel state. For example, this threshold value is 0.62 when $\beta = \gamma = 0.2$. In other words, we have the Cassie and Baxter state from α =0.08 until α = 0.61(Fig. 6.4a) but the state changes to the Wenzel state as this value exceeds 0.62(Fig. 6.4b).

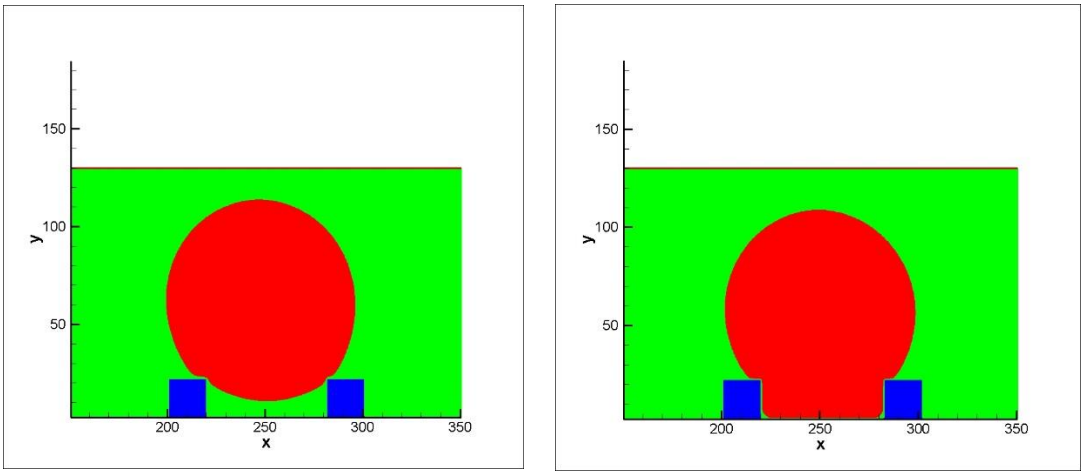

(a) (b)

Fig. 6.4. *Effect of the parameter α on the wetting state for $\beta = \gamma = 0.2$ (a) the Cassie-Baxter state as α = 0.61 and (b) the Wenzel state as α = 0.62.*

The effect of the pillar height is also important. In order to focus the discussion, the spacing ratio is next set to unity and the aspect ratio is varied in the following. The simulation results are depicted in Fig. 6.5. We observed that the state of the wetting is not significantly influenced by the height of the pillar if ε is less than 0.5. In other words, when α and β are chosen in the range between 0.05 to 0.15 the wetting outcome is not changed by increasing or decreasing the height of the pillars.

But it is observed that for $\alpha = \beta = 0.2$, the outcome depends on the height of the pillars. It means that the Cassie-Baxter state is obtained as γ has a value from 0.15 to 0.25. If γ is less than 0.15, the mushroom Wenzel state is observed and whenever this value is equal or greater than 0.29, the engulfed state occurs. It should be mentioned that a non-symmetric state occurs for γ =0.26, 0.27 and 0.28. In these cases either the droplet has not a symmetric profile (γ = 0.26) or the droplet does not sit on the pillars completely (γ = 0.27 and 0.28).

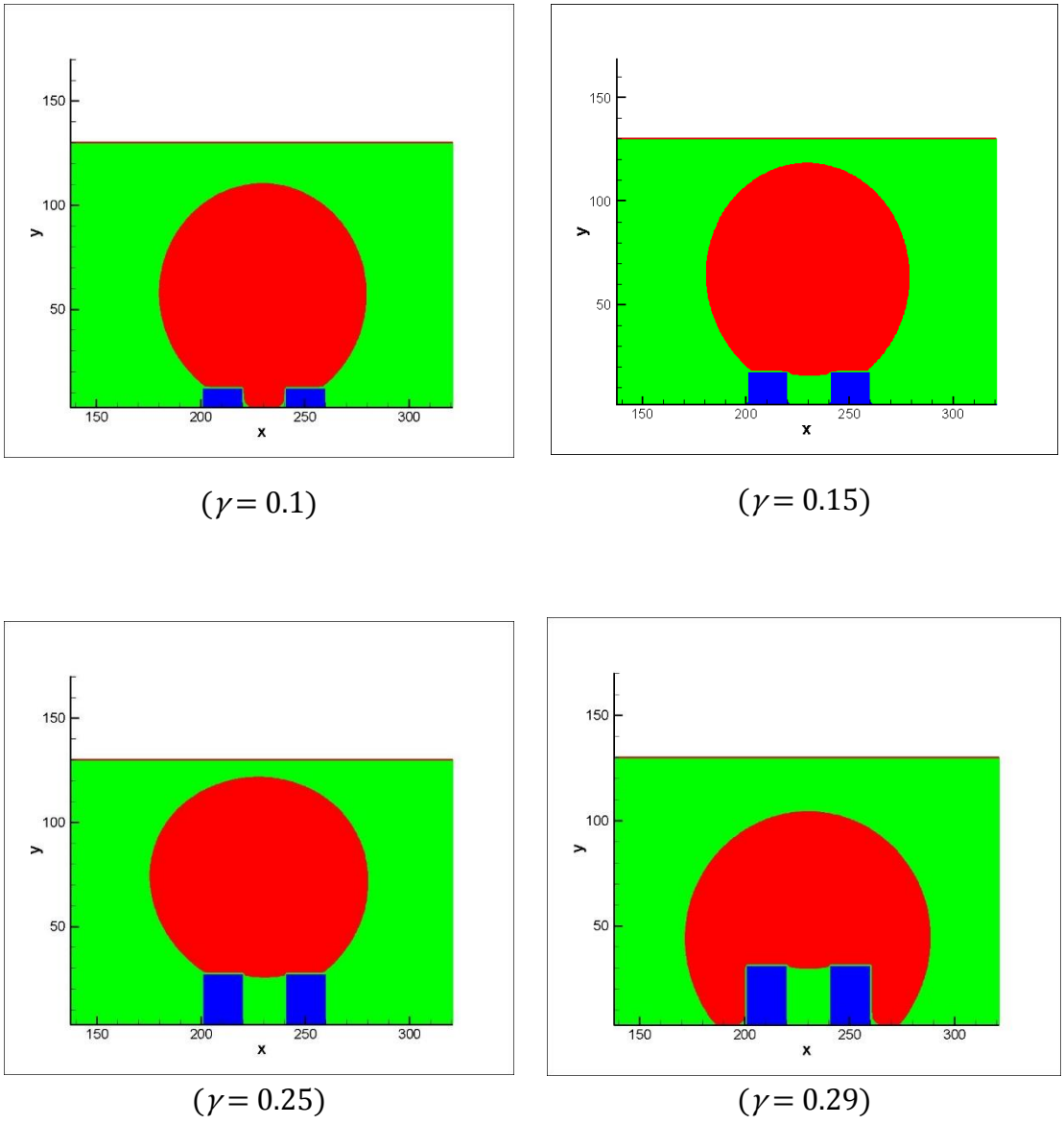

($\gamma = 0.1$) ($\gamma = 0.15$)

($\gamma = 0.25$) ($\gamma = 0.29$)

Fig. 6.5. *Effect of the pillar height on the wetting state as $\alpha = \beta = 0.2$. The Wenzel state is observed for $\gamma < 0.15$, while the Cassie-Baxter exist as $0.15 \leq \gamma \leq 0.25$. When the height of pillar is large ($\gamma \geq 0.29$), the Engulfed state occurs.*

6.3 Effect of the Weber number

Beside the geometrical parameters, the impact velocity has a significant influence on the wetting outcomes. We now simulate the droplet impact on the four different substrates described in Table 6.1 for a wide range of the Weber number. To keep the discussion simple,

the aspect ratio and spacing ratio are kept to unity and therefore the width, height and spacing values are equal. The Weber number is varied by changing the impact velocity.

Droplet break-up can be observed when the Weber number increases. With an increase of the impact velocity, the thickness of lamella reduces which leads to the rupture in the liquid film [108]. In our cases, a thin neck forms between the pillars after impact (see left panel of Fig. 6.6). As the spreading continues, this neck thins further until it breaks up leading to two or more disconnected satellite droplets (see right panel of Fig. 6.6).

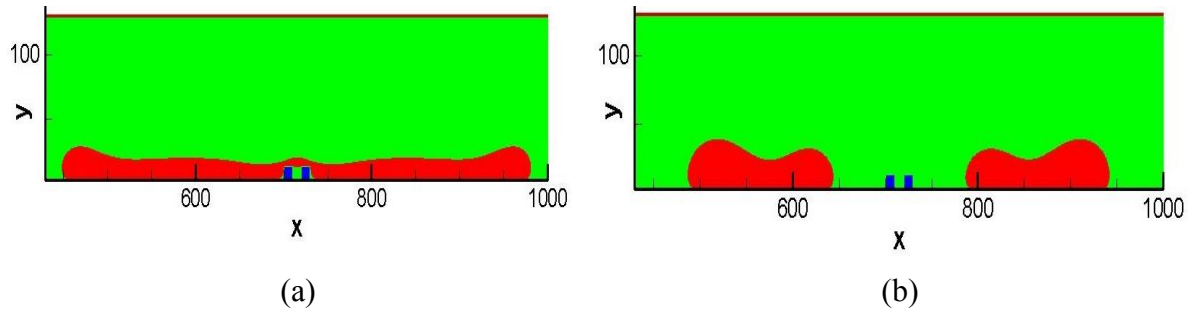

Fig. 6.6. *Droplet Break-up: When the Weber number increases, (a) the droplet spreads onto the substrate and creates a neck on the top of the pillars. (b) This neck becomes thinner and thinner until it ruptures.*

The simulation results for different Weber numbers and geometrical parameters (α and β) are summarized in a regime map shown in Fig. 6.7. This map helps predict the whole range of possible wetting states which are the Engulfed, Wenzel, Cassie-Baxter and Break-up states. It can be seen that the substrate parameters (α and β) play an important role in the wetting outcomes. For pillars with α and β equal 0.05 and 0.1, only two states are possible: the engulfed state for small Weber number followed by break-up for larger Weber numbers. The threshold Weber number between the two states is very close for α and β equal 0.05 and 0.1. When α and β increase to 0.15 and 0.2, the Wenzel state happens first for low Weber number followed the Cassie-Baxter state and break-up for increasing Weber numbers. The threshold between Cassie-Baxter and Break-up occurs for larger Weber number for $\alpha = \beta = 0.15$ when compared to $\alpha = \beta = 0.2$. When $\alpha = \beta = 0.15$, the droplet is able to spread after impact and recoil to sit

on top of the pillar pair. On the other hand, when $\alpha = \beta = 0.2$, as the droplet spreads, the lamella above the pillars thins to the extent that break-up occurs more readily hence the lower Weber number threshold.

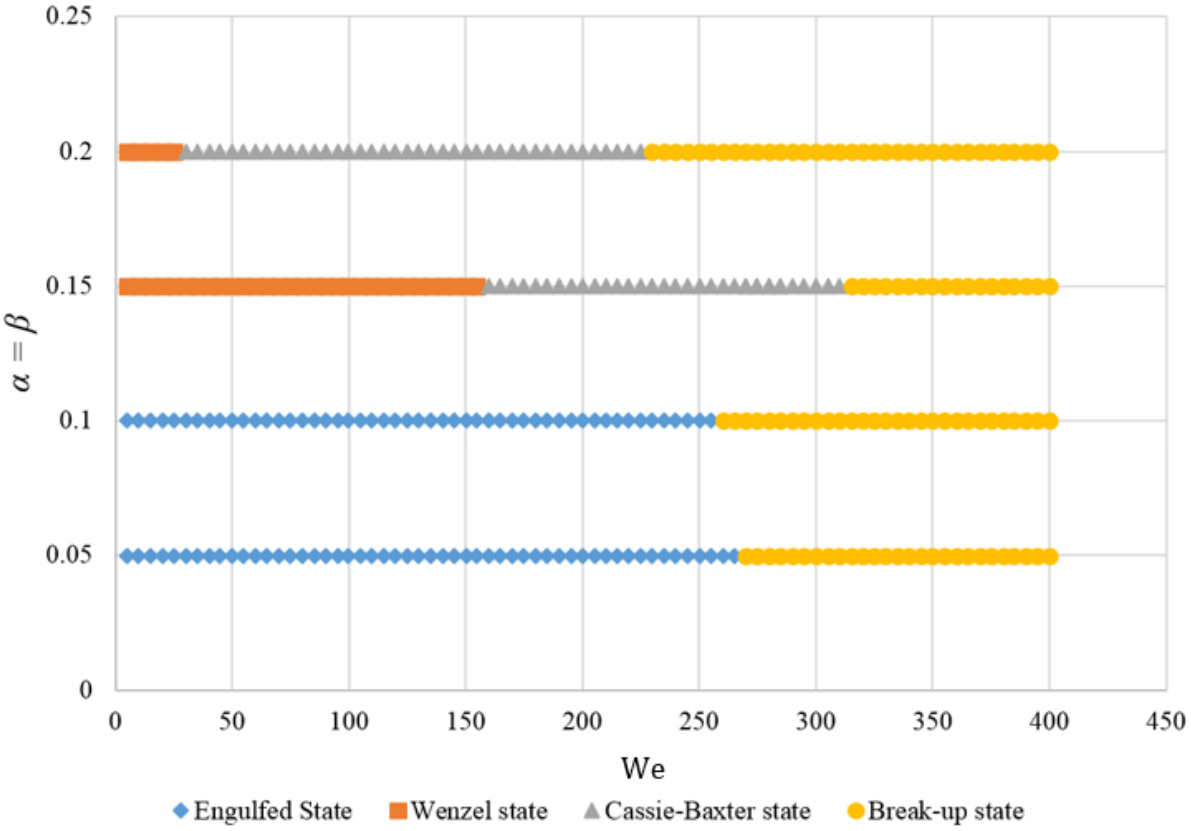

Fig. 6.7. *The regime map for different Weber numbers and geometrical parameters including the normalized distance between the pillars ($\alpha = S/D$) and the normalized pillar width ($\beta = W/D$). Four different states are observed Engulfed (◆), Wenzel (■), Cassie-Baxter (▲) and Break-up (●) states.*

It is also worth noting that the dynamics of spreading and droplet break-up can also be affected by the air flow beneath the droplet because the break-up state occurs only when an air pocket has been created under droplet. In other words, with increasing Weber number, the break-up state cannot been observed directly from the Wenzel state while the break-up happens for the engulfed and Cassie-Baxter states for which an air pocket exists into the spacing between two pillars.

6.4 Effect of substrate wettability

Finally, we investigate the influence of substrate wettability on the wetting front. The same geometrical parameters and conditions presented in section 6.1 are considered and only the equilibrium contact angle is varied. Table 6.2 shows a comparison of the wetting outcomes for a surface with four different contact angles ranging from hydrophilic to super-hydrophobic.

When the equilibrium contact angle of the surface is 150° (super-hydrophobic surface), we observed only the Cassie-Baxter state for all substrate textures. For a hydrophilic surface with a contact angle of 60°, complete wetting occurs for which the lamella spreads over the pillars, touches, and wets the surface are observed. The same outcome also takes place as the contact angle increases to 90° for all α and β values except for $\alpha = \beta$ =0.05 when the engulfed state occurs. A key conclusion of these results is that wetting outcome does not appear to be influenced by the pillar width and spacing when the substrate is hydrophilic or super-hydrophobic.

Table 6.2. *Comparison of the wetting outcomes for a surface with four different contact angles 60°, 90°, 110° and 150°.*

$\alpha = \beta$	Equilibrium Contact Angle			
	60°	90°	110°	150°
0.05	Complete wetting	Engulfed state	Engulfed state	Cassie-Baxter state
0.1	Complete wetting	Complete wetting	Engulfed state	Cassie-Baxter state
0.15	Complete wetting	Complete wetting	Wenzel state	Cassie-Baxter state
0.2	Complete wetting	Complete wetting	Cassie-Baxter state	Cassie-Baxter state

6.5 Summary

The influence of the pillar pair geometric parameters such as the normalized distance between the pillars ($\alpha = S/D$), the normalized pillar width ($\beta = W/D$), the normalized pillar height ($\gamma = h/D$) and the normalized pattern extent ($\varepsilon = (2W + S)/D$) on the droplet wetting outcome has been investigated. Simulation results have demonstrated that the Cassie-Baxter state occurs only as ε becomes sufficiently large and also α has a value which is lower than a threshold value. Simulations also revealed the engulfed state as another possible wetting regime when α and β are small enough. In the engulfed state, the droplet wets both sides of pillars but an air pocket exists between the two pillars. Moreover, the outcome is not significantly influenced by the pillar height for a small values of ε.

In addition to geometrical parameters, the effect of the impact velocity was investigated. We have plotted a regime map of the different wetting outcomes for different Weber numbers and geometrical parameters. We have found that geometrical parameters play an essential role in the spreading and occurrence of droplet break-up as well as the air bubble beneath the droplet. As a consequence, the break-up state took place as an air bubble is trapped beneath the droplet. Finally, we have shown that substrate wettability strongly affect wetting outcomes. For a hydrophilic surface or a super-hydrophobic surface, the width and spacing of the pillars did not affect the wetting outcome in the range of parameters considered.

Chapter 7

7. Oblique impact of a droplet on a textured substrate

This results chapter presents the modelling of an oblique drop impact on a textured substrate to understand the conditions under which the lamella lifts off the substrate and generates a satellite droplet. Depending on the impact angle and the Weber number, four various outcomes are observed: asymmetric spreading, bilateral splashing including a prompt splash and a corona splash, one-sided coronal splashing and asymmetric break-up. To obtain a better understanding of when splashing is likely to occur, a graph which shows splashing thresholds for a range of normal Weber numbers and impact angles between 5° to 45° is presented. Numerical results show that an increasing proportion of the droplet bounces off the surface in the form of satellite droplets for increasingly tangential impacts. Furthermore, the influence of substrate texture parameters such as the height of posts and wettability of the substrate are investigated. Results show that splashing vanishes as the wettability of the substrate increases. Also, the space between posts and the height of posts is shown to play an important role on the occurrence of splashing.

7.1 Problem specification

For oblique impacts, both the normal and tangential components of the impact velocity are considered and therefore the behaviour of the lamella spreading is more complex. In particular, an important question is how the tangential component of the impact velocity influences the dynamics of the contact line. To address this question, several researchers have studied vertical impact onto an inclined stationary surface [57,110-112] and others investigated the vertical impact of droplets onto a moving surface which equally resulted in a tangential component of the impact velocity [58,113-114]. Another case for which the tangential component of the impact velocity matters is oblique impact on a horizontal surface. For such impacts, the role of the impact velocity components on the wetting outcomes has not to this day been investigated systematically. In addition, the effect of the geometrical parameters of the textured hydrophobic surface such as the space between posts, the height of post have not been studied. Thus, the aim of this chapter is to provide a greater understanding of the relation between the splashing, the impact parameters, and the substrate texture for this kind of drop impact.

To achieve this goal, we consider now an oblique droplet impacts on a textured substrate as is shown in Fig. 7.1. The size of the droplet is $D = 200\ lu$ during all 2D simulations and because of its diagonal motion, the impact velocity of the droplet contains two components: $V_n = V \sin \Phi$ and $V_t = V \cos \Phi$. The textured substrate features an array of identical posts. To restrict the number of independent parameters, posts have unit aspect ratio and unit spacing ratio. Therefore the width of posts W, the space between posts S, and the height of posts H are equal and such that $W = S = H = 10\ lu$.The equilibrium contact angle of the substrate is set to $\theta = 150°$ which is referred to a super-hydrophobic surface. We will investigate numerically the conditions under which it breaks-up and generates a satellite droplet.

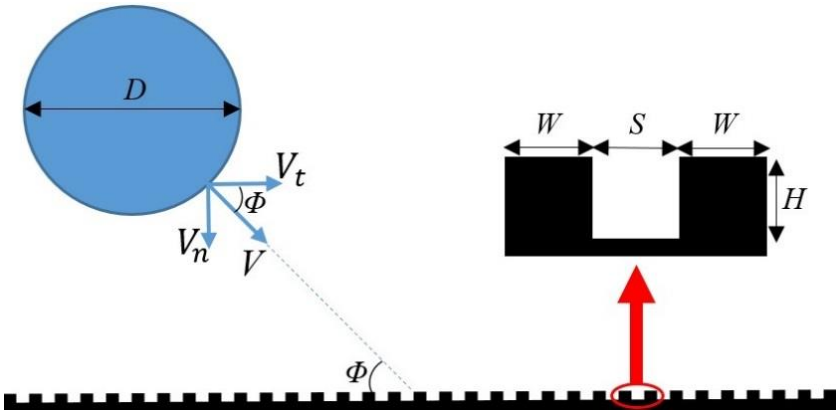

Fig. 7.1. *Schematic of an oblique impacting droplet with a diameter of D and an impact angle Φ onto a textured substrate.*

7.2 Classification of outcomes

First, we investigate the possible outcomes which are observed during our simulations. By varying the normal Weber number and the impact angle, four modes are observed as shown in Fig. 7.2: Case (a), for $\mathrm{We}_n = 125$ and $\Phi = 30°$, asymmetric spreading occurs as the lamella spreads onto the substrate asymmetrically without splashing. Case (b), for $\mathrm{We}_n = 140$ and $\Phi = 20°$, bilateral splashing including a prompt splash which generates tiny droplets onto the substrate from the receding contact line and a corona splash which launches a satellite droplet from the advancing contact line. Case (c), for $\mathrm{We}_n = 140$ and $\Phi = 30°$, one-sided corona splashing which only occurs at the advancing contact line of the lamella. Case (d), for $\mathrm{We}_n = 690$ and $\Phi = 60°$, an asymmetric break-up which takes place as an air pocket appears and grows underneath the lamella and causes a break-up at maximum spread.

It is also worth noting that the combination outcome of Case (c) and Case (d) in Fig. 7.2 may occur. This combination happens when the normal Weber number increases in Case (d) and as a consequence in addition to the occurrence of the asymmetric break-up, the one-sided corona splashing also takes places in the separated right hand part of the lamella.

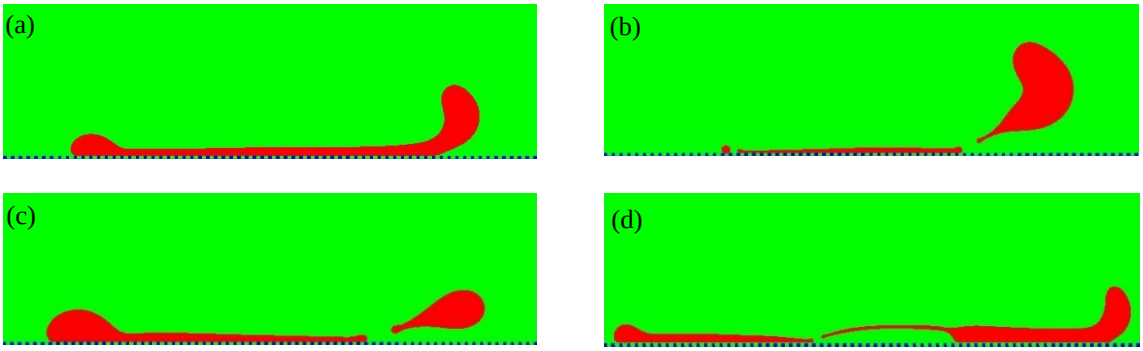

Fig. 7.2. *Four various possible outcomes of the oblique impact of a droplet onto a super-hydrophobic textured substrate: (a) asymmetric spreading (*$\mathrm{We}_n = 125$ *and* $\Phi = 30°$*), (b) bilateral splashing includes simultaneous occurrence of both the prompt splash and the corona splash (*$\mathrm{We}_n = 140$ *and* $\Phi = 20°$*), (c) one-sided corona splashing (*$\mathrm{We}_n = 140$ *and* $\Phi = 30°$*), and (d) asymmetric break-up (*$\mathrm{We}_n = 690$ *and* $\Phi = 60°$*).*

7.3 Effect of impact parameters on splashing

The impact angle of the droplet as well as its normal Weber number lead to different wetting outcomes which have been mentioned in previous section. Numerical results demonstrate that the asymmetric spreading can be observed so long as the normal weber number is insufficient to trigger splashing. Therefore, such outcome may occur for any impact angle. If the normal Weber number is high enough, splashing and asymmetric break-up take place. While bilateral splashing only takes place as long as the impact angle (see Fig. 7.1) is $\Phi \leq 20°$, the one-sided corona splashing happens for an impact angle between $25° \leq \Phi \leq 45°$. When the impact angle becomes $\Phi \geq 50°$ the asymmetric break-up can occur.

Fig. 7.3 illustrates the splashing threshold values for an oblique impact with an impact angle of $5° \leq \Phi \leq 45°$. There is no splash in the area located on the left hand side of the line. It can be seen that splashing is likely to occur with a decrease in the impact angle (i.e. increasingly tangential impact). In other words, with a lower normal weber number, splashing takes for smaller impact angles.

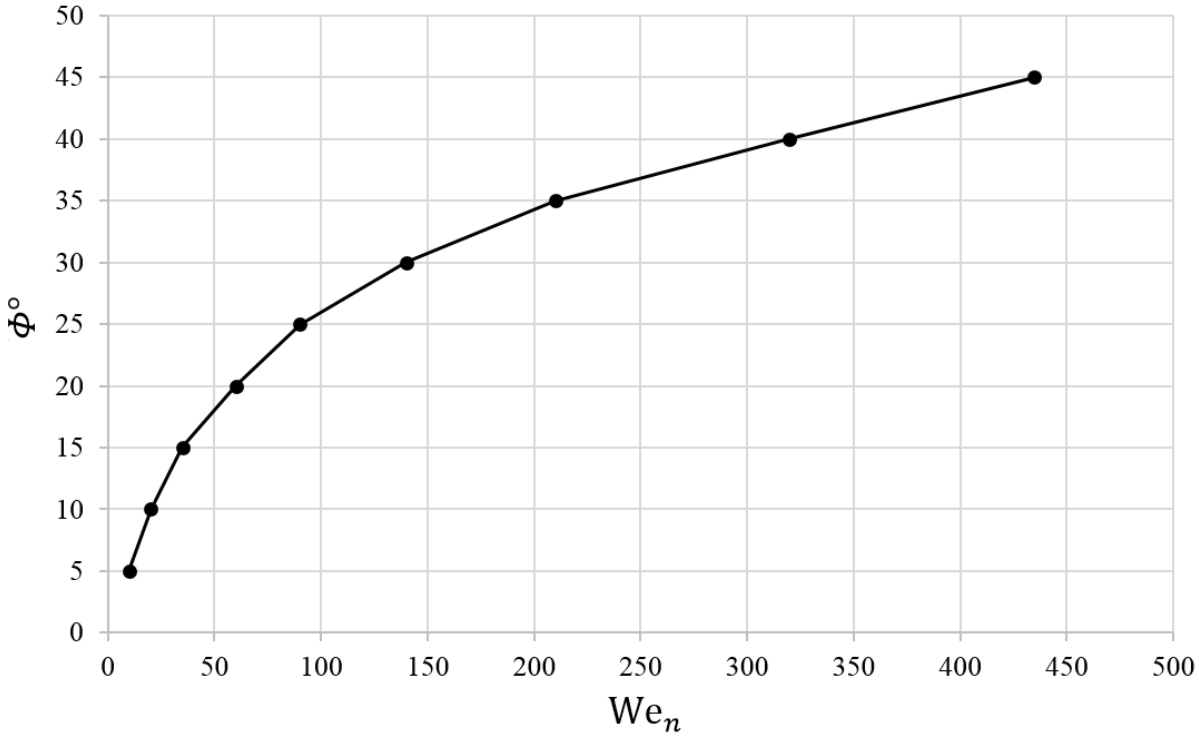

Fig. 7.3. *Corona splashing threshold for an oblique impact with a range of the impact angle between 5° to 45°. On left hand side of the line splashing does not occur.*

During corona splashing, the amount of the mass which detaches away from the lamella is also interesting quantity. In thermal spraying and for a smooth surface, Sobolev and Guilemany [115] reported that the ratio χ of the mass of the droplet which remains onto the substrate to the initial mass of the droplet is dependent on the impact angle as follows:

$$\chi \sim \sin \Phi \tag{7.1}$$

From the above relation, it is obvious that the loss of the droplet mass due to splashing decreases as the impact angle increases. To confirm this trend, we compared two different cases with the same normal Weber number ($\mathrm{We}_n = 140$) and different impact angles ($\Phi = 20°$ for Case (b) and $\Phi = 30°$ for Case (c) in Fig. 7.2). It can be seen that with an increase in the impact angle from Φ =20° to Φ =30°, the mass of the satellite droplet generated during splashing decreases as predicted.

7.4 Effect of textured substrate parameters

In addition to the impact parameters, the substrate parameters such as texture and wettability may influence on splashing. In this section, the normal Weber number and the impact angle are kept constant and equal to $\mathrm{We_n} = 140$ and $\Phi = 30°$ (Case (c) in Fig. 7.2) and numerical simulation were performed for a range of substrate parameters.

First of all, the effect of texture on splashing is investigated. When the substrate does not feature posts, splashing does not occur for a contact angle of 150° with $\mathrm{We_n} = 140$ and $\Phi = 30°$ as seen in Fig. 7.4. Conversely, the presence of texture with $W = S = H = 10\ lu$ was shown to trigger the splash for the same conditions (Case (c) in Fig. 7.2).

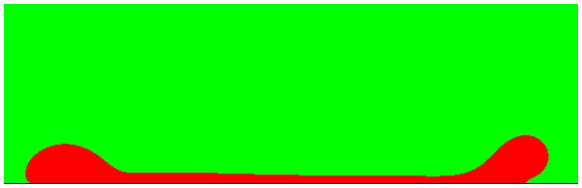

Fig. 7.4. *Although the equilibrium contact angle of the substrate is* $\theta = 150°$ *splashing does not occur for an oblique impact on a smooth substrate with the impact parameters* $\mathrm{We}_n = 140$ *and* $\Phi = 30°$.

To understand the role of the space between posts (S), the height of post (H), and the wettability of the substrate (θ) in the appearance of splashing, we now simulate six different cases as are reported in Table 7.1 and compare these numerical results with Case (c) in Fig. 7.2.

Table 7.1. *Six simulation cases with different substrate parameters. These simulation cases are compared with Case (c) in Fig.7.2 for which the one-sided corona splashing took place.*

Case	Impact Parameters		Substrate Parameters				Status
	We_n	Φ (°)	$W\ (lu)$	$S\ (lu)$	$H\ (lu)$	θ (°)	
1	140	30	10	5	10	150	no splashing
2	140	30	10	20	10	150	splashing
3	140	30	10	10	5	150	no splashing
4	140	30	10	10	20	150	splashing
5	140	30	10	10	25	150	no splashing
6	140	30	10	10	10	110	no splashing
(c) in Fig. 7.2	140	30	10	10	10	150	splashing

The simulation results for Case 1 and Case 2 for which only the space between posts is varied are depicted in Fig. 7.5. It can be seen that with S equal to 5 lu (Case 1) the splashing does not occur (see Fig. 7.5a), whereas with an increase in this parameter to 20 lu (Case 2) splashing is observed (see Fig. 7.5b) as was seen for Case (c) for which S was 10 lu. The difference between Case 2 and Case (c) is that splashing occurs earlier (17,000 ts for Case 2 against 20,000 ts for Case (c)). This means that the space between posts affects the time and the likelihood of splashing.

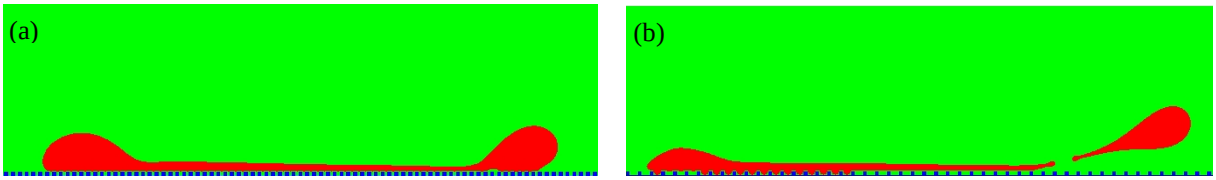

Fig. 7.5. *The effect of the space between posts (S) on the occurrence of splashing for an oblique impact with* $\mathrm{We}_n = 140$ *and* $\Phi = 30°$ *on a textured substrate with an equilibrium contact angle* $\theta = 150°$*: (a) the splashing does not occur for Case 1 which S=5 lu and the height of posts (H) and the width of posts (W) are 10 lu but (b) splashing occurs for Case 2 which S=20 lu and* $H = W = 10$ *lu.*

Beside the space between posts, the height of the posts also plays an important role in splashing. Our numerical results demonstrate that for Case 3 for which the height of posts is $H = 5\ lu$ splashing does not happen as shown in Fig. 7.6a, while as previously observed in Fig. 7.2c splashing occurs when $H = 10\ lu$. Splashing takes place until $H = 20\ lu$ (Case 4). When the height of posts reaches $H = 25\ lu$ (Case 5), splashing is once more prevented as shown in Fig. 7.6b. Thus, splashing occurs between two thresholds of post height.

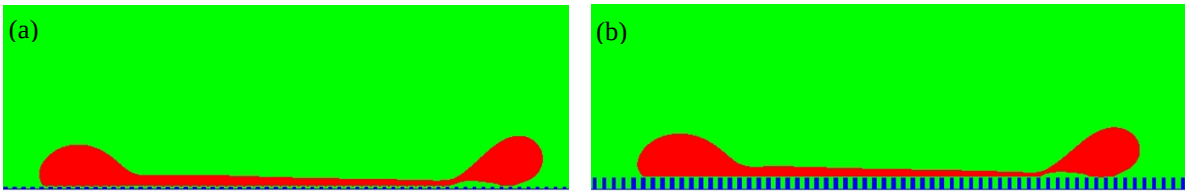

Fig. 7.6. *For an oblique impacting droplet with* $\mathrm{We}_n = 140$ *and* $\Phi = 30°$ *onto a textured substrate with* $S = W = 10$ *lu, the splashing is unlikely to occur as the height of the posts are either (a)* $H = 5$ *lu or (b)* $H = 25$ *lu.*

To investigate the effect of the wettability of the substrate on splashing, we consider another case (Case 6) for which the impact parameters ($We_n = 140$ and $\Phi = 30°$) and texture parameters ($W = S = H = 10\ lu$) are similar to Case (c) in Fig. 7.2. The equilibrium contact angle of the substrate is set to $\theta = 110°$. Fig. 7.2c showed that splashing occurs when the equilibrium substrate contact angle is 150°. With a reduction in the contact angle from 150° to 110°, as is shown in Fig. 7.7, the splashing is seen to be prevented since wettability of the substrate increases.

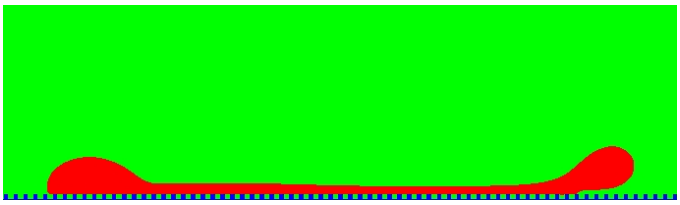

Fig. 7.7. *Simulation result for an oblique impacting droplet with an impact angle of 30° and normal Weber number of 140. The equilibrium contact angle of the substrate is θ = 110°. The numerical results show that the splashing vanishes with an increase in wettability of the substrate to θ = 110°.*

7.5 Summary

In this chapter, we investigated how the lamella of an oblique impacting droplet behaves onto a textured super-hydrophobic substrate. For oblique impacts, an asymmetric behaviour has been observed due to the tangential component of the impact velocity.

Four various wetting outcomes have been identified for such impacts. The asymmetric spreading happens for any impact angle Φ as the normal Weber is sufficiently low such that surface tension prevents splashing. Depending on the impact angle, other wetting outcome occur with an increase in the normal Weber number. Bilateral splashing including prompt and corona splash is observed for an impact angle $\Phi \leq 20°$, one-sided corona splash for $25° \leq \Phi \leq 45°$ and the asymmetric break-up for $\Phi \geq 50°$. We have also presented a graph which illustrates splashing threshold values for impact angles $5° \leq \Phi \leq 45°$. Results show that

splashing is more likely to occur for smaller impact angle. Moreover, we have demonstrated that the mass of the satellite droplet generated during corona splashing decreases as the impact angle increases as predicted by others.

In addition to the impact parameters, we have studied the influences of the geometrical parameters of the textured substrate (the space between posts and the height of the posts) and also the wettability of the surface on the occurrence of splashing. We observed that the time and the occurrence of splashing are influenced by the distance between posts. Furthermore, corona splashing only occurs in a limited range of post heights. Finally, our result show that with a decrease of the substrate contact angle from θ=150° to θ=110°, splashing is prevented as intuitively expected.

Chapter 8

8. Conclusions and future works

This chapter briefly reports key findings of the current work and gives the conclusions of this study. Recommendations for the future works are also provided.

8.1 Conclusions

This thesis aimed at understanding how a droplet wets a textured substrate after impact. To reach this aim, a numerical simulation tool using the Shan-Chen multiphase lattice Boltzmann method was developed. The Solvers were thoroughly validated for static and dynamic wetting conditions using a range of previously published results and correlations. The present method was first used for simulating the impact of a droplet onto a substrate which featured a single occlusion and also a pair of occlusions. This numerical model enabled a deeper understanding of the wetting process and allowed us to probe the role of various control parameters such as the Weber number, geometrical parameters and substrate wettability on the wetting outcomes. Moreover, for oblique impacts, the influence of these control parameters as well as the impact angle on the wetting of an occlusion array were discussed due to this problem was less understood.

The proposed methodology has limitations. For example, simulations were not able to capture the smaller length scale effects entirely because of the restrictions on the liquid to gas density

ratio which is of O (10) in the simulations, approximately two orders of magnitude smaller than typical liquid/gas systems. The consequence of this small density ratio is that the surrounding atmosphere is not has "passive" as it would be in a real system and most likely dampens any instability which would otherwise grow in a real system.

Despite this drawback, the multiphase lattice Boltzmann method proves a very powerful tool to unravel wetting phenomena such as drop impact and provides insight which could not be paralleled experimentally. It is also important to stress that the lattice Boltzmann method offers a significant advantage when compared to continuum multiphase simulations methods such as the Volume of Fluid methods which faces difficulties when modelling the wetting of complex, textured surfaces. For example, in the LBM phase separation can be produced spontaneously from the particle kinetics and therefore there is no need to control and remedy the interfaces. Moreover, the LBM is simple to use for complex boundary conditions such as bounce-back boundaries, whereas mesh refinement or boundary-fitted grid are essential for such boundaries in other CFD tools. It is also worth noting that in the LBM the pressure field is obtained straight from the density distribution and therefore there is no need to solve the Poisson equation. This supremacy as well as parallel process computing bring a decrease in the computational time for this methodology.

Key findings of this research are listed as follows:

- ✓ For an impacting droplet onto a single ridged surface, the possible wetting outcomes are pinning, wetting, and splashing. The wetting outcome is dictated by the dimensionless distance from the impact point to the ridge and the Weber number,
- ✓ During the wetting of an occlusion after drop impact, a hole in the lamella is more likely to be triggered by the occlusion if the diameter of the occlusion, the impact velocity and hydrophobicity of the substrate are increased.

- ✓ When considering the wetting of a pair of pillars, the engulfed state was introduced as an extra wetting regime. Moreover, the geometrical parameters and the air bubble beneath the droplet influenced the occurrence of droplet break-up
- ✓ For oblique impacts, a satellite droplet was more likely to be generated when the substrate was textured. The occurrence of splashing was dependent on the impact angle, the Weber number, the geometrical parameters of the textured substrate and also the substrate wettability.

By better understanding of a droplet wets a limited number of occlusion, this thesis sheds light on the different wetting outcomes and contributes to developing guidelines on how to produce bioinspired, man-made super-hydrophobic surfaces with specific properties. Although occlusions cannot be considered in isolation on a complex textured surface, this thesis helps understand when the liquid is more likely to "flood" the texture (i.e. penetrates every single asperities) or skim on top of the occlusion leaving air pockets trapped underneath.

8.2 Future works

With the conclusions of this thesis in mind, the following future extensions of the current work are suggested:

- Development of a multiphase Lattice Boltzmann simulation tool able to handle a greater liquid to gas density ratio [116-118] will allow a more accurate study of dynamic wetting. Further improvement of this simulation tool will be achieved by a parallelization of the computations. Parallel computing would allow the simulation of larger computational domains for a broader range of parameters.
- Some industrial applications involve the impact of a non-Newtonian droplet onto a surface such as milk droplet in dairy industry. Therefore, the simulation of non-

Newtonian droplet impact will be an interesting extension to the research presented in this thesis.

- The ambient pressure may change the behaviour of the spreading lamella during wetting of the substrate (see Ref. [37]). This control parameter which was not considered in this study can affect wetting outcomes, particularly for the lamella break-up in chapter 6 and splashing in chapter 7.
- The effect of the flexibility of the pillar array can be addressed in the future works. It is possible that this flexibility may enhance super-hydrophobicity as observed on some animals such fur seals: the hairy skin of the seal traps air which reduces its overall drag. The fouling of these man-made super-hydrophobic surface for specific engineering applications will also need to be carefully studied and better understood in the future in order to make them industrially relevant.
- Finally, an important question is how to produce a surface texture in an accurate and reliable way, likely to scale up to mass production. In order to address this question, it will be important to consider material selection and manufacturing processes which are compatible with the targeted engineering applications.

References

[1] De Gennes, P.G., Brochard-Wyart, F. and Quere, D., 2013. Capillarity and wetting phenomena: drops, bubbles, pearls, waves. Springer Science & Business Media.

[2] Young, T., 1805. III. An essay on the cohesion of fluids. Philosophical transactions of the royal society of London, 95, pp.65-87.

[3] Guo, Z., Liu, W. and Su, B.L., 2011. Superhydrophobic surfaces: from natural to biomimetic to functional. Journal of colloid and interface science, 353(2), pp.335-355.

[4] Gao, L., Fadeev, A.Y. and McCarthy, T.J., 2008. Superhydrophobicity and contact-line issues. MRS bulletin, 33(08), pp.747-751.

[5] Feng, X.J. and Jiang, L., 2006. Design and creation of superwetting/antiwetting surfaces. Advanced Materials, 18(23), pp.3063-3078.

[6] Jeong, D.W., Shin, U.H., Kim, J.H., Kim, S.H., Lee, H.W. and Kim, J.M., 2014. Stable hierarchical superhydrophobic surfaces based on vertically aligned carbon nanotube forests modified with conformal silicone coating. Carbon, 79, pp.442-449.

[7] Barthlott, W. and Neinhuis, C., 1997. Purity of the sacred lotus, or escape from contamination in biological surfaces. Planta, 202(1), pp.1-8.

[8] Feng, X.Q., Gao, X., Wu, Z., Jiang, L. and Zheng, Q.S., 2007. Superior water repellency of water strider legs with hierarchical structures: experiments and analysis. Langmuir, 23(9), pp.4892-4896.

[9] Zheng, Y., Gao, X. and Jiang, L., 2007. Directional adhesion of superhydrophobic butterfly wings. Soft Matter, 3(2), pp.178-182.

[10] Fritsch, A., Willmott, G.R. and Taylor, M., 2013. Superhydrophobic New Zealand leaves: contact angle and drop impact experiments. Journal of the Royal Society of New Zealand, 43(4), pp.198-210.

[11] Celia, E., Darmanin, T., de Givenchy, E.T., Amigoni, S. and Guittard, F., 2013. Recent advances in designing superhydrophobic surfaces. Journal of colloid and interface science, 402, pp.1-18.

[12] Verho, T., Korhonen, J.T., Sainiemi, L., Jokinen, V., Bower, C., Franze, K., Franssila, S., Andrew, P., Ikkala, O. and Ras, R.H., 2012. Reversible switching between superhydrophobic states on a hierarchically structured surface. Proceedings of the National Academy of Sciences, 109(26), pp.10210-10213.

[13] Farhadi, S., Farzaneh, M. and Kulinich, S.A., 2011. Anti-icing performance of superhydrophobic surfaces. Applied Surface Science, 257(14), pp.6264-6269.

[14] Shirtcliffe, N.J. and Roach, P., 2013. Superhydrophobicity for Antifouling Microfluidic Surfaces. Microfluidic Diagnostics: Methods and Protocols, pp.269-281.

[15] Truesdell, R., Mammoli, A., Vorobieff, P., van Swol, F. and Brinker, C.J., 2006. Drag reduction on a patterned superhydrophobic surface. Physical review letters, 97(4), p.044504.

[16] Miljkovic, N. and Wang, E.N., 2013. Condensation heat transfer on superhydrophobic surfaces. MRS bulletin, 38(05), pp.397-406.

[17] Naebe, M., Robins, N., Wang, X. and Collins, P., 2013. Assessment of performance properties of wetsuits. Proceedings of the Institution of Mechanical Engineers, Part P: Journal of Sports Engineering and Technology, 227(4), pp.255-264.

[18] Massinon, M. and Lebeau, F., 2012. Experimental method for the assessment of agricultural spray retention based on high-speed imaging of drop impact on a synthetic superhydrophobic surface. Biosystems Engineering, 112(1), pp.56-64.

[19] Makkonen, L., 2012. Ice adhesion—theory, measurements and countermeasures. Journal of Adhesion Science and Technology, 26(4-5), pp.413-445.

[20] Wenzel, R.N., 1936. Resistance of solid surfaces to wetting by water. Industrial & Engineering Chemistry, 28(8), pp.988-994.

[21] Cassie, A.B.D. and Baxter, S., 1944. Wettability of porous surfaces. Transactions of the Faraday society, 40, pp.546-551.

[22] https://en.wikipedia.org/wiki/Ultrahydrophobicity

[23] Zu, Y.Q. and Yan, Y.Y., 2016. Single droplet on micro square-post patterned surfaces–theoretical model and numerical simulation. Scientific reports, 6, p.19281.

[24] Gross, M., Varnik, F. and Raabe, D., 2009. Fall and rise of small droplets on rough hydrophobic substrates. EPL (Europhysics Letters), 88(2), p.26002.

[25] Bormashenko, E., 2015. Progress in understanding wetting transitions on rough surfaces. Advances in colloid and interface science, 222, pp.92-103.

[26] Sui, Y., Ding, H. and Spelt, P.D., 2014. Numerical simulations of flows with moving contact lines. Annual Review of Fluid Mechanics, 46.

[27] Dupuis, A. and Yeomans, J.M., 2005. Modelling droplets on superhydrophobic surfaces: equilibrium states and transitions. Langmuir, 21(6), pp.2624-2629.

[28] Lundgren, M., Allan, N.L. and Cosgrove, T., 2007. Modelling of wetting: a study of nanowetting at rough and heterogeneous surfaces. Langmuir, 23(3), pp.1187-1194.

[29] Smith, A.F., Mahelona, K. and Hendy, S.C., 2017. The rolling and slipping of droplets on superhydrophobic surfaces. arXiv preprint arXiv:1712.05523.

[30] Andrade, R., Skurtys, O. and Osorio, F., 2013. Drop impact behaviour on food using spray coating: Fundamentals and applications. Food research international, 54(1), pp.397-405.

[31] Massinon, M. and Lebeau, F., 2012. Experimental method for the assessment of agricultural spray retention based on high-speed imaging of drop impact on a synthetic superhydrophobic surface. Biosystems Engineering, 112(1), pp.56-64.

[32] Castrejón-Pita, J.R., Martin, G.D., Hoath, S.D. and Hutchings, I.M., 2008. A simple large-scale droplet generator for studies of inkjet printing. Review of Scientific Instruments, 79(7), p.075108.

[33] Kim, J., 2007. Spray cooling heat transfer: the state of the art. International Journal of Heat and Fluid Flow, 28(4), pp.753-767.

[34] Yarin, A.L., 2006. Drop impact dynamics: splashing, spreading, receding, bouncing…. Annu. Rev. Fluid Mech., 38, pp.159-192.

[35] Van der Veen, R.C., Hendrix, M.H., Tran, T., Sun, C., Tsai, P.A. and Lohse, D., 2014. How microstructures affect air film dynamics prior to drop impact. Soft matter, 10(21), pp.3703-3707.

[36] Varnik, F., Gross, M., Moradi, N., Zikos, G., Uhlmann, P., Müller-Buschbaum, P., Magerl, D., Raabe, D., Steinbach, I. and Stamm, M., 2011. Stability and dynamics of droplets on patterned substrates: insights from experiments and lattice Boltzmann simulations. Journal of Physics: Condensed Matter, 23(18), p.184112.

[37] Tsai, P., CA van der Veen, R., van de Raa, M. and Lohse, D., 2010. How micropatterns and air pressure affect splashing on surfaces. Langmuir, 26(20), pp.16090-16095.

[38] Shahraz, A., Borhan, A. and Fichthorn, K.A., 2013. Wetting on physically patterned solid surfaces: the relevance of molecular dynamics simulations to macroscopic systems. Langmuir, 29(37), pp.11632-11639.

[39] Scheller, B.L. and Bousfield, D.W., 1995. Newtonian drop impact with a solid surface. AIChE Journal, 41(6), pp.1357-1367.

[40] Pasandideh-Fard, M., Qiao, Y.M., Chandra, S. and Mostaghimi, J., 1996. Capillary effects during droplet impact on a solid surface. Physics of fluids, 8(3), pp.650-659.

[41] Clanet, C., Béguin, C., Richard, D. and Quéré, D., 2004. Maximal deformation of an impacting drop. Journal of Fluid Mechanics, 517, pp.199-208.

[42] Ukiwe, C. and Kwok, D.Y., 2005. On the maximum spreading diameter of impacting droplets on well-prepared solid surfaces. Langmuir, 21(2), pp.666-673.

[43] Roisman, I.V., 2009. Inertia dominated drop collisions. II. An analytical solution of the Navier–Stokes equations for a spreading viscous film. Physics of Fluids, 21(5), p.052104.

[44] Eggers, J., Fontelos, M.A., Josserand, C. and Zaleski, S., 2010. Drop dynamics after impact on a solid wall: theory and simulations. Physics of Fluids, 22(6), p.062101.

[45] Rioboo, R., Tropea, C. and Marengo, M., 2001. Outcomes from a drop impact on solid surfaces. Atomization and Sprays, 11(2).

[46] Xu, L., 2007. Liquid drop splashing on smooth, rough, and textured surfaces. Physical Review E, 75(5), p.056316.

[47] Kim, H., Park, U., Lee, C., Kim, H., Hwan Kim, M. and Kim, J., 2014. Drop splashing on a rough surface: How surface morphology affects splashing threshold. Applied Physics Letters, 104(16), p.161608.

[48] Marengo, M., Antonini, C., Roisman, I.V. and Tropea, C., 2011. Drop collisions with simple and complex surfaces. Current Opinion in Colloid & Interface Science, 16(4), pp.292-302.

[49] Khojasteh, D., Kazerooni, M., Salarian, S. and Kamali, R., 2016. Droplet impact on superhydrophobic surfaces: A review of recent developments. Journal of Industrial and Engineering Chemistry, 42, pp.1-14.

[50] Josserand, C. and Thoroddsen, S.T., 2016. Drop impact on a solid surface. Annual review of fluid mechanics, 48, pp.365-391.

[51] Bartolo, D., Bouamrirene, F., Verneuil, É., Buguin, A., Silberzan, P. and Moulinet, S., 2006. Bouncing or sticky droplets: Impalement transitions on superhydrophobic micropatterned surfaces. EPL (Europhysics Letters), 74(2), p.299.

[52] Bange, P.G. and Bhardwaj, R., 2016. Computational study of bouncing and non-bouncing droplets impacting on superhydrophobic surfaces. Theoretical and Computational Fluid Dynamics, 30(3), pp.211-235.

[53] Liu, Y., Moevius, L., Xu, X., Qian, T., Yeomans, J.M. and Wang, Z., 2014. Pancake bouncing on superhydrophobic surfaces. Nature Physics, 10(7), pp.515-519.

[54] Josserand, C., Lemoyne, L., Troeger, R. and Zaleski, S., 2005. Droplet impact on a dry surface: triggering the splash with a small obstacle. Journal of fluid mechanics, 524, pp.47-56.

[55] de Jong, R., Enríquez, O.R. and van der Meer, D., 2015. Exploring droplet impact near a millimetre-sized hole: comparing a closed pit with an open-ended pore. Journal of fluid mechanics, 772, pp.427-444.

[56] Ellis, A.S., Smith, F.T. and White, A.H., 2011. Droplet Impact on to a Rough Surface. Quarterly Journal of Mechanics & Applied Mathematics, 64(2).

[57] Yeong, Y.H., Burton, J., Loth, E. and Bayer, I.S., 2014. Drop impact and rebound dynamics on an inclined superhydrophobic surface. Langmuir, 30(40), pp.12027-12038.

[58] Aboud, D.G. and Kietzig, A.M., 2015. Splashing threshold of oblique droplet impacts on surfaces of various wettability. Langmuir, 31(36), pp.10100-10111.

[59] Kadau, K., Germann, T.C. and Lomdahl, P.S., 2006. Molecular dynamics comes of age: 320 billion atom simulation on BlueGene/L. International Journal of Modern Physics C, 17(12), pp.1755-1761.

[60] Perumal, D.A. and Dass, A.K., 2015. A Review on the development of lattice Boltzmann computation of macro fluid flows and heat transfer. Alexandria Engineering Journal, 54(4), pp.955-971.

[61] d'Humieres, D., Lallemand, P. and Frisch, U., 1986. Lattice gas models for 3D hydrodynamics. EPL (Europhysics Letters), 2(4), p.291.

[62] McNamara, G.R. and Zanetti, G., 1988. Use of the Boltzmann equation to simulate lattice-gas automata. Physical review letters, 61(20), p.2332.

[63] Lallemand, P. and Luo, L.S., 2000. Theory of the lattice Boltzmann method: Dispersion, dissipation, isotropy, Galilean invariance, and stability. Physical Review E, 61(6), p.6546.

[64] Wolf-Gladrow, D.A., 2004. Lattice-gas cellular automata and lattice Boltzmann models: an introduction. Springer.

[65] Higuera, F.J., Succi, S. and Benzi, R., 1989. Lattice gas dynamics with enhanced collisions. EPL (Europhysics Letters), 9(4), p.345.

[66] Qian, Y.H., dHumieres, D. and Lallemand, P., 1992. Lattice BGK models for Navier-Stokes equation. EPL (Europhysics Letters), 17(6), p.479.

[67] Bhatnagar, P.L., Gross, E.P. and Krook, M., 1954. A model for collision processes in gases. I. Small amplitude processes in charged and neutral one-component systems. Physical review, 94(3), p.511.

[68] d'Humières, D., 2002. Multiple–relaxation–time lattice Boltzmann models in three dimensions. Philosophical Transactions of the Royal Society of London A: Mathematical, Physical and Engineering Sciences, 360(1792), pp.437-451.

[69] Frisch, U., Hasslacher, B. and Pomeau, Y., 1986. Lattice-gas automata for the Navier-Stokes equation. Physical review letters, 56(14), p.1505.

[70] He, X. and Luo, L.S., 1997. Theory of the lattice Boltzmann method: From the Boltzmann equation to the lattice Boltzmann equation. Physical Review E, 56(6), p.6811.

[71] Zhang, J., 2011. Lattice Boltzmann method for microfluidics: models and applications. Microfluidics and Nanofluidics, 10(1), pp.1-28.

[72] Sukop, M. and Thorne, D.T., 2006. Lattice Boltzmann modeling: an introduction for geoscientists and engineers. 2nd. ed.

[73] Mohamad, A.A., 2011. Lattice Boltzmann method: fundamentals and engineering applications with computer codes. Springer Science & Business Media.

[74] Rothman, D.H. and Keller, J.M., 1988. Immiscible cellular-automaton fluids. Journal of Statistical Physics, 52(3), pp.1119-1127.

[75] Gunstensen, A.K., Rothman, D.H., Zaleski, S. and Zanetti, G., 1991. Lattice Boltzmann model of immiscible fluids. Physical Review A, 43(8), p.4320.

[76] Shan, X. and Chen, H., 1993. Lattice Boltzmann model for simulating flows with multiple phases and components. Physical Review E, 47(3), p.1815.

[77] Shan, X. and Chen, H., 1994. Simulation of nonideal gases and liquid-gas phase transitions by the lattice Boltzmann equation. Physical Review E, 49(4), p.2941.

[78] Swift, M.R., Osborn, W.R. and Yeomans, J.M., 1995. Lattice Boltzmann simulation of nonideal fluids. Physical Review Letters, 75(5), p.830.

[79] Swift, M.R., Orlandini, E., Osborn, W.R. and Yeomans, J.M., 1996. Lattice Boltzmann simulations of liquid-gas and binary fluid systems. Physical Review E, 54(5), p.5041.

[80] He, X., Chen, S. and Zhang, R., 1999. A lattice Boltzmann scheme for incompressible multiphase flow and its application in simulation of Rayleigh–Taylor instability. Journal of Computational Physics, 152(2), pp.642-663.

[81] Lee, T. and Lin, C.L., 2005. A stable discretization of the lattice Boltzmann equation for simulation of incompressible two-phase flows at high density ratio. Journal of Computational Physics, 206(1), pp.16-47.

[82] Sankaranarayanan, K., Shan, X., Kevrekidis, I.G. and Sundaresan, S., 2002. Analysis of drag and virtual mass forces in bubbly suspensions using an implicit formulation of the lattice Boltzmann method. Journal of Fluid Mechanics, 452, pp.61-96.

[83] Falcucci, G., Ubertini, S., Bella, G. and Succi, S., 2013. Lattice Boltzmann simulation of cavitating flows. Communications in Computational Physics, 13(03), pp.685-695.

[84] Chan, T.S., Srivastava, S., Marchand, A., Andreotti, B., Biferale, L., Toschi, F. and Snoeijer, J.H., 2013. Hydrodynamics of air entrainment by moving contact lines. Physics of fluids, 25(7), p.074105.

[85] Hyväluoma, J. and Harting, J., 2008. Slip flow over structured surfaces with entrapped microbubbles. Physical review letters, 100(24), p.246001.

[86] Chen, L., Kang, Q., Mu, Y., He, Y.L. and Tao, W.Q., 2014. A critical review of the pseudopotential multiphase lattice Boltzmann model: Methods and applications. International Journal of Heat and Mass Transfer, 76, pp.210-236.

[87] Benzi, R., Biferale, L., Sbragaglia, M., Succi, S. and Toschi, F., 2006. Mesoscopic modeling of a two-phase flow in the presence of boundaries: the contact angle. Physical Review E, 74(2), p.021509.

[88] Yuan, P. and Schaefer, L., 2006. Equations of state in a lattice Boltzmann model. Physics of Fluids, 18(4), p.042101.

[89] Huang, H., Krafczyk, M. and Lu, X., 2011. Forcing term in single-phase and Shan-Chen-type multiphase lattice Boltzmann models. Physical Review E, 84(4), p.046710.

[90] Bird, J.C., Dhiman, R., Kwon, H.M. and Varanasi, K.K., 2013. Reducing the contact time of a bouncing drop. Nature, 503(7476), p.385.

[91] Gauthier, A., Symon, S., Clanet, C. and Quéré, D., 2015. Water impacting on superhydrophobic macrotextures. Nature communications, 6, p.8001.

[92] Regulagadda, K., Bakshi, S. and Das, S.K., 2017. Morphology of drop impact on a superhydrophobic surface with macro-structures. Physics of Fluids, 29(8), p.082104.

[93] Reyssat, M., Richard, D., Clanet, C. and Quéré, D., 2010. Dynamical superhydrophobicity. Faraday discussions, 146, pp.19-33.

[94] Robson, S. and Willmott, G.R., 2016. Asymmetries in the spread of drops impacting on hydrophobic micropillar arrays. Soft matter, 12(21), pp.4853-4865.

[95] Tsai, P., Hendrix, M.H., Dijkstra, R.R., Shui, L. and Lohse, D., 2011. Microscopic structure influencing macroscopic splash at high Weber number. Soft Matter, 7(24), pp.11325-11333.

[96] Collings, E.W., Markworth, A.J., McCoy, J.K. and Saunders, J.H., 1990. Splat-quench solidification of freely falling liquid-metal drops by impact on a planar substrate. Journal of Materials Science, 25(8), pp.3677-3682.

[97] Bennett, T. and Poulikakos, D., 1993. Splat-quench solidification: estimating the maximum spreading of a droplet impacting a solid surface. Journal of Materials Science, 28(4), pp.963-970.

[98] Wildeman, S., Visser, C.W., Sun, C. and Lohse, D., 2016. On the spreading of impacting drops. Journal of fluid mechanics, 805, pp.636-655.

[99] Padday, J.F., 1970. Cohesive properties of thin films of liquids adhering to a solid surface. Special Discussions of the Faraday Society, 1, pp.64-74.

[100] Taylor, G.I. and Michael, D.H., 1973. On making holes in a sheet of fluid. Journal of fluid mechanics, 58(4), pp.625-639.

[101] Redon, C., Brochard-Wyart, F. and Rondelez, F., 1991. Dynamics of dewetting. Physical review letters, 66(6), p.715.

[102]Kheshgi, H.S. and Scriven, L.E., 1991. Dewetting: Nucleation and growth of dry regions. Chemical engineering science, 46(2), pp.519-526.

[103] Moriarty, J.A. and Schwartz, L.W., 1993. Dynamic considerations in the closing and opening of holes in thin liquid films. Journal of colloid and interface science, 161(2), pp.335-342.

[104] López, P.G., Miksis, M.J. and Bankoff, S.G., 2001. Stability and evolution of a dry spot. Physics of Fluids, 13(6), pp.1601-1614.

[105] Bankoff, S.G., Johnson, M.F.G., Miksis, M.J., Schluter, R.A. and Lopez, P.G., 2003. Dynamics of a dry spot. Journal of Fluid Mechanics, 486, pp.239-259.

[106] Sellier, M., Grayson, J.W., Renbaum-Wolff, L., Song, M. and Bertram, A.K., 2015. Estimating the viscosity of a highly viscous liquid droplet through the relaxation time of a dry spot. Journal of Rheology, 59(3), pp.733-750.

[107] Sharma, A. and Ruckenstein, E., 1989. Dewetting of solids by the formation of holes in macroscopic liquid films. Journal of colloid and interface science, 133(2), pp.358-368.

[108] Dhiman, R. and Chandra, S., 2009, December. Rupture of thin films formed during droplet impact. In Proceedings of the Royal Society of London A: Mathematical, Physical and Engineering Sciences (p. rspa20090425). The Royal Society.

[109] Ishino, C. and Okumura, K., 2008. Wetting transitions on textured hydrophilic surfaces. The European Physical Journal E, 25(4), pp.415-424.

[110] Šikalo, Š., Tropea, C. and Ganić, E.N., 2005. Impact of droplets onto inclined surfaces. Journal of colloid and interface science, 286(2), pp.661-669.

[111] LeClear, S., LeClear, J., Park, K.C. and Choi, W., 2016. Drop impact on inclined superhydrophobic surfaces. Journal of colloid and interface science, 461, pp.114-121.

[112] Liu, J., Vu, H., Yoon, S.S., Jepsen, R.A. and Aguilar, G., 2010. Splashing phenomena during liquid droplet impact. Atomization and Sprays, 20(4).

[113] Chen, R.H. and Wang, H.W., 2005. Effects of tangential speed on low-normal-speed liquid drop impact on a non-wettable solid surface. Experiments in fluids, 39(4), pp.754-760.

[114] Bird, J.C., Tsai, S.S. and Stone, H.A., 2009. Inclined to splash: triggering and inhibiting a splash with tangential velocity. New Journal of Physics, 11(6), p.063017.

[115] Sobolev, V. and Guilemany, J.M., 1997. Effect of droplet impact angle on flattening of splat in thermal spraying. Materials Letters, 32(2-3), pp.197-201.

[116] Lee, T. and Lin, C.L., 2005. A stable discretization of the lattice Boltzmann equation for simulation of incompressible two-phase flows at high density ratio. Journal of Computational Physics, 206(1), pp.16-47.

[117] Li, Q., Luo, K.H. and Li, X.J., 2013. Lattice Boltzmann modeling of multiphase flows at large density ratio with an improved pseudopotential model. Physical Review E, 87(5), p.053301.

[118] Falcucci, G., Ubertini, S. and Succi, S., 2010. Lattice Boltzmann simulations of phase-separating flows at large density ratios: the case of doubly-attractive pseudo-potentials. Soft Matter, 6(18), pp.4357-4365.